SELF-ASSEMBLY OF LIQUID CRYSTALS AND CHIRAL SUPERSTRUCTURES: FROM COARSE-GRAINED TO FULLY ATOMISTIC MODELS

by

Fangyong Yan

MS Chemistry, Sichuan University, China, 2002

Submitted to the Graduate Faculty of

the Arts and Sciences in partial fulfillment

of the requirements for the degree of

Doctor of Philosophy

University of Pittsburgh

2011

UNIVERSITY OF PITTSBURGH

CHEMISTRY DEPARTMENT

This dissertation was presented

by

Fangyong Yan

It was defended on

April 18, 2011

and approved by

Kenneth D. Jordan, Chemistry Department

Rob Coalson, Chemistry Department

Nathaniel Rosi, Chemistry Department

J. Karl Johnson, Chemical Engineering Department

Dissertation Director: Kenneth D. Jordan, Chemistry Department

SELF-ASSEMBLY OF LIQUID CRYSTALS AND CHIRAL SUPERSTRUCTURES: FROM COARSE-GRAINED TO FULLY ATOMISTIC MODELS

Fangyong Yan, PhD

University of Pittsburgh, 2011

Computer simulations have been used to study the self-assembly of liquid crystals and/or chiral superstructures in both coarse-grained and fully atomistic models. In chapters 4-6, coarse-grained models of rigid achiral bent-core and linear molecules were found to self-assemble to chiral superstructures and liquid crystalline phases. Chiral dopants were found to induce the system to adopt a consistent chiral twist direction, the first molecular scale computer simulation of this effect. Superstructural chirality can be tuned into rigid linear particles by the appropriate spacing of Lennard-Jones (LJ) particles. These results point to design rules that can be manipulated for the experimental synthesis of chiral structures from achiral particles.

In chapters 7-8, the largest liquid crystal atomistic simulations to date, to our knowledge, have been performed for both a series of single component liquid crystals and liquid crystal mixtures. It was also demonstrated for the first time, to our knowledge, the formation of smectic phases from an isotropic liquid state at the all atom level. These simulations are in good agreement with experiments,[1, 2] and show that atomistic simulations are capable of capturing macroscopic phase behavior changes induced by a small variation in the structure of single component liquid crystal molecules, or by concentration change in the liquid crystal mixtures. This opens up the possibility of theoretically designing and screening liquid crystals with desired properties.

TABLE OF CONTENTS

LIST OF FIGURES

PREFACE

I am so grateful to my research advisors, Professors David J. Earl and Kenneth D. Jordan.

Professor David J. Earl is always encouraging me in my research, challenging me with new and interesting research topics, and also patient with me when I was having problems with my research. He is the person who guides me into the amazing world of computational chemistry.

Professor Kenneth D. Jordan has been supervising me since July, 2010. He has been training me in dealing with scientific problems with insight. He has also been encouraging me to try new directions in my research.

I want to thank Professor Coalson for his great support in my PhD study. After taking his statistical mechanics class, I have found myself attracted by math equations, which have been very helpful in my computational research.

I want to thank Dr. Adam Hixson for his equal contribution in the coarse-grained model simulations. I also want to thank him for showing me patience and kindness when he was teaching me computer algorithms.

I want to thank Professor Richard Christie for his invaluable help in Center for Molecular and Materials Simulation (CMMS).

I want to thank Professor Mark R. Wilson from Chemistry Department of University of Durham, for his generosity providing us with his LCFF[8] force field for atomistic simulations of liquid crystals.

I want to thank Professor Kenneth D. Jordan, Professor Rob Coalson, Professor Nathaniel Rosi and Professor J. Karl Johnson, all members of my thesis committee, for their invaluable help in preparing this thesis.

Many thanks go to all the members in Professor David J. Earl's group and Professor

Kenneth D. Jordan's group, and all my friends in Pittsburgh, for their encouragement and help in my PhD study.

Finally, many thanks also go to family, especially my parents, for their love, encouragement and understanding. It was very difficult for them to send their son abroad to pursue a PhD in the United States. Mom and Dad, this thesis is dedicated to both of you.

1.0 INTRODUCTION

1.1 COARSE-GRAINED SIMULATION STUDY OF RIGID ACHIRAL MOLECULES

The development of design rules that relate the architecture and chemistry of a molecule or building block to the superstructures and phases that it can form remains a fundamental goal of the physical sciences[9, 10, 11, 12, 13] and has implications for the synthesis of materials that may be of importance in a range of emerging applications.[14, 15, 16, 17, 18, 19, 20, 21] Recently, anisotropy has been proposed as a method by which the self-assembly of nanoparticle and colloidal building blocks can be controlled[9], providing a link between the field of liquid crystals and the assembly of large scale building blocks into useful materials. Over the last two decades, computer simulations have played a prominent role in the development of theories of liquid crystalline phase formation and stability, and simplified coarse-grained models have been particularly useful in understanding the relationship between molecular shape and phase behaviour.[10, 22, 23, 24] These principles are beginning to be applied to the study of nanoparticle and colloidal building blocks[11, 25, 26, 27, 28, 29, 30] and have the potential for providing significant insight into the ordered arrangement of these particles that will be required in building useful materials in the future.

1.1.1 LIQUID CRYSTALS SELF-ASSEMBLED BY BENT-CORE MOLECULES

Liquid crystals are phases of matter that have properties intermediate between those of a liquid and those of a crystal.[31] Due to their mobility and long range order they have many applications, for example in liquid crystal displays, lasers, functional polymers, optical systems, supramolecular electronic and optoelectronic materials, and biomolecular materials.[32, 33, 34, 35, 36, 37]. Liquid crystals are formed through the spontaneous self-assembly of the constituent molecules into ordered phases.[31] In order to generate liquid crystalline phases, the constituent molecules must have anisotropic shapes, as in rod-like or disk-like molecules, or be amphiphilic in nature.[38, 31, 39] Rod-like molecules can self-assemble to form layers, which are known as smectic liquid crystalline phases; and disc-like molecules can self-assemble to form columns, which are known as columnar liquid crystalline phases. Both rod-like and disk-like molecules can form the nematic phase (N).[31, 38] When the symmetry of the constituent molecule is reduced so that it becomes more anisotropic, other liquid crystal phases can form.[14, 12] For example, introducing a bending angle at the centre of rod-like molecules leads to the more anisotropic bent-core (banana-shaped) molecules, which can exhibit more phases as well as chirality[14, 40]. A typical bent-core molecule is shown in Fig. 1.

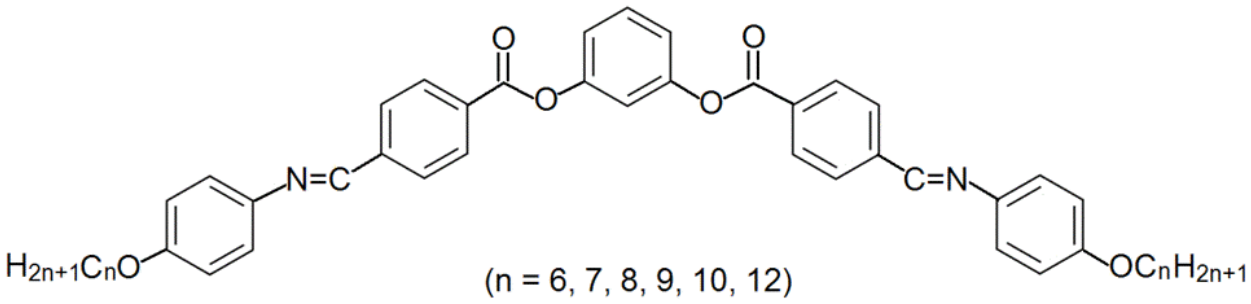

Figure 1: A typical bent-core (banana-shaped) molecule. The figure is adapted from ref. [3].

Due to their rich phase behavior and feature of chirality[41, 14, 42, 40, 43, 44, 45, 13],

bent-core molecules have evolved into a major topic in liquid crystal research[14, 40], and have broad applications in optical and electronic devices[46, 47, 48, 49, 50], and in forming fibers[51]. The most well-known liquid crystalline phases found in bent-core molecules are the nematic phase (N), the smectic phases, and the chiral banana phases[14, 40]. In a nematic phase, the centres of mass of the molecules have no translational order, a feature which is similar to that of a conventional liquid. However, there is orientational order along the system director, $\vec{n}$, as shown in Fig. 2a.

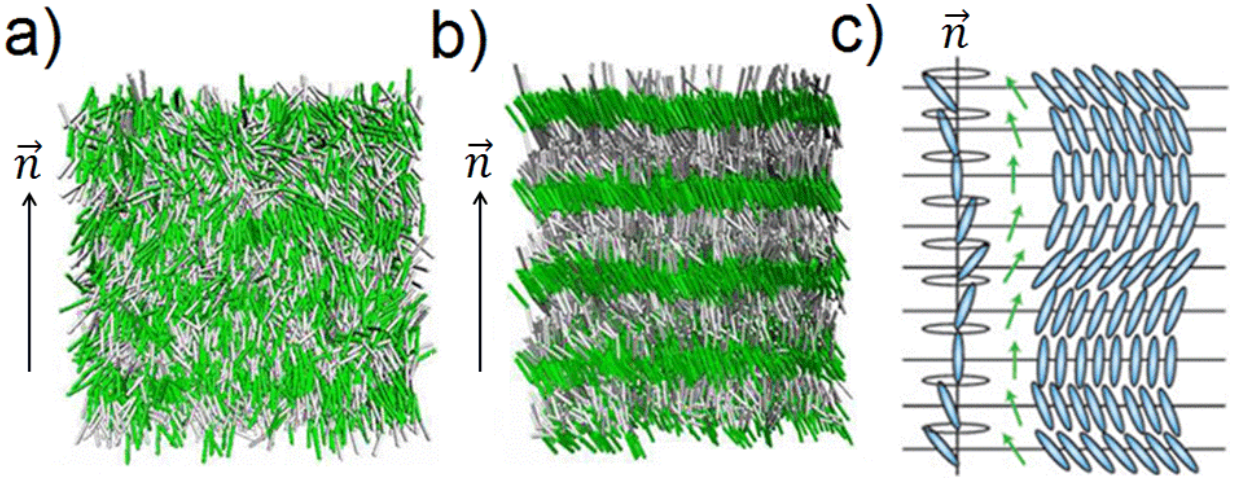

Figure 2: (a) Simulation snapshot of a nematic phase (N) obtained in our simulation.[4] (b) Simulation snapshot of a smectic C phase (SmC) obtained in our simulation. There are four tilted layers in this structure, with a regular spacing between each layer. (c) A typical chiral smectic C phase (SmC*). Compared with SmC phase, it has smectic C layers, but all layers twist along system director $\vec{n}$. The figure is adapted from ref. [5].

The basic smectic phases formed by bent-core molecules are smectic A (SmA), smectic C (SmC), smectic I (SmI), and chiral smectic C (SmC*).[14, 40] All smectic phases have layered structures with a well-defined interlayer spacing, with long-range order along the system director $\vec{n}$. A picture of SmC phase formed by bent-core molecules from our computer simulation[4] is shown in Fig. 2b. By comparison, a SmC* phase shows the smectic layers twist along axis $\vec{n}$, as shown in Fig. 2c. Bent-core molecules also form the banana phases,

which refer to a class of liquid crystalline phases B_n ($1 \leq n \leq 8$)[14, 40], where each B_n represents a group of liquid crystalline phases with similar structures. A feature of chirality has been found in B2, B4 and B6 phases[40].

1.1.2 CHIRAL SUPERSTRUCTURES SELF-ASSEMBLED FROM ACHIRAL MOLECULES

The formation of chiral superstructures and phases is an area of high interest from both a theoretical and practical perspective.[52] Macromolecular and nanoscale systems exhibiting superstructural chirality abound. In biological contexts, chiral helices can be found in DNA and proteins; twisted beta sheets form helical columns[53], as in silk, and modern synthetic analogues have appeared[54, 55]. In materials science, examples include liquid crystalline cholesteric phases[31] and chiral smectic phases[14] formed from bent-core molecules. These systems each exhibit chirality that goes beyond an individual unit and extends into a superstructure or over an entire phase. Generally, the chirality is derived from the chirality of individual molecular components. Surprisingly, however, chirality can also arise spontaneously in systems that are composed of achiral molecules. Experimental examples of chiral superstructures formed from achiral substituents include liquid crystalline banana phases[14, 41], fatty acid salt crystals[56], and π-stacked helical hydrogen-bonded amide stacks[57]. Similarly, stable chiral structures can be formed from achiral particles due to templating[58] and stirring[59]. In simulation and theory, structural and superstructural chirality is usually modelled with the addition of a potential explicitly favoring twisting. As examples, Memmer *et al.*[60] found that chiral Gay-Berne[61] particles form helices, whereas achiral Gay-Berne particles do not[62], Grason and Bruinsma[63] modeled biopolymer bundle aggregates by adding a twisting term to a free-energy expression, and Tepper and Voth[3] reproduced the DNA double helix using a model that incorporated frustration that was best satisfied in the double helix structure. Twisted structures have also been found in simulation systems where interactions are not explicitly chiral. Fejer and Wales[64] cataloged the lowest potential energy structures of clusters of discotic Gay-Berne-like particles and found helical structures. Further, Chakrabarti and Wales[65] demonstrated the formation of helical columnar phases

using particles which interact via a Gay-Berne variant[66]. Also, Horsch *et al.* predicted a hexagonal chiral cylinder phase in a system composed of flexible achiral polymer-tethered nanorods[25, 26]. All these examples have not depended on explicit chiral terms in the potential model, and are more similar to the approach taken in this thesis[52, 67, 4], where a simplified coarse-grained model is used to study the phase behavior of bent-core and linear molecules. These works will be discussed in chapters 4-6.

1.1.3 SELF-ASSEMBLY OF LIQUID CRYSTALS AND CHIRAL SUPERSTRUCTUES BY COARSE-GRAINED BENT-CORE OR LINEAR MOLECULES

In chapter 4, the phase behavior of a rigid achiral bent-core model system is explored (see Fig. 4a) [52]. Nematic and smectic phases form at higher densities, whereas micelles and columns composed of chiral clusters of these molecules self-assemble at lower densities. No nucleation mechanism requiring transient chirality is possible in the formation of these chiral superstructures due to the rigid achiral nature of the substituents. The chiral micelles are shown to be minima of the potential energy surface using energy minimization[68] and parallel tempering simulations[69]. Chiral dopants are found to induce the system to adopt a consistent chiral twist direction, which is the first molecular scale computer simulation of this effect[52].

In the work in chapter 5[67], the phase behavior of a coarse-grained linear rigid molecule system (see Fig. 8a) with the same potential type as that in chapter 4 was studied using molecular dynamics simulations in the isothermal-isobaric (NPT) ensemble. Compared to bent-core model, this linear rigid model is less anisotropic in shape (because it is linear). Thus, the shape anisotropy effect on the phase behavior of this model can be investigated. Simulation results for the linear rigid model are found to be similar to the rigid bent-core model. Chiral phases are found to self-assemble at low pressures, and Monte Carlo parallel tempering[69] and energy minimization simulations[68] demonstrate that chiral superstructures are minima of the potential energy surface for these rigid linear molecules. Liquid crystalline phases, including nematic (N), smectic A (SmA), smectic C (SmC), and smectic

I (SmI) phases formed at high pressures. In addition, both chiral superstructures and tiltled smectic phases have been found to be tunable by varying the spacing between interaction centres in the linear molecule. Further more, superstructural chirality appears as a common theme in systems composed of achiral linear particles with Lennnard-Jones interaction sites that are appropriately spaced.

In the final work with the coarse-grained model simulation[4] (chapter 6), a comprehensive computational study on phase behaviors of bent-core molecules at different bending angle γ and different arm length ratio N_A / N_B is performed. It is found that increasing the bending angle γ favors the formation of chiral phases and liquid crystalline phases. At small bending angles, the steric effect from the purely repulsive Weeks-Chandler-Andersen (WCA) particles can inhibit formation of chiral phases and liquid crystalline phases. However, these phases can be recovered by decreasing the number of WCA particles per molecule. These results show that chiral phases and liquid crystalline phases can be tuned by altering the bending angle and/or the arm length ratio.

In summary, the part of coarse-grained model simulations is organized as follows. The theoretical background of the molecular dynamics simulations and Monte Carlo parallel tempering simulations are provided in chapter 2 and chapter 3, respectively. Then the simulation results for coarse-grained bent-core or linear model systems are shown in chapters 4-6.

1.2 FROM COARSE-GRAINED TO FULLY ATOMISTIC MODELS

After completing the comprehensive simulation study of phase behavior of coarse-grained bent-core molecules, atomistic simulations are then used to study the phase behavior of liquid crystalline molecules. Although coarse-grained methods are capable of determining much of the essential physics required for the formation of liquid crystalline phases, they are incapable of capturing the effects of subtle chemical changes to the molecular structure of a molecule that can result in large changes in the phases experimentally observed in a series of compounds[70]. In these cases, atomistic resolution models are required to study

and understand the behavior.

Atomistic resolution models present molecules at an all atom level, thus are capable of capturing the macroscopic phase behavior change due to a very small variation on the molecular structure of a liquid crystal molecule.[70] However, due to the relatively long time and length scales required for liquid crystal phase formation, and the need for accurate force fields, atomistic level modeling of liquid crystalline systems is challenging[70]; but with the aid of larger and faster computers, and better parallel algorithms, the ability of scientists to tackle these systems is increasing.

1.2.1 RECENT DEVELOPMENT OF ATOMISTIC SIMULATION OF LIQUID CRYSTALS

A number of notable atomistic studies of nematic phases have been performed. These include Wilson and Allen's simulations of CCH5[71, 72], the first thousand molecule atomistic simulation of a liquid crystal by Cook and Wilson[73], Pelaez and Wilson's study of a biaxial nematic phase[74], Berardi *et al.*'s study of the odd-even effect in nematic phases[75], and Cheung *et al.*'s calculation of flexoelectric coefficents for a nematic phase[76]. Atomistic and semi-atomistic studies of smectic liquid crystal phases include those by Lansac *et al.*[77], simulations of a series of the 4-*n*-alkyl-4′-cyanobiphenyls (*n*CB)[78], the recent simulations of 2-(4-butyloxyphenyl)-5-octyloxypyrimidine (2PhP) and 5-(4-butyloxyphenyl)-2-octyloxypyrimidine (5PhP) by Pecheanu and Cann[79], and sexithiophene (T6) by Pizzirusso *et al.*[80]. However, to fully demonstrate smectic phase formation one needs to assemble the system from a more disordered state, and to conduct the simulation with system sizes sufficient to form at least three smectic layers in order to rule out the influence of periodic image interactions. Previous atomistic smectic phase simulations have not satisfied one or both of these criteria. Concurrently, efforts have also been made to develop accurate atomistic force fields for liquid crystals. For example, Wilson's research group have developed a liquid crystal force field (LCFF)[8], based on the OPLS-AA force field[81], which has been shown to give good results for a number of different systems[73, 82, 76, 74]. Zannoni and co-workers[83] have developed an algorithm to derive effective charges for liquid crystals in order to speed

up the calculations of long electrostatic interactions. Bizzarri and co-workers[84] have also developed a force field for a nematic phase formed by n-cyanobiphenyls using a fragmentation reconstruction method[85]. And recently Pecheanu and Cann[79] have developed a force field for 2-(4-butyloxyphenyl)-5-octyloxypyrimidine (2PhP) and 5-(4-butyloxyphenyl)-2-octyloxypyrimidine (5PhP).

By using the liquid crystal force field (LCFF) of Wilson and co-workers[8], this work here has performed the largest atomistic simulations of liquid crystals to date, and demonstrated for the first time, to our knowledge, the formation of smectic phases with four smectic layers from an isotropic liquid state at the all atom level. Both a series of single component liquid crystals (chapter 7) and binary liquid crystal mixtures (chapter 8) are studied in this thesis.

1.2.2 SELF-ASSEMBLY OF LIQUID CRYSTALS BY FULLY ATOMISTIC SIMULATIONS

The single component liquid crystals are a series of di-, tri-, and tetrafluoroterphenyls (chapter 7). The choice of system is inspired by the experimental work of Gasowska *et al.*[1] where the substitution of hydrogen atoms with fluorine atoms in the aromatic ring groups of terphenyl molecules was found to destabilize the smectic phases that were observed for the difluoroterphenyl molecule. The simulation results are in good agreement with the experiment[1], and show that atomistic simulations are capable of capturing macroscopic changes in the phase behavior of a series of compounds, even when only a small variation in molecular structure is made, in this case the regiospecific substitution of one or two hydrogen atoms with fluorine atoms.

In chapter 8, liquid crystal mixtures of alkoxy substituted phenylpyrimidines 2-[4-(butyloxy)phenyl]-5-(octyloxy)pyrimidine (2PhP) and 2-[4-(tetradecyloxy)phenyl]-5-(tetradecyloxy) pyrimidine (PhP14) are studied using molecular dynamics simulations in the isothermal-isobaric (NPT) ensemble at the all atom level. Compared to atomistic simulations of single component liquid crystals, atomistic simulations of liquid crystal mixtures are more challenging because polydisperity in the mixtures frustrates the self-assembly of the molecules into ordered smectic layers[86], thus requiring longer equilibration times and making the compu-

tation more expensive. The simulation results are in good agreement with the experimental findings of Kapernaum *et al.*[2], thus showing that atomistic simulations are capable of reproducing the phase behaviour of liquid crystal mixtures and can also provide microscopic details regarding the mechanisms that govern phase stability.

2.0 LIOUVILLE FORMULATION OF TIME-REVERSIBLE DYNAMICS IN MOLECULAR DYNAMICS SIMULATION

2.1 INTRODUCTION

Molecular dynamics simulations determine the time evolution of a system by integrating the equations of motion.[87, 88] Molecular dynamics simulations can provide useful information for molecular systems at equilibrium. For example, these simulations can allow one to calculate pairwise correlation distribution functions which provide structural information[67, 4, 89, 90]. Phase transition information can be obtained from temperature (or pressure) annealing,[52, 67, 4, 90] and time correlation functions can be obtained and used to calculate transport coefficients[87, 88]. Further, the motion of the component particles during the time evolution of a system can be observed by visulization tools, such as vmd[91], BALLView[92, 93], Chimera[94], RASMOL[95], etc. NVT (constant number of particles, N; volume V; and temperature, T) and NPT (constant number of particles, N; pressure, P; and temperature, T) simulations are essential as most experiments are conducted under conditions of constant temperature and/or pressure.[87, 88, 96, 97, 98, 99, 100, 101, 102, 103] Several methods for temperature and pressure control in the canonical (NVT) and isothermal-isobaric (NPT) ensembles were developed in the 1980's, including stochastic methods[96], extended system methods[97, 98] and others[99, 100, 101, 102]. The stochastic methods control the system temperature by stochastic collision with a heat bath. This ensures that all accessible energy surfaces can be visited according to their Boltzmann weight.[87, 88, 96] While it gives the correct canonical distribution, the stochastic collisions make the dynamics discontinuous.[87, 88, 104] The extended method uses an extended Hamiltonian system to give the correct canonical ensemble. [97, 98, 104] It works well for large (ergodic) systems, but fails for small

or stiff systems.[98, 104] Based on Nosé's extended Hamiltonian method[97, 98], Martyna and Tuckerman[103, 104, 105, 106, 107, 108, 109, 110] developed a time-reversible algorithm by using a Liouville formulation for different ensembles. By using several Nosé-Hoover thermostat chains instead of one chain, this method is able to generate the correct canonical distribution for small or stiff systems. Using the Liouville formulation and a quaternion integration scheme in an extended Hamiltonian[97, 98, 103, 104], Miller *et al.*[111] developed a time-reversible symplectic quaternion scheme, NO_SQUISH, for rigid-body systems.

In the simulations presented in chapters 4-6, the systems are made of entirely rigid coarse-grained achiral bent-core molecules[52, 4] or linear rigid molecules[67]. The equations of motion were integrated by using the NO_SQUISH integrator of Miller *et al.*[111], and an operator splitting similar to that proposed by Kamberaj *et al.* [112] was used in the canonical (NVT) and the isothermal-isobaric (NPT) ensembles. All simulations are conducted by using a home-made simulation package in our group: The Pitt Molecular Modelling Package (PMM). In this chapter, the mathematial background for the Liouville formulation of time-reversible dynamics[103, 104, 105, 106, 107, 108, 109, 110] in the NVT and NPT simulations, and the NO_SQUISH integration scheme for rigid-body systems[111, 112] is introduced. Then the method of combining the NO_SQUISH approach with Martyna and Tuckerman's method for rigid-body systems in the NVT and NPT simulations is described.

2.2 THE LIOUVILLE FORMULATION OF A TIME-REVERSIBLE ALGORITHM IN A HAMILTONIAN SYSTEM

The Liouville equation describes the time evolution of the phase space distribution function. [113, 114] For a system of N particles, the dynamical state is defined by a space made of the $3N$-dimensional momentum coordinates $\mathbf{p}_1, \cdots, \mathbf{p}_N$ with $\mathbf{p}_j = p_j^x, p_j^y, p_j^z$, and the $3N$-dimensional spatial coordinates $\mathbf{q}_1, \cdots, \mathbf{q}_N$ with $\mathbf{q}_j = q_j^x, q_j^y, q_j^z$. Such a space is called phase space. A phase point is a point in the phase space which determines the state of the system at a time t. During the time evoluation of phase space, the movement of each phase point can be determined by the equations of motion.[113, 114] An ensemble is made of many phase

points which have the same variables such as temperature, total energy, pressure, volume, chemical potential, and number of particles. For example, the canonical ensemble (NVT) has constant number of particles, volume and temperature. In an ensemble, each phase point is distributed according to the phase space distribution function $f(\mathbf{p}(t), \mathbf{q}(t))$, where $\mathbf{p}(t)$ is the shorthand notation for $\sum_{j=1}^{N} \mathbf{p}_j$ and $\mathbf{q}(t)$ for $\sum_{j=1}^{N} \mathbf{q}_j$. Because no phase points can be destroyed or created during the evolution, the total phase space distribution is conserved, as stated by Liouville's theorem[87, 88, 113, 114]:

$$df(\mathbf{p}(t), \mathbf{q}(t))/dt = 0 \tag{2.1}$$

where d/dt denotes the total derivative with respect to time, and can be expanded as

$$d/dt = \partial/\partial t + (\sum_{j=1}^{N} \frac{\mathbf{p}_j}{m_j} \cdot \bigtriangledown_{\mathbf{q}_j} + \sum_{j=1}^{N} \mathbf{F}_j \cdot \bigtriangledown_{\mathbf{p}_j}) \tag{2.2}$$

where $\mathbf{q}_j$, $\mathbf{p}_j$, $\bigtriangledown_{\mathbf{q}_j}$, $\bigtriangledown_{\mathbf{p}_j}$, $\mathbf{F}_j$ and m_j are the position, momentum, gradient with respect to the position, gradient with respect to the moment, the total force, and the mass of the jth particle, respectively. $(\sum_{j=1}^{N} \frac{\mathbf{p}_j}{m_j} \cdot \bigtriangledown_{\mathbf{q}_j})$ is related to the time evolution of position, and $(\sum_{j=1}^{N} \mathbf{F}_j \cdot \bigtriangledown_{\mathbf{p}_j})$ is related to the time evolution of momentum.

Combining eqs. (2.1) and (2.2) leads to the Liouville equation in a Hamiltonian system containing N particles[113, 114]:

$$\begin{aligned} \partial f/\partial t &= -(\sum_{j=1}^{N} \frac{\mathbf{p}_j}{m_j} \cdot \bigtriangledown_{\mathbf{q}_j} + \sum_{j=1}^{N} \mathbf{F}_j \cdot \bigtriangledown_{\mathbf{p}_j}) f \\ &= -i\hat{L} f \end{aligned} \tag{2.3}$$

where $i\hat{L}$ is the Liouville operator.

The Liouville operator can be separated into two parts[87]:

$$i\hat{L} = i\hat{L}_r + i\hat{L}_p \tag{2.4}$$

where $i\hat{L}r = (\sum_{j=1}^{N} \frac{\mathbf{p}_j}{m_j} \cdot \bigtriangledown_{\mathbf{q}_j})$, and $i\hat{L}_p = (\sum_{j=1}^{N} \mathbf{F}_j \cdot \bigtriangledown_{\mathbf{p}_j})$.

The solution of eq. (2.3) can be obtained by using the expression of eq. (2.4)[87, 103, 114]:

$$f(\mathbf{p}(t), \mathbf{q}(t)) = \exp(i\hat{L}_r t + i\hat{L}_p t) f(\mathbf{p}(0), \mathbf{q}(0)) \tag{2.5}$$

where $f(\mathbf{p}(0), \mathbf{q}(0))$ denotes the phase space distribution at time $t = 0$, and $f(\mathbf{p}(t), \mathbf{q}(t))$ denotes the phase space distribution at time t.

Eq. (2.5) indicates that, given an initial phase space function $f(\mathbf{p}(0), \mathbf{q}(0))$, the trajectory (a trajectory is the path for the movement of a system in phase space) for the evolution of phase space can be obtained by applying the Liouville operator. Because $[i\hat{L}_r, i\hat{L}_p] \neq 0$, that is, $i\hat{L}_r i\hat{L}_p - i\hat{L}_p i\hat{L}_r \neq 0$, $i\hat{L}_r$ and $i\hat{L}_p$ do not commute. For two noncommuting operators $\hat{A}$ and $\hat{B}$:

$$\exp(\hat{A} + \hat{B}) \quad \neq \quad \exp(\hat{A})\exp(\hat{B}) \tag{2.6}$$

In order to solve this problem, a Trotter expansion can be applied to decompose eq. (2.6), which yields[115, 116]

$$\exp(\hat{A} + \hat{B}) \quad = \quad \lim_{P\to\infty} (\exp(\frac{\hat{A}}{2P}) \exp(\frac{\hat{B}}{P}) \exp(\frac{\hat{A}}{2P}))^P \tag{2.7}$$

Following eq. (2.7), $\exp i\hat{L}t$ can be expressed as[103, 104, 105]

$$\begin{aligned} \exp(i\hat{L}t) &= \exp(i\hat{L}_p t + i\hat{L}_r t) \\ &= \lim_{P\to\infty} (\exp(\frac{i\hat{L}_p}{2P}) \exp(\frac{i\hat{L}_r}{P}) \exp(\frac{i\hat{L}_p}{2P}))^P \end{aligned} \tag{2.8}$$

For a large but finite P,

$$\exp(i\hat{L}t) \quad = \quad (\exp(\frac{\Delta t}{2} i\hat{L}_p) \exp(i\hat{L}_r \Delta t)(\exp(\frac{\Delta t}{2} i\hat{L}_p))^P + O(t\Delta t^2) \tag{2.9}$$

where $\Delta t = t/P$, which corresponds to the length of one time-step in molecular dynamics simulation, t corresponds to the total simulation time, and P is the total number of time steps. $O(t\Delta t^2)$ indicates that the operator is accurate to the second order; also note that the error in the evolution increases linearly with time t[111].

From eq. (2.9), a time-step propagator $G(\Delta t)$ can be defined as

$$\begin{aligned} G(\Delta t) &= \exp(i\hat{L}t) \\ &= \exp(\frac{\Delta t}{2} i\hat{L}_p) \exp(i\hat{L}_r \Delta t) \exp(\frac{\Delta t}{2} i\hat{L}_p) \end{aligned} \tag{2.10}$$

Furthermore, based on eq. (2.10), it is easy to show that

$$\begin{aligned} G^{-1}(\Delta t) &= \exp(-i\hat{L}t) \\ &= G(-\Delta t) \quad \Rightarrow \\ G(\Delta t)G^{-1}(\Delta t) &= 1 \end{aligned} \tag{2.11}$$

Here the fact that $i^2 = -1$ is used. Now, if an operator such as $G(\Delta t)G^{-1}(\Delta t)$ is applied to a phase space distribution function $f(\mathbf{p}(0), \mathbf{q}(0))$ at initial time, it follows that

$$\begin{aligned} G^{-1}(\Delta t)G(\Delta t)f(\mathbf{p}(0), \mathbf{q}(0)) &= G^{-1}(\Delta t)f(\mathbf{p}(t), \mathbf{q}(t)) \\ &= f(\mathbf{p}(0), \mathbf{q}(0)) \end{aligned} \tag{2.12}$$

This shows that after applying an operator by a time Δt, the phase space evolves to $f(\mathbf{p}(t), \mathbf{q}(t))$, then applying the operator reversibly by a time Δt, the phase space has to evolve back to its original state, $f(\mathbf{p}(0), \mathbf{q}(0))$. Thus, Liouville operator can generate time-reversible dynamics.[115, 117]

The following equations describe the evolution of phase space at initial time, $f(\mathbf{p}(0), \mathbf{q}(0))$ to time Δt, $f(\mathbf{p}(\Delta t), \mathbf{q}(\Delta t))$, by applying the one time-step Liouville operator $G(\Delta t)$:[87]

$$\begin{aligned} &\exp(\frac{\Delta t}{2}i\hat{L}_p)\exp(i\hat{L}_r\Delta t)\exp(\frac{\Delta t}{2}i\hat{L}_p)f(\mathbf{p}(0), \mathbf{q}(0)) \\ \equiv &\exp(\frac{\Delta t}{2}i\hat{L}_p)\exp(i\hat{L}_r\Delta t)\exp(\frac{\Delta t}{2}\dot{\mathbf{p}}(0)\frac{\partial}{\partial \mathbf{p}})f(\mathbf{p}(0), \mathbf{q}(0)) \\ = &\exp(\frac{\Delta t}{2}i\hat{L}_p)\exp(i\hat{L}_r\Delta t)f[\mathbf{p}(0) + \dot{\mathbf{p}}(0)\frac{\Delta t}{2}, \mathbf{q}(0)] \\ = &\exp(\frac{\Delta t}{2}i\hat{L}_p)\exp(\Delta t\dot{\mathbf{q}}(\Delta t/2)\frac{\partial}{\partial \mathbf{q}})f[\mathbf{p}(\frac{\Delta t}{2}), \mathbf{q}(0)] \\ = &\exp(\frac{\Delta t}{2}i\hat{L}_p)f[\mathbf{p}(\frac{\Delta t}{2}), \mathbf{q}(0) + \Delta t\dot{\mathbf{q}}(\Delta t/2)] \\ = &\exp(\frac{\Delta t}{2}\dot{\mathbf{p}}(\Delta t)\frac{\partial}{\partial \mathbf{q}})f[\mathbf{p}(\frac{\Delta t}{2}), \dot{\mathbf{q}}(\Delta t)] \\ = &f[\mathbf{p}(\frac{\Delta t}{2}) + \dot{\mathbf{p}}(\Delta t)\frac{\Delta t}{2}, \dot{\mathbf{q}}(\Delta t)] \\ = &f[\mathbf{p}(\Delta t), \mathbf{q}(\Delta t)] \end{aligned} \tag{2.13}$$

Eq. (2.13) shows that after one time-step the momentum $\mathbf{p}$ and position $\mathbf{q}$ evolve as

$$\begin{aligned} \mathbf{p}(\Delta t) &= \mathbf{p}(0) + \dot{\mathbf{p}}(0)\frac{\Delta t}{2} + \dot{\mathbf{p}}(\Delta t)\frac{\Delta t}{2} \\ \mathbf{q}(\Delta t) &= \mathbf{q}(0) + \dot{\mathbf{q}}(\Delta t/2)\Delta t \end{aligned} \tag{2.14}$$

These are the exact equations of the velocity Verlet algorithm, so the velocity Verlet algorithm can generate reversible dynamics.[118, 119] Therefore, the Verlet algorithm is a special case of a Trotter expansion of the Louville operator.[87] In a typical molecular dynamics simulation, one proceeds with the following steps. First, choose a forcefield for the system, like AMBER[120, 121], CHARMM[122], MM4[123], OPLS[81], etc. Second, generate the initial state, which corresponds to the phase space distribution function $f(\mathbf{p}(0), \mathbf{q}(0))$. Third, apply the evolution operator full time propagator operator $\exp(i\hat{L}t)$ to the phase space until the system reaches equilibrium. Finally, after equilibration, conduct the measurements based on the output, which corresponds to the phase space distribution $f(\mathbf{p}(t), \mathbf{q}(t))$.

2.3 THE LIOUVILLE FORMULATION IN A NON-HAMILTONIAN SYSTEM

Defining all the phase space coordinates for a system of N particles at time $t = 0$ as $\eta(\mathbf{t_0})$, the phase space volume can be defined as[87, 114, 124],

$$\begin{aligned} d\eta(\mathbf{t_0}) &= d\mathbf{q}d\mathbf{p} \\ &= dq_1 \cdots dq_{3N} \cdots dp_1 \cdots dp_{3N} \end{aligned} \tag{2.15}$$

where q_i, p_i are the position and momentum for the ith particle at the initial time.

At time t, $\eta(\mathbf{t_0})$ evolves to $\eta(\mathbf{t})$, and the phase space volume becomes[87, 114, 124]

$$\begin{aligned} d\eta(\mathbf{t}) &= d\mathbf{Q}d\mathbf{P} \\ &= dQ_1 \cdots dQ_{3N} \cdots dP_1 \cdots dP_{3N} \end{aligned} \tag{2.16}$$

where Q_i and P_i are the position and momentum for the ith particle at time t.

Based on the change of variables theorem, these two volume elements are related by a Jacobian[125]

$$\begin{aligned} d\eta(t_0) &= |\det(\mathbf{M})| d\eta(t) \\ &= J(\eta_t, \eta_0) d\eta(t) \end{aligned} \tag{2.17}$$

where "det" denotes the determinant, and $\mathbf{M}$ is the Jacobian matrix for the transformation:

$$\begin{aligned} \mathbf{M} &= \frac{\partial(\eta(t_0))}{\partial(\eta(t))} \\ &= \begin{pmatrix} \frac{\partial q_1}{\partial Q_1} & \cdots & \frac{\partial q_1}{\partial P_{3N}} \\ \vdots & \ddots & \vdots \\ \frac{\partial p_{3N}}{\partial Q_1} & \cdots & \frac{\partial p_{3N}}{\partial P_{3N}} \end{pmatrix} \end{aligned} \tag{2.18}$$

and $J(\eta_t, \eta_0)$ in eq. (2.17) is the Jacobian, which is the determinant of the Jacobian matrix $\mathbf{M}$.

In Hamiltonian systems, the equations of motion can be written as[113, 114, 124, 88, 87]

$$\dot{\eta} = \omega \frac{\partial H}{\partial \eta} \tag{2.19}$$

where $\eta = \begin{pmatrix} \mathbf{q} \\ \mathbf{p} \end{pmatrix}$, and ω is the phase space geometric tensor, which is skew-symmetric in a Hamiltonian system[124]

$$\omega = \begin{pmatrix} 0 & 1 \\ -1 & 0 \end{pmatrix} \tag{2.20}$$

Based on the eq. (2.19), the Liouville equation in Hamiltonian system can be rewritten as

$$\frac{\partial f}{\partial t} + \bigtriangledown \cdot (\dot{\eta} f) = 0 \tag{2.21}$$

For the time evolution of phase space from $\eta(0)$ to $\eta(t)$, the Jocobian matrix $\mathbf{M}$ follows a symplectic condition[87]

$$\mathbf{M} \omega \widetilde{\mathbf{M}} = \omega \tag{2.22}$$

where $\widetilde{\mathbf{M}}$ is the transpose of $\mathbf{M}$. Note that for a system to follow symplectic condition, it must be a Hamiltonian system.

Based on the symplectic condition, the Jacobian $J(\eta_t, \eta_0)$ $(= |\det(\mathbf{M})|)$ can be calculated by taking the determinant of both sides of the symplectic condition

$$\begin{aligned} \det(\mathbf{M}\omega\widetilde{\mathbf{M}}) &= \det(\omega) \\ \det{}^2(\mathbf{M})\det(\omega) &= \det(\omega) \\ \Rightarrow \det(\mathbf{M}) &= \pm 1 \\ \Rightarrow J(\eta_t, \eta_0) = |\det(\mathbf{M})| &= 1 \end{aligned} \tag{2.23}$$

Because $J(\eta_t, \eta_0) = 1$, eq. (2.17) can be simplified as

$$d\eta(t_0) = d\eta(t) \tag{2.24}$$

which shows the phase space volume is preserved during the time evolution, and therefore, the phase space in a Hamiltonian system is incompressible.

In a non-Hamiltonian system, however, the phase space has non-unity compressibility, and the Jacobian is not equal to 1 (nor even a constant). The phase space compressibility of the system can be derived from the time dependence of the Jacobian[87, 107, 108]

$$\frac{dJ(\eta_t, \eta_0)}{dt} = \kappa(\eta_t, t)J(\eta_t, \eta_0) \tag{2.25}$$

where $\kappa(\eta_t, t)$ is the phase space compressibility, and is equal to zero in a Hamiltonian system, which means it is incompressible. $\kappa(\eta_t, t)$ is defined as

$$\kappa(\eta_t, t) \equiv \bigtriangledown_\eta \cdot \dot{\eta} \tag{2.26}$$

Integration of $\kappa(\eta_t, t)$ over time gives the solution for eq. (2.25) as[87, 107, 108, 109, 110]

$$J(\eta_t, \eta_0) = \exp\left(\int_0^t \kappa(\eta_s, s)ds\right) = \exp(w(\eta_t, t) - w(\eta_0, 0)) \equiv \frac{\sqrt{g(\eta_0, 0)}}{\sqrt{g(\eta_t, t)}} \tag{2.27}$$

Substituting eq. (2.27) into eq. (2.17) gives the phase spave volume measurement in a non-Hamiltonian systems as

$$\sqrt{g(\eta_t, t)}d\eta(t) \quad = \quad \sqrt{g(\eta_0, 0)}d\eta(0) \tag{2.28}$$

which defines an invariant measurement in the phase space.

In order to make an invariant measurement in a non-Hamiltonian system, $\sqrt{g}$ must be included in the Liouville equation. Then based on eq. (2.21), the Liouville equation in the Hamiltonian system can be modified in the non-Hamiltonian system as

$$\frac{\partial f\sqrt{g}}{\partial t} + \bigtriangledown\cdot(\dot{\eta} f\sqrt{g}) \quad = \quad 0 \tag{2.29}$$

2.4 NON-HAMILTONIAN SIMULATION IN THE CANONICAL ENSEMBLE (NVT)

Originally, molecular dynamics simulations were most commonly conducted in a micro-canonical ensemble (NVE, constant number of system particles, N; volume, V; and total energy, E), in which the Hamiltonian (Newtonian) equations of motion for the system particles can be solved numerically. This method has limited applications because most real experiments are conducted in the canonical (NVT) or the isothermal-isobaric (NPT) ensemble.[88, 87, 96, 97] In order to solve this problem, "extended phase space" methods, which are non-Hamiltonian due to the inclusion of the extended system, are often used in molecular dynamics simulations to generate the correct canonical ensemble or isothermal-isobaric ensemble.[88, 87] In an extended system, some extra variables are incorporated into the system in order to generate the correct ensemble. Thus, the equations of motion must include the contributions from these additions variables. Based on a modified extended Hamiltonian method of Nosé[126], Martyna and Tuckerman have shown that a Nosé-Hoover thermostat chain gives the correct canonical distribution, even for small or stiff systems, which the Nosé method fails to do.[98, 104] The equations of motion for an extended

Hamiltonian system coupled with a Nosé-Hoover chain containing M thermostats are given by[104, 105, 106]:

$$\begin{aligned}
\dot{\mathbf{r}}_i &= \frac{\mathbf{p}_i}{m_i}, \\
\dot{\mathbf{p}}_i &= \mathbf{F}_i - \frac{p_{\xi_1}}{Q_1}\mathbf{p}_i, \\
\dot{\xi}_k &= \frac{p_{\xi_k}}{Q_k}, \quad k = 1, \cdots, M, \\
\dot{p}_{\xi_1} &= (\sum_{i=1}^{N} \frac{\mathbf{p}_i^2}{m_i} - N_f k_B T) - \frac{p_{\xi_2}}{Q_2} p_{\xi_1}, \\
\dot{p}_{\xi_k} &= (\frac{p_{\xi_{k-1}}^2}{Q_{k-1}} - k_B T) - p_{\xi_k}, \quad \text{for} \quad k = 2, \cdots, M-1, \\
\dot{p}_{\xi_M} &= \frac{p_{\xi_{M-1}}^2}{Q_{M-1}} - k_B T
\end{aligned} \tag{2.30}$$

where $\mathbf{r}_i$, $\mathbf{p}_i$, $\mathbf{F}_i$ and m_i are position, momentum, force and mass for the ith particle in the system; ξ_k, p_{ξ_k} and Q_k are position, momentum and mass for the kth thermostat; N_f is the number of degrees of freedom for the system, k_B is the Boltzmann constant.

The conserved energy for the system is[104, 106]

$$H' = H(\mathbf{r}, \mathbf{p}) + \sum_{k=1}^{M} \frac{p_{\xi_k}^2}{2Q_k} + N_f k_B T \xi_1 + \sum_{k=2}^{M} k_B T \xi_k \tag{2.31}$$

where $H(\mathbf{r}, \mathbf{p})$ is the total energy for the original system which only includes the system particles' positions $\mathbf{r}$ and momentum $\mathbf{p}$. $\sum_{k=1} M \frac{p_{\xi_k}^2}{2Q_k}$ is the kinetic energy, and $N_f k_B T \xi_1 + \sum_{k=2}^{M} k_B T \xi_k$ is the potential energy for the M Nosé-Hoover chain thermostats.

In eq. (2.31), H' is not Hamiltonian because the equations of motion (see eq. (2.19)) cannot be derived from it. The phase space compressibility (see eq. (2.26)) can be expanded as[104, 105, 106]

$$\begin{aligned}
\kappa(\eta) &\equiv \bigtriangledown_\eta \cdot \dot{\eta} \\
&= -N_f \dot{\xi}_1 - \sum_{i=2}^{M} \dot{\xi}_i
\end{aligned} \tag{2.32}$$

This shows that the compressibility of the extended system is from the thermostat. Substituting eq. (2.32) into eq. (2.25) gives the expression of the Jacobian $J(\eta)$ as[87, 106, 108]

$$J(\eta) = \exp(N_f \xi_1 + \xi_c) \tag{2.33}$$

where $\xi_c = \sum_{k=2}^{M} \xi_k$, and is defined as the thermostat center.

Based on eq. (2.33), only the first chain, ξ_1, and the thermostat center, ξ_c, are coupled to the system. The partition function for the extended system can be expressed as[87, 106, 110]

$$\Omega(N,V,C) = \int d\mathbf{p} \int d\mathbf{r} \int d\xi_1 \int d\xi_c \int dp_{\xi_1} \cdots \int dp_{\xi_M} J(\eta) \times \delta(C - H') \quad (2.34)$$

where the δ function is

$$\delta(C - H') = \begin{cases} 1 & , C = H' \\ 0 & , C \neq H'. \end{cases} \quad (2.35)$$

From eq. (2.35), it is obvious that in order to generate the correct ensemble, C must be equal to H'. Also because it is non-Hamiltonian, the Jacobian must be included to define an invariant phase space volume measurement (see eq. (2.29)).

Integeration of eq. (2.34) over ξ_1 and ξ_c by using the δ function gives[87, 106, 110]

$$\begin{aligned} \Omega(N,V,C) &= \frac{\exp(\beta C)}{N_f k_B T} \int d\mathbf{p} \int d\mathbf{r} \exp\left[-\beta H(\mathbf{r},\mathbf{p})\right] \int dp_{\xi_1} \times \cdots \times \int dp_{\xi_M} \exp\left[-\beta \sum_{k=1}^{M} \frac{p_{\xi_k}^2}{2Q_k}\right] \\ &= \text{constant} \times \int d\mathbf{p} \int d\mathbf{r} \exp\left[-\beta H(\mathbf{r},\mathbf{p})\right] \\ &\propto Q(N,V,T) \end{aligned} \quad (2.36)$$

where $\beta = 1/k_B T$. This demonstrates that the correct canonical ensemble is generated.

Constructing the Liouville operator from the equations of motion (see eq. (2.30)) gives[87, 108]

$$\begin{aligned} i\hat{L} &= \dot{\eta} \bigtriangledown_\eta \\ &= \sum_i \dot{\mathbf{r}}_i \cdot \bigtriangledown_{\mathbf{r}_i} + \sum_i \dot{\mathbf{p}}_i \cdot \bigtriangledown_{\mathbf{p}_i} + \sum_i \dot{\xi}_i \cdot \bigtriangledown_{\xi_i} + \sum_i \dot{p}_{\xi_i} \cdot \bigtriangledown_{p_{\xi_i}} \\ &= i\hat{L}_{NHC} + i\hat{L}_r + i\hat{L}_p \end{aligned} \quad (2.37)$$

where $i\hat{L}_r$ and $i\hat{L}_p$ are defined in eq. (2.4), and

$$i\hat{L}_{NHC} = \sum_i \dot{\xi}_i \cdot \bigtriangledown_{\xi_i} + \sum_i \dot{p}_{\xi_i} \cdot \bigtriangledown_{p_{\xi_i}} \quad (2.38)$$

Using a Trotter expansion, the propagator operator can be expressed as[108]

$$\begin{aligned} \exp(i\hat{L}\Delta t) &= \exp(i\hat{L}_{NHC}\frac{\Delta t}{2})\exp(i\hat{L}_p\frac{\Delta t}{2})\exp(i\hat{L}_r\Delta t) \\ &\quad \times \exp(i\hat{L}_p\frac{\Delta t}{2})\exp(i\hat{L}_{NHC}\frac{\Delta t}{2}) + O(\Delta t^3) \end{aligned} \tag{2.39}$$

where $O(\Delta t^3)$ is an infinitesimal asymptotic expression, which shows the operator is accurate to the second order.

Applying this propagator operator to the phase space generates time-reversible dynamics (see eqs. (2.11)-(2.12)) in the canonical ensemble.[87, 105, 106]

2.5 NON-HAMILTONIAN SIMULATION IN THE ISOTHERMAL-ISOBARIC ENSEMBLE (NPT)

In order to control the pressure in the NPT ensemble, the system must be allowed to change its volume.[88, 87] Thus, the volume must be introduced as a dynamic variable in the equations of motion.[88, 87, 96, 97, 127, 126] The temperature control is treated the same as in NVT simulations using Nosé-Hoover thermostat chains, and the pressure control is treated by introducing a barostat particle whose coordinate is related to the volume of the simulation box.[87, 106, 110] Based on the extended system method[88, 87, 96, 97], Martyna and Tuckerman developed an integration scheme which gives the desired NPT ensemble[105, 106, 107, 108]. The equations of motion for the extended system are[107, 108, 109, 110]

$$\begin{aligned}
\dot{\mathbf{r}}_i &= \frac{\mathbf{p}_i}{m_i} + \frac{p_\varepsilon}{W}\mathbf{r}_i, \\
\dot{\mathbf{p}}_i &= \mathbf{F}_i - (1+\frac{d}{N_f})\frac{p_\varepsilon}{W}\mathbf{p}_i - \frac{p_{\xi_1}}{Q_1}\mathbf{p}_i, \\
\dot{V} &= \frac{dVp_\varepsilon}{W}, \\
\dot{p}_\varepsilon &= dV(P_{int}-P_{ext}) + \frac{d}{N_f}\sum_{i=1}^{N}\frac{\mathbf{p}_i^2}{m_i} - \frac{p_{\xi_1}}{Q_1}p_\varepsilon, \\
\dot{\xi}_k &= \frac{p_{\xi_k}}{Q_k}, \quad \text{for} \quad k=1,\cdots,M, \\
\dot{p}_{\xi_1} &= \sum_{i=1} N\frac{\mathbf{p}_i^2}{m_i} + \frac{p_\varepsilon^2}{W} - (N_f+1)k_BT - \frac{p_{\xi_2}}{Q_2}p_{\xi_1}, \\
\dot{p}_{\xi_k} &= (\frac{p_{\xi_{k-1}}^2}{Q_{k-1}} - k_BT) - \frac{p_{\xi_{k+1}}}{Q_{k+1}}p_{\xi_k}, \quad \text{for} \quad k=2,\cdots,M-1, \\
\dot{p}_{\xi_M} &= (\frac{p_{\xi_{M-1}}^2}{Q_{M-1}} - k_BT)
\end{aligned} \tag{2.40}$$

where d is the system dimension, ξ_k, p_{ξ_k}, and Q_k represent the position, momentum and mass for the kth thermostat. ε, p_ε, and W are the position, momentum and mass for the barostat, and the barostat position ε is related to the volume of the system as

$$\varepsilon = \ln(\frac{V}{V(0)}) \tag{2.41}$$

where $V(0)$ is the system volume at initial time. P_{ext} is the external pressure, and P_{int} is the internal pressure for the system and is equal to

$$P_{\text{int}} = \frac{1}{dV}[\sum_{i=1}^{N}(\frac{\mathbf{p}_i^2}{m_i} + \mathbf{r}_i \cdot \mathbf{F}_i) - dV\frac{\partial U(V)}{\partial V}] \tag{2.42}$$

where U is the potential energy of the system. Note in the isothermal-isobaric ensemble, the constant pressure is P_{ext}. Also note in the equations of motion (eq. (2.40)), both the system and barostat are coupled to the first theromstat of the Nose-Hoover thermostat chain, though other choices can be made.[87, 106, 110]

The conserved energy for the extended system is[108, 109, 110]

$$H' = H(\mathbf{r}, \mathbf{p}) + \frac{{p_\varepsilon}^2}{2W} + \sum_{k=1}^{M}\frac{{p_{\xi_k}}^2}{2Q_k} + (N_f + 1)k_BT\xi_1 + k_BT\xi_c + P_{\text{ext}}V \tag{2.43}$$

where $\xi_c = \sum_{k=2}^{M}\xi_k$. $p_\varepsilon^2/2W$ and $P_{\text{ext}}V$ are the kinetic energy and potential energy of the barostat, respectively. Note that H' is not Hamiltonian because it cannot generate Hamiltonian dynamics (see previous comment on eq. (2.31)).

Following the same procedure as in the canonical ensemble (section 2.4), the Jacobian is calculated as

$$J(\eta) = \exp(N_f\xi_1 + \xi_c) \tag{2.44}$$

The partition function for the extended system is given by[108, 109, 110]

$$\Omega_{T,P_{\text{ext}}}(N, C) = \int dV \int d\mathbf{p} \int d\mathbf{r} \int d\xi_1 \int d\xi_c \int dp_{\xi_c} \times \cdots \times \int dp_{\xi_M} \int dp_\varepsilon J(\eta)\delta(C - H') \tag{2.45}$$

where $\Omega_{T,P_{\text{ext}}}(N, C)$ indicates the constant temperature, pressure and number of particles. The Jacobian $J(\eta)$ is included in order to make an invariant measurement.

Integration eq. (2.45) over ξ_1 and ξ_c using the δ function gives[87, 106, 110]

$$\begin{aligned}
\Omega_{T,P_{\rm ext}}(N,C) &= \frac{\exp(\beta C)}{N_f k_B T}\int dV \exp(P_{ext}V)\int d\mathbf{p}\int d\mathbf{r}\exp[-\beta H(\mathbf{r},\mathbf{p})]\int dp_\varepsilon \exp(\frac{-\beta p_\varepsilon^2}{2W}) \\
&\quad \times \int dp_{\xi_1}\cdots\int dp_{\xi_M}\exp[-\beta\sum_{k=1}^{M}\frac{p_{\xi_k}^2}{2Q_k}] \\
&= \text{constant}\times\int dV\exp(P_{ext}V)\int d\mathbf{p}\int d\mathbf{r}\exp[-\beta H(\mathbf{r},\mathbf{p})] \\
&\propto \Delta(N,P,T) \qquad (2.46)
\end{aligned}$$

This demonstrates that the correct NPT ensemble is generated. Applying the Liouville operator for the equations of motion gives[87, 108]

$$\begin{aligned}
i\hat{L} &= \dot{\eta}\bigtriangledown_\eta \\
&= \sum_i \dot{\mathbf{r}}_i\cdot\bigtriangledown_{\mathbf{r}_i}+\sum_i\dot{\mathbf{p}}_i\cdot\bigtriangledown_{\mathbf{p}_i}+\sum_i\dot{\xi}_i\cdot\bigtriangledown_{\xi_i}+\sum_i\dot{p}_{\xi_i}\cdot\bigtriangledown_{p_{\xi_i}}+\dot{V}\cdot\frac{\partial}{\partial V}+\dot{p}_\varepsilon\frac{\partial}{\partial p_\varepsilon} \\
&= \sum_{i=1}^{N}[\mathbf{v}_i+v_\varepsilon\mathbf{r}_i]\cdot\bigtriangledown_{\mathbf{r}_i}+\sum_{i=1}^{N}\dot{\mathbf{p}}_i\cdot\bigtriangledown_{\mathbf{r}_i}+i\hat{L}_{NHC}-(1+\frac{d}{N_f})\sum_{i=1}^{N}v_\varepsilon\mathbf{v}_i\cdot\bigtriangledown_{\mathbf{v}_i} \\
&\quad +[G_\varepsilon-v_\varepsilon v_\xi]\frac{\partial}{\partial v_\varepsilon}+v_\varepsilon\frac{\partial}{\partial_\varepsilon} \qquad (2.47)
\end{aligned}$$

where v_ε is the barostat velocity, and $i\hat{L}_{NHC}$ is defined in eq. (2.38) except for the force of the first thermostat G_1, because it is now copuled to both the system and the barostat. This is defined as

$$G_1=\frac{1}{Q}[\sum_{i=1}^{N}m_i\mathbf{v}_i^2+Wv_\varepsilon^2-(N_f+1)k_BT] \qquad (2.48)$$

The barostat force, G_ε, is defined as[87, 108]

$$G_\varepsilon=\frac{1}{W}[(1+\frac{d}{N_f})\sum_{i=1}^{N}m_i\mathbf{v}_i^2+\sum_{i=1}^{N}\mathbf{r}_i\cdot\mathbf{F}_i-dV\frac{\partial U(V)}{\partial V}-dP_{ext}V] \qquad (2.49)$$

Using a Trotter expansion, the propagator can be expressed as[87, 108]

$$\begin{aligned}
\exp(i\hat{L}\Delta t) &= \exp(i\hat{L}_{NHCP}\frac{\Delta t}{2})\exp(i\hat{L}_1\frac{\Delta t}{2})\exp(i\hat{L}_2\Delta t)\exp(i\hat{L}_1\frac{\Delta t}{2})\exp(i\hat{L}_{NHCP}\frac{\Delta t}{2})+O(\Delta t^3) \\
&= \exp(i\hat{L}_{NHC}\frac{\Delta t}{4})\exp(i\hat{L}_P\frac{\Delta t}{2})\exp(i\hat{L}_{NHC}\frac{\Delta t}{4})\exp(i\hat{L}_1\frac{\Delta t}{2})\exp(i\hat{L}_2\Delta t) \\
&\quad \times\exp(i\hat{L}_{NHC}\frac{\Delta t}{4})\exp(i\hat{L}_P\frac{\Delta t}{2})\exp(i\hat{L}_{NHC}\frac{\Delta t}{4}) \qquad (2.50)
\end{aligned}$$

where

$$
\begin{aligned}
i\hat{L}_1 &= i\hat{L}_p, \\
i\hat{L}_2 &= i\hat{L}_r + \sum_{i=1}^{N}[v_\varepsilon \mathbf{r}_i]\cdot\bigtriangledown_{\mathbf{r}_i} + v_\varepsilon\frac{\partial}{\partial\varepsilon}, \\
i\hat{L}_{NHCP} &= i\hat{L}_{NHC} + i\hat{L}_P, \\
i\hat{L}_P &= -(1+\frac{d}{N_f})\sum_{i=1}^{N} v_\varepsilon \mathbf{v}_i\cdot\bigtriangledown_{\mathbf{v}_i} + [G_\varepsilon - v_\varepsilon v_\xi]\frac{\partial}{\partial v_\varepsilon}
\end{aligned}
\tag{2.51}
$$

Applying this propagator to the phase space generates time-reversible dynamics in the NPT ensemble.[87, 106]

2.6 RIGID-BODY INTEGRATOR NO_SQUISH (NOVEL SYMPLECTIC QUATERNION SCHEME)

Although molecular system are not rigid bodies in reality,[88] it is desirable to treat some systems (or part of the same systems) as rigid-bodies in order to save computational time[128, 129], especially for large biophysical molecular dynamics simulations[111, 130, 131]. In this thesis, the bent-core molecules are treated as purely rigid because of two reasons, first, it saves computational time; second, the aromatic cores of the bent-core molecules can be treated as rigid based on their structural properties[14] (see Fig. 1).

The tranditional methods for treating rigid bodies like SHAKE[132] or RATTLE[133] solve the equations of motion iteratively, which cause the dynamics to be irreversible[134, 132, 133]. Other methods are either non-symplectic[135] or introduce many extra parameters[136]. By preserving the volume of phase space (see eq. (2.24)), the symplectic integrator is superior to the non-symplectic integrator because it possesses long-term energetic stability[136]. Based on the extended system method[96], Miller *et al.* developed a symplectic quaternion integration scheme (NO_SQUISH) using a Liouville formulation[111] which introduce only a few extra parameters.

The orientation of a rigid body about its center of mass can be specified by three Eulerian angles (ϕ, θ, ψ).[113] Because of a "$\frac{1}{\sin\theta}$" term in the equations of motion, this can cause a

singularity when θ approaches 0 or π, which in general makes the simulation unstable[88, 135]. Evans solved this singularity by using a quaternion algorithm[135]. In terms of quaternions, the rotation matrix relates the body-fixed frames to the space-fixed frames as[88, 113, 135]

$$\mathbf{e}^b = \mathbf{A}(\mathbf{q})\cdot\mathbf{e}^s \tag{2.52}$$

where $\mathbf{e}^b$ and $\mathbf{e}^s$ are vectors in the body-fixed and space-fixed frames, respectively. $\mathbf{q}$ is the quaternion, and $\mathbf{q} = (q_0, q_1, q_2, q_3)^T$, "$T$" represents "transpose", and $q_0^2 + q_1^2 + q_2^2 + q_3^2 = 1$. $\mathbf{q}$ is related to Euler by[88]

$$\begin{aligned} q_0 &= \cos\frac{\theta}{2}\cos\frac{\phi+\psi}{2} \\ q_1 &= \sin\frac{\theta}{2}\cos\frac{\phi-\psi}{2} \\ q_2 &= \sin\frac{\theta}{2}\sin\frac{\phi-\psi}{2} \\ q_3 &= \cos\frac{\theta}{2}\sin\frac{\phi+\psi}{2} \end{aligned} \tag{2.53}$$

and the rotation matrix, in terms of quaterionions, is defined as

$$\mathbf{A}(\mathbf{q}) = \begin{pmatrix} -q_2^2 - q_3^2 + q_0^2 + q_1^2 & 2(q_1q_2 + q_0q_3) & 2(q_1q_3 - q_0q_2 \\ 2(q_1q_2 - q_0q_3) & q_0^2 - q_1^2 - q_2^2 + q_3^2 & 2(q_2q_3 + q_0q_1 \\ 2(q_1q_3 + q_0q_2 & 2(q_0q_3 - q_1q_2 & -q_1^2 - q_2^2 + q_0^2 + q_3^2 \end{pmatrix} \tag{2.54}$$

The equations of motion in terms of quaternions are given by[88, 113, 135]

$$\begin{aligned} \dot{\mathbf{q}} &= \frac{1}{2}\mathbf{S}(\mathbf{q})\omega^{(4)} \\ \dot{\omega}_x^b &= \frac{\tau_x^b}{I_{xx}} + \frac{(I_{yy} - I_{zz})}{I_{xx}}\omega_y^b\omega_z^b \\ \dot{\omega}_y^b &= \frac{\tau_y^b}{I_{yy}} + \frac{(I_{zz} - I_{xx})}{I_{yy}}\omega_z^b\omega_x^b \\ \dot{\omega}_z^b &= \frac{\tau_z^b}{I_{zz}} + \frac{(I_{xx} - I_{yy})}{I_{zz}}\omega_x^b\omega_y^b \end{aligned} \tag{2.55}$$

where I_{xx}, I_{yy}, and I_{zz} are the three principal moments of inertia; τ_x^b, τ_y^b, τ_z^b are the torque in the body-fixed frames; ω_x^b, ω_y^b, and ω_z^b are the body-fixed angular velocities, $\omega^{(4)} = (0, \omega_x^b, \omega_y^b, \omega_z^b)$; and $\mathbf{S}(\mathbf{q})$ is a 4×4 orthogonal matrix,[135] which is defined as

$$\mathbf{S}(\mathbf{q}) = \begin{pmatrix} q_0 & -q_1 & -q_2 & -q_3 \\ q_1 & q_0 & -q_3 & q_2 \\ q_2 & q_3 & q_0 & -q_1 \\ q_3 & -q_2 & q_1 & q_0 \end{pmatrix} \tag{2.56}$$

The conserved energy of a rigid body system in terms of internal coordinates is given by[111, 112, 113, 114]

$$H' = T(\omega) + \Phi(\mathbf{q}) = \frac{1}{2} I_{xx} (\omega_x^b)^2 + \frac{1}{2} I_{yy} (\omega_y^b)^2 + \frac{1}{2} I_{zz} (\omega_z^b)^2 + \Phi(\mathbf{q}) \tag{2.57}$$

where $T(\omega)$ is the rotational kinetic energy, and $\Phi(\mathbf{q})$ is the rotational potential energy in terms of quaternions.

Since H' in eq. (2.57) is not Hamiltonian (see eq. (2.19)), the dynamics does not satisfy the symplectic condition (see eq. (2.22)) [87, 111]. However, by using an extended phase space, Miller *et al.*[111] showed that the generated dynamics does indeed follow the symplectic condition. In the extended phase space, $\omega^{(4)}$ changes to $(\omega_x^0, \omega_x^b, \omega_y^b, \omega_z^b)$, and a principal moment of inertia I_{00} is added which corresponds to ω_x^0. The extended Hamiltonian is then given by[111]

$$H(\mathbf{p}, \mathbf{q}) = \frac{1}{8} \mathbf{p}^T \mathbf{S}(\mathbf{q}) \mathbf{D} \mathbf{S}^T(\mathbf{q}) \mathbf{p} + \Phi(\mathbf{q}) = T(\mathbf{p}, \mathbf{q}) + \Phi(\mathbf{q}) \tag{2.58}$$

where $T(\mathbf{p}, \mathbf{q})$ is the rotational kinetic energy in terms of quaternions $\mathbf{q}$ and conjugate momenta of quaternions, $\mathbf{p}$, is defined by

$$\begin{aligned} \mathbf{p} &= \frac{2}{|q|^4} \mathbf{S}(\mathbf{q}) \mathbf{D}^{-1} \omega^{(4)}, \\ D &= \begin{pmatrix} I_{00}^{-1} & 0 & 0 & 0 \\ 0 & I_{xx}^{-1} & 0 & 0 \\ 0 & 0 & I_{yy}^{-1} & 0 \\ 0 & 0 & 0 & I_{zz}^{-1} \end{pmatrix} \end{aligned} \tag{2.59}$$

The equations of motion in the extended Hamiltonian are[111]

$$\begin{aligned}
\dot{\mathbf{q}} &= \bigtriangledown_{\mathbf{p}} H(\mathbf{p},\mathbf{q}) \\
&= \sum_{k=0}^{3} \frac{1}{4I_k} (\mathbf{p}^T \mathbf{P}_k \mathbf{q}) \mathbf{P}_k \mathbf{q}, \\
\dot{\mathbf{p}} &= -\bigtriangledown_{\mathbf{q}} H(\mathbf{p},\mathbf{q}) \\
&= \mathbf{F}^4 - \sum_{k=0}^{3} \frac{1}{4I_k} (\mathbf{p}^T \mathbf{P}_k \mathbf{q}) \mathbf{P}_k \mathbf{p}
\end{aligned} \tag{2.60}$$

where $(I_0, I_1, I_2, I_3) = (I_{00}, I_{xx}, I_{yy}, I_{zz})$; $\mathbf{F}^{(4)}$ are the quaternion forces

$$\mathbf{F}^{(4)} = 2\mathbf{S}(\mathbf{q})\tau^{(4)}, \quad (\tau^{(4)} = (0, \tau_x^b, \tau_y^b, \tau_z^b)) \tag{2.61}$$

and

$$\begin{aligned}
\mathbf{P}_0\mathbf{p} = \{p_0, p_1, p_2, p_3\}, \quad \mathbf{P}_1\mathbf{p} = \{-p_1, p_0, p_3, -p_2\}, \\
\mathbf{P}_2\mathbf{p} = \{-p_2, -p_3, p_0, p_1\}, \quad \mathbf{P}_3\mathbf{p} = \{-p_3, p_2, -p_1, p_0\}, \\
\mathbf{P}_0\mathbf{q} = \{q_0, q_1, q_2, q_3\}, \quad \mathbf{P}_1\mathbf{q} = \{-q_1, q_0, q_3, -q_2\}, \\
\mathbf{P}_2\mathbf{q} = \{-q_2, -q_3, q_0, q_1\}, \quad \mathbf{P}_3\mathbf{q} = \{-q_3, q_2, -q_1, q_0\}
\end{aligned} \tag{2.62}$$

Since eq. (2.58) satisfies the symplectic condition (eq. (2.22)), a symplectic integrator can then be generated.[111, 136]

Decomposition of eq. (2.60) gives the equations of NO_SQUISH[111] as

$$\begin{aligned}
H(\mathbf{p},\mathbf{q}) &= \sum_{k=0}^{3} h_k(\mathbf{p},\mathbf{q}) + \Phi(\mathbf{q}), \\
h_k(\mathbf{p},\mathbf{q}) &= \frac{1}{8I_k} [\mathbf{p}^T \mathbf{P}_k q]^2, \quad k = 0, \cdots, 3
\end{aligned} \tag{2.63}$$

Applying the Liouville operator for the equations of motion gives[111]

$$i\hat{L}_k = \bigtriangledown_{\mathbf{p}} h_k(\mathbf{p},\mathbf{q}) \cdot \bigtriangledown_{\mathbf{q}} - \bigtriangledown_{\mathbf{q}} h_k(\mathbf{p},\mathbf{q}) \cdot \bigtriangledown_{\mathbf{p}}, \quad k = 0, \cdots, 4 \tag{2.64}$$

where $h_k(\mathbf{p},\mathbf{q})(k = 0, \cdots, 3)$ is given in eq. (2.63), and $h_4(\mathbf{p},\mathbf{q})$ is equal to $\Phi((q))$.

A Trotter expansion of the Liouville operator gives[111]

$$\begin{aligned}\exp(i\hat{L}\Delta t) &= \exp[i\hat{L}_4(\Delta t/2)]\{\exp[i\hat{L}_3(\delta t/2)]\exp[i\hat{L}_2(\delta t/2)]\exp(i\hat{L}_1\delta t)\exp[i\hat{L}_2(\delta t/2)] \\ &\quad \times \exp[i\hat{L}_3(\delta t/2)]\}^{m_{rot}} \times \exp[i\hat{L}_4(\Delta t/2)] \end{aligned} \tag{2.65}$$

where $\{\exp[i\hat{L}_3(\delta t/2)]\exp[i\hat{L}_2(\delta t/2)]\exp(i\hat{L}_1\delta t)\exp[i\hat{L}_2(\delta t/2)]\exp[i\hat{L}_3(\delta t/2)]\}^{m_{rot}}$ represents the evolution of the quaternions, $\exp(i\hat{L}_4\Delta t)$ represents the evolution of quaternion momentum; m_{rot} is a rotation integrator parameter for increasing the calculation accuracy and $\delta t = \Delta t/m_{rot}$. Note that if by setting the initial $\omega_0(0) = 0$, then $h_0(\mathbf{p}, \mathbf{q}) = 0$ for all time t, and thus explains the absence of $\exp(i\hat{L}_0\Delta t)$ because $\exp(i\hat{L}_0\Delta t) = 1$.[111]

Applying this propagator to the extended phase space generates time-reversible and symplectic dynamics for rigid body systems[111].

2.7 NO_SQUISH IN NVT AND NPT SIMULATIONS

NO_SQUISH yields a symplectic and time-reversible integrator in the microcanonical ensemble which is Hamiltonian[111]. In non-Hamiltonian systems, however, it loses its symplectic property, even though it retains time-reversibility and preverses phase space volume. Because most useful molecular dynamic simulations are conducted in the canonical ensemble and isothermal-isobaric ensembles, which generate non-Hamiltonian dynamics, the application of NO_SQUISH in these ensembles causes a non-symplectic integrator[111, 112, 113, 114, 115, 116].

Combining NO_SQUISH with Martyna and Tuckerman's method for treating rigid-body in the NVT and NPT ensemble, Kamberaj *et al.*[112] found the combined algorithm showed reversibility and long-term stability, even in non-Hamiltonian systems, even though it is not symplectic.

By following a similar integration scheme as Kamberaj *et al.*[112], NVT and NPT simulations for a bent-core[52, 4] or linear molecule[67] system are conducted in chapters 4-6. In the NVT simulations, the time evolution for a rigid body system can be determined by a Trotter expansion of the propagator operator $\exp(i\hat{L}\Delta t)$ as in eq. (2.66). This combines

the propagator operator in the canonical ensemble (eq. (2.39)) with the propagator operator of NO_SQUISH (eq. (2.65)):

$$\begin{aligned}\exp(i\hat{L}\Delta t) &= \exp[i\hat{L}_{NHC}(\Delta t/2)]\exp[i\hat{L}_4^{rot}(\Delta t/2)]\{\exp[i\hat{L}_3^{rot}(\delta t/2)]\exp[i\hat{L}_2^{rot}(\delta t/2)]\exp(i\hat{L}_1^{rot}\delta t)\\ &\times\exp[i\hat{L}_2^{rot}(\delta t/2)]\exp[i\hat{L}_3^{rot}(\delta t/2)]\}^{m_{rot}}\times\exp[i\hat{L}_p^{trans}(\Delta t/2)]\exp(i\hat{L}_r^{trans}\Delta t)\\ &\times\exp[i\hat{L}_4^{rot}(\Delta t/2)]\exp[i\hat{L}_p^{trans}(\Delta t/2)]\exp[i\hat{L}_{NHC}(\Delta t/2)] \qquad (2.66)\end{aligned}$$

Here, the superscript "rot" represents the rotation of the rigid body, and "trans" represents the translation of the rigid body. Note the expression of $\exp(i\hat{L}_{NHC}\Delta t)$ is different from that in eq. (2.39) because the equations of motion in rigid-body systems are different from those in a flexible molecule system, and the correct form can be found in Kamberaj *et al.*'s work.[112]

In a similar manner, the propagator operator in NPT simulations (eq. (2.67)) can be obtained by combining the propagator operator in the NPT ensemble (eq. (2.50)) with the propagator operator of NO_SQUISH (eq. (2.65)):

$$\begin{aligned}\exp(i\hat{L}\Delta t) &= \exp[i\hat{L}_{NHC}(\Delta t/4)]\exp[i\hat{L}_P(\Delta t/2)]\exp[i\hat{L}_{NHC}(\Delta t/4)]\exp[i\hat{L}_4^{rot}(\Delta t/2)]\\ &\times\{\exp[i\hat{L}_3^{rot}(\delta t/2)]\exp[i\hat{L}_2^{rot}(\delta t/2)]\exp(i\hat{L}_1^{rot}\delta t)\\ &\times\exp[i\hat{L}_2^{rot}(\delta t/2)]\exp[i\hat{L}_3^{rot}(\delta t/2)]\}^{m_{rot}}\times\exp[i\hat{L}_p^{trans}(\Delta t/2)]\exp(i\hat{L}_r^{trans}\Delta t)\\ &\times\exp[i\hat{L}_4^{rot}(\Delta t/2)]\exp[i\hat{L}_p^{trans}(\Delta t/2)]\exp[i\hat{L}_{NHC}(\Delta t/4)]\\ &\times\exp[i\hat{L}_P(\Delta t/2)]\exp[i\hat{L}_{NHC}(\Delta t/4)] \qquad (2.67)\end{aligned}$$

Note again that the expression of $\exp(i\hat{L}_{NHC}\Delta t)$ and $\exp(i\hat{L}_P\Delta t)$ are different from the corresponding ones in eq. (2.50) as previously explained, and the correct form can be found in Kamberaj *et al.*'s work.[112]

3.0 THEORETICAL BACKGROUND OF MONTE CARLO PARALLEL TEMPERING SIMULATION AND BASIN-HOPPING MINIMIZATION

3.1 INTRODUCTION

Like molecular dynamics simulations, Monte Carlo simulations can also provide useful information for molecular systems at equilibrium[88, 87], such as structural information calculated from the pairwise correlation distribution functions, phase transitions using temperature (or pressure) annealing, and exploring the local minima of a potential energy surface using parallel tempering[69]. While many aspects are similar, dynamical information cannot be obtained using Monte Carlo simulations[88, 87]. As previously explained since molecular dynamics simulations solve the equations of motion, it is well suited for this task. Unlike molecular dynamics simulations, Monte Carlo simulations only sample configuration space. However, Monte Carlo simulations can perform unphysical trial moves[87], which are not allowed in molecular dynamics simulations but can still be valid in Monte Carlo simulations. For example, Grand Canonical Monte Carlo simulation requires the number of system particles to fluctuate in order to give the correct configurational space distribution in the Grand Canonical ensemble, which is not possible in molecular dynamics simulations as the number of particles need to be constant.[88, 87]

To explore the energy landscape and to determine the energy minima of clusters composed of coarse-grained bent-core or linear molecules, both Monte Carlo parallel tempering simulations[69] and basin-hopping minimization[68] are performed on clusters containing between 2 and 60 molecules. Chiral superstructures formed in molecular dynamics simulations are shown to be minima of the potential energy surface. In this chapter, the theoretical background of the Monte Carlo parallel tempering simulation[69] and basin hopping minimization

scheme are introduced[68].

3.2 INTRODUCTION TO MONTE CARLO SIMULATIONS

The general way information is obtained in Monte Carlo simulations is by calculating its thermodynamics average. This is accomplished theoretically by evaluating the configuration average:

$$\langle A \rangle = \frac{\int d\mathbf{r}^N \exp[-\beta U(\mathbf{r}^N)] A(\mathbf{r}^N)}{\int d\mathbf{r}^N \exp[-\beta U(\mathbf{r}^N)]} \tag{3.1}$$

Note there is no momentum term in eq. (3.1) because only the configurational space is included. Pratically, the solution of eq. (3.1) can be accomplished by a discrete average over the configurations generated in the Markov chain, that is, $\langle A \rangle = \frac{1}{N} \sum_{i=1}^{N} A_i$.

The probability of finding a system in a configuration $\mathbf{r}^N$, $\overline{N}(\mathbf{r}^N)$, can be expressed as

$$\begin{aligned} \overline{N}(\mathbf{r}^N) &= \frac{\exp[-\beta U(\mathbf{r}^N)]}{\int d\mathbf{r}^N \exp[-\beta U(\mathbf{r}^N)]} \\ &= \frac{\exp[-\beta U(\mathbf{r}^N)]}{Q} \end{aligned} \tag{3.2}$$

where Q is the partition function.

During a Monte Carlo simulation move, the old configuration is defined as o, and the new configuration as n. Unlike molecular dynamics simulation, in which the new configuration is completely determined by the last configuration by following the equations of motion[88, 87], the trial move in Monte Carlo is done by a displacement of the old configuration, which may be accepted or rejected[88, 87]. If the transition probability matrix from o to n is defined as $\pi(o \to n)$, after the system reaches equilibrium, the detailed balance condition needs to be satisfied[88, 87]. This condition states that the average number of accepted moves from o to n is the same as the average number of accepted moves from n to o. This can be mathematically expressed as[88, 87]

$$\overline{N}(o)\pi(o \to n) = \overline{N}(n)\pi(n \to o) \tag{3.3}$$

The transition probability matrix is a product of two probabilities, the probability of attempting a trial from o to n, defined as $\alpha(o \to n)$, and the probability of accepting a trial move from o to n, $acc(o \to n)$, so is defined as[88, 87]

$$\pi(o \to n) = \alpha(o \to n) \times acc(o \to n) \tag{3.4}$$

Substituting eq. (3.4) into (3.3) gives

$$\overline{N}(o)\alpha(o \to n) \times acc(o \to n) = \overline{N}(n)\alpha(n \to o) \times acc(n \to o) \tag{3.5}$$

If the probability of attempting a move from o to n is the same as the reverse, then eq. (3.5) can be simplified as[88, 87]

$$\begin{aligned} \overline{N}(o) \times acc(o \to n) &= \overline{N}(n) \times acc(n \to o), \\ \frac{acc(o \to n)}{acc(n \to o)} &= \frac{\overline{N}(n)}{\overline{N}(o)} = \exp\{-\beta[U(n) - U(o)]\} \end{aligned} \tag{3.6}$$

where eq. (3.2) is used in derivation.

Using Metropolis *et al.*'s[137] scheme, the acceptance ratio probability $acc(o \to n)$ can be defined by

$$acc(o \to n) = \min\{1, \exp[-\beta(U(n) - U(o))]\} \tag{3.7}$$

A typical Monte Carlo simulation in the canonical ensemble proceeds as follows: first, choose a force field; second, generate an initial configuration; third, conduct Monte Carlo moves to sample configuration space according to eq. (3.7) unitl equilibrium is reached; finally, conduct Monte Carlo moves according to eq. (3.7) and collect statistics for properties of interest of equilibrium.

3.3 MONTE CARLO PARALLEL TEMPERING SIMULATIONS

In a Monte Carlo parallel tempering simulation[69], one conducts M simulations (each one is known as a replica) of the system of interest, where each of the M systems typically has a different temperature. An extended ensemble is defined as a combination of all M subsystems. Since the subsystems do not interact energetically, the partition function of this extended system is give by[69, 87]

$$\begin{aligned} Q &= \prod_{i=1}^{M} Q_{NVT_i} \\ &= \prod_{i=1}^{M} \frac{q_i}{N!} \int d\mathbf{r}_i^N \exp[-\beta_i U(\mathbf{r}_i^N)] \end{aligned} \tag{3.8}$$

where $q_i = \prod_{j=1}^{N} (2\pi m_j k_B T_i)^{3/2}$ comes from the integration out of the momenta, $\mathbf{p}_i$; m_j is the mass of atom j, $\mathbf{r}_i^N$ specifies the positions of the N particles in system i, β_i is the reciprocal temperature.

Monte Carlo parallel tempering simulations are effective at overcoming energy barriers in simulations. This is achieved by attempting configuration swaps between replicas at different temperatures[69, 87]. It should be noted that parallel tempering technique can also be applied to molecular dynamics simulations. However, because the dynamic information for each replicas will lose during the configuration swaps, the gain in molecular dynamics parallel tempering is negligible.[69]

In Monte Carlo parallel tempering simulations, assuming the acceptance rule of a swap between replicas i and j follows the condition of detialed balance, and can be expressed as[87]

$$\begin{aligned} &\overline{N}(\mathbf{r}_i^N, \beta_i)\overline{N}(\mathbf{r}_j^N, \beta_j) \times \alpha[(\mathbf{r}_i^N, \beta_i), (\mathbf{r}_j^N, \beta_j) \to (\mathbf{r}_j^N, \beta_i), (\mathbf{r}_i^N, \beta_j)] \\ &\qquad \times acc[(\mathbf{r}_i^N, \beta_i), (\mathbf{r}_j^N, \beta_j) \to (\mathbf{r}_j^N, \beta_i), (\mathbf{r}_i^N, \beta_j)] \quad = \\ &\overline{N}(\mathbf{r}_i^N, \beta_j)\overline{N}(\mathbf{r}_j^N, \beta_i) \times \alpha[(\mathbf{r}_i^N, \beta_j), (\mathbf{r}_j^N, \beta_i) \to (\mathbf{r}_i^N, \beta_i), (\mathbf{r}_j^N, \beta_j)] \\ &\qquad \times acc[(\mathbf{r}_i^N, \beta_j), (\mathbf{r}_j^N, \beta_i) \to (\mathbf{r}_i^N, \beta_i), (\mathbf{r}_j^N, \beta_j)] \end{aligned} \tag{3.9}$$

where $\overline{N}(\mathbf{r}_i^N, \beta_i)$ is the probability density at position $\mathbf{r}_i^N$ with the reciprocal temperature β_i.

If the probability, α, of attempting a swap move is equal for all conditions, then based on eqs. (3.6) and (3.9), the acceptance rule for exchanges between replicas i and j is expressed as

$$\begin{aligned}\frac{acc[(\mathbf{r}_i^N,\beta_i),(\mathbf{r}_j^N,\beta_j)\rightarrow(\mathbf{r}_j^N,\beta_i),(\mathbf{r}_i^N,\beta_j)]}{acc[(\mathbf{r}_i^N,\beta_j),(\mathbf{r}_j^N,\beta_i)\rightarrow(\mathbf{r}_i^N,\beta_i),(\mathbf{r}_j^N,\beta_j)]} &= \frac{\exp[-\beta_i U(\mathbf{r}_j^N)-\beta_j U(\mathbf{r}_i^N)]}{\exp[-\beta_i U(\mathbf{r}_i^N)-\beta_j U(\mathbf{r}_j^N)]} \\ &= \exp\{(\beta_i-\beta_j)[U(\mathbf{r}_i^N)-U(\mathbf{r}_j^N)]\}\end{aligned} \tag{3.10}$$

Following Metropolis *et al.*'s[137] scheme, the acceptance probability is defined by

$$A = \min\{1,\exp[(\beta_i-\beta_j)(U(\mathbf{r}_i^N)-U(\mathbf{r}_j^N))]\} \tag{3.11}$$

Swaps are normally attempted between systems with adjacent temperatures. Because the swap does not disturb the Boltzmann distribution of a particular ensemble, each individual ensemble can be sampled just like a normal Monte Carlo simulation.[69, 87]

In Monte Carlo parallel tempering simulations, all simulations are performed inside a spherical enclosure. The use of a spherical enclosure significantly improves the efficiency of the parallel tempering scheme by keeping particles relatively close together, whilst being large enough not to influence the clusters formed in the simulation. Monte Carlo moves are performed by changing the centre of mass position and orientation of randomly selected molecules. Choosing temperatures is also very important in parallel tempering. In our parallel tempering simulations, the lowest temperature is fixed and the temperatures of other replicas are allowed to adaptively vary until the swapping ratios are optimized[138]. The choice of the lowest temperature is a balance between being close enough to zero temperature to provide good low-energy candidates for energy minimization and having a broad enough energy distribution to allow for parallel tempering swaps between adjacent replicas. The total number of replicas used ensures that the high-temperature replica is isotropic. Low-energy configurations from the simulations are stored and energy minimized.

3.4 BASIN-HOPPING MINIMIZATION

The Basin-hopping minimization method[68] has been successfully employed in the global optimization of numerous systems, for example in the study of low energy LJ clusters[139] and protein conformations[140]. Basin-hopping minimization combines Monte Carlo simulation with minimization, as shown in Fig. 3.

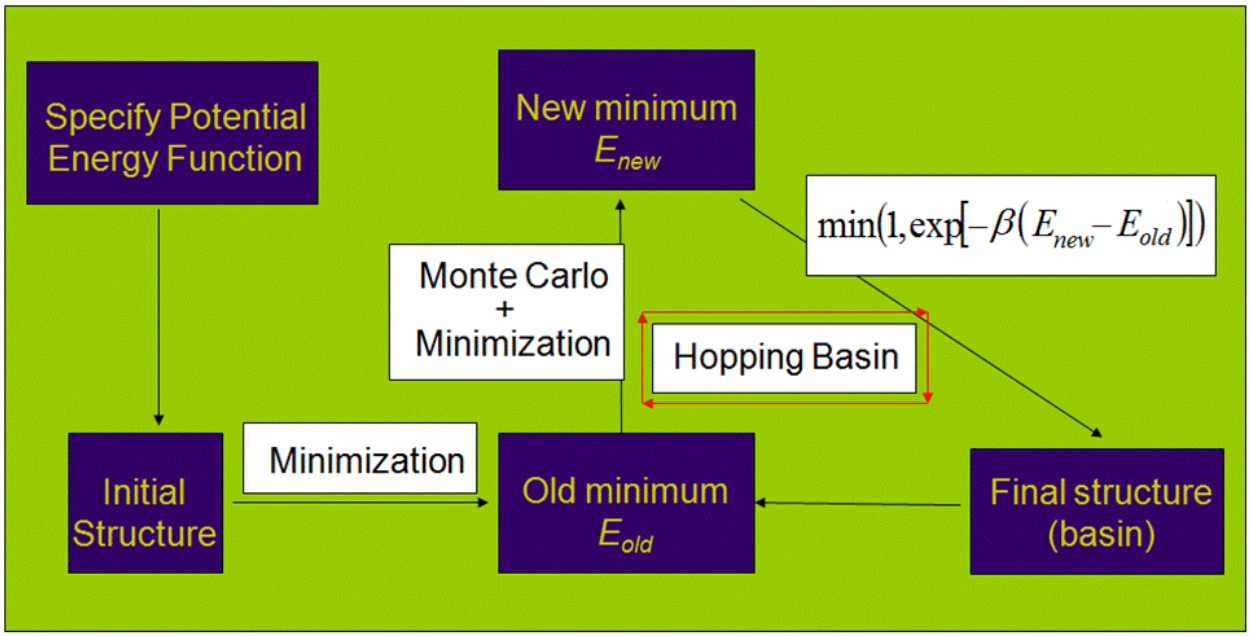

Figure 3: Flowchat of a typical basin-hopping scheme.

In the basin-hopping minimization scheme, one proceeds along the following steps. First, choose a force field; second generate an initial configuration; third, conduct minimization on the initial configuration, store the minimized configuration and define its energy as E_{old}; fourth, perform a normal Monte Carlo simulation on the minimized geometry, then conduct a minimization on the final structure of the simulation, storing the new minimized configuration, and defining its corresponding energy as E_{new}; finally, determine to accept or reject the new minimum using the Metropolis criterion, $\min(1, \exp[-\beta(E_{new} - E_{old})])$. After the cycle, the final structure (basin) will be used as the initial configuration for the next cycle.

Then start the above procedure again until the global minimum is found.

Because the basin-hopping method explores the potential energy surface using local minima (basins), it is much more effective in finding the global minimum of the studied systems.[141, 142, 68] However, for large clusters containing more than 100 atoms, the computational effort of basin-hopping minimization method is prohibitive[139]. In that case, Monte Carlo parallel tempering simulation can be used to solve this size problem, and still be able to find the global minimum.[69]

In chapters 4-6, Monte Carlo parallel tempering simulations are preformed on clusters containing 50 or 60 molecules, and basin-hoping minimizations on clusters containing between 2 and 15 molecules. The simulation results show that the chiral superstructures are minima of the potential energy surface for the coarse-grained rigid bent-core or linear molecules.

4.0 SELF-ASSEMBLED CHIRAL SUPERSTRUCTURES COMPOSED OF RIGID ACHIRAL MOLECULES AND MOLECULAR SCALE CHIRAL INDUCTION BY DOPANTS

This part is partially reproduced from our following work[52]:

Yan, F.; Hixson, C. A.; Earl, D. J. Phys. Rev. Lett. 2008, 101, 157801.

4.1 INTRODUCTION

In this work the phase behavior of a coarse-grained bent-core model system is explored using computer simulations, where the constituent molecules in the simulations are rigid and achiral. A simplified coarse-grained model system has been chosen in order to determine the essential physics required to observe the chiral phenomena of interest here. A phase diagram is constructed by characterizing the structures observed in molecular dynamics simulations at a range of temperatures and volume fractions. Two major results are presented. First, chiral superstructures can self-assemble from the rigid achiral molecules employed here, although on the scale of the whole system, equal numbers of left- and right-handed structures are observed. To understand the thermodynamic basis for the stability of these structures, Monte Carlo parallel tempering simulations and energy minimization calculations are performed on small clusters of these molecules. Second, control of the supramolecular chirality is demonstrated by the addition of low concentrations of chiral dopants. The chiral dopants are found to induce a consistent twist sense over the entire phase, this result represents the first molecular scale simulation of this effect.

4.2 COMPUTATIONAL DETAILS

The details of the model molecule are as follows (Fig. 4a): each rigid molecule is composed of N beads, each of mass m.

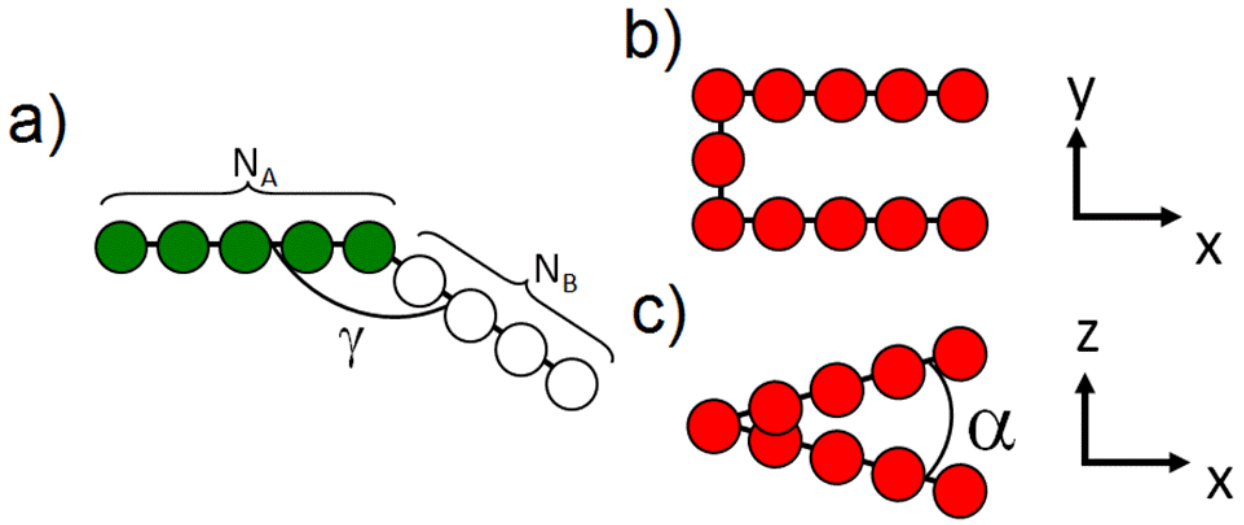

Figure 4: Two model molecules were employed in this work. (a) The bent-core model, composed of LJ [shaded (green)] and WCA (white) particles, with the fixed angle, γ, defining the rigid, achiral shape of the molecule. It was found that the twist direction of the structures formed by the bent-core molecules could be controlled by adding chiral dopants, composed of LJ [dark shaded (red)] particles. The chiral dopant molecule is shown in (b) the xy plane and (c) the xz plane. The angle, α, defines the twist sense of the dopant molecule.

A subset containing N_A beads (green) interacts using an intermolecular Lennard-Jones (LJ) potential. The LJ potential uses an truncated and shifted 12-6 Lennard-Jones (LJ) potential, and is expressed as

$$U_{LJ}(r) = \begin{cases} 4\varepsilon[(\frac{\sigma}{r})^{12} - (\frac{\sigma}{r})^{6}] - 4\varepsilon[(\frac{\sigma}{r_c})^{12} - (\frac{\sigma}{r_c})^{6}] & r \leq r_c, \\ 0 & r > r_c \end{cases} \tag{4.1}$$

where ε is the depth of the potential well, σ is the distance at which the interparticle potential is zero, r is the distance between particles, and r_c is the cutoff distance, $r_c = 2.5\sigma$. The

shifted potential at the distance r_c is implemented to avoid the discontinuity caused by the truncation of the potential at r_c.[88]

The remaining $N_B = N - N_A$ beads (white) interact using an intermolecular Weeks-Chandler-Andersen (WCA) potential[143]. Intermolecular A-B interactions use a WCA potential. The WCA potential is the 12-6 LJ potential truncated at the minimum potential and shifted vertically by ε, which gives a purely repulsive potential[143]:

$$U_{WCA}(r) = \begin{cases} 4\varepsilon[(\frac{\sigma}{r})^{12} - (\frac{\sigma}{r})^{6}] + \varepsilon & r \leq r_c^*, \\ 0 & r > r_c^* \end{cases} \tag{4.2}$$

where $r_c^* = 2^{\frac{1}{6}}\sigma$.

Each subset of beads is arranged in a linear segment, with each particle separated by length σ. The two linear segments are joined together into a single rigid molecule with an angle of γ between the two segments (see Fig. 4a).

In this work, a system of $M = 4800$ molecules are chosen, with $N_A = 5, N_B = 4$ and $\gamma = 150°$. The molecule may be interpreted as a rigid-shape amphiphile in a solvent that is good for the WCA section and poor for the LJ section. Simulation details and results are presented in terms of reduced units[88]:

$$T^* = \frac{k_B T}{\varepsilon}; \quad P^* = \frac{P\sigma^3}{\varepsilon}; \quad t^* = t(\frac{\varepsilon}{m\sigma^2})^{\frac{1}{2}} \tag{4.3}$$

where T^*, P^*, and t^* are the reduced temperature, pressure and time, respectively. And the energy is in units of ε.

All molecular dynamics simulations are performed using a time step of $5\times10^{-3}t^*$. The equations of motion are integrated by using the NO_SQUISH integrator of Miller *et al.*[111], and an operator splitting similar to that proposed by Kamberaj *et al.*[112] is used for simulations in the canonical (NVT) and isothermal-isobaric (NPT) ensembles (see chapter 2). The system is prepared at a variety of densities, and heated until the isotropic phase was observed in the NVT ensemble. The system is then sequentially cooled 0.25 reduced temperature units over 1.5×10^5 steps followed by an equilibration period of 3×10^5 steps. Near phase transitions this process is slowed and manually observed. Simulations are also performed in the isothermal-isobaric (NPT) ensemble, where systems are prepared in the isotropic phase

at a variety of pressures and then slowly annealed following the same procedure as in the NVT simulations. The phases reported in this work are observed in both the NVT and the NPT simulations, and a phase diagram for the bent-core system is shown in Fig. 5. A phase diagram is constructed in a manner similar to Horsch *et al.*[25, 26].

4.3 RESULTS AND DISCUSSION

All the phases observed are shown in Fig. 5.

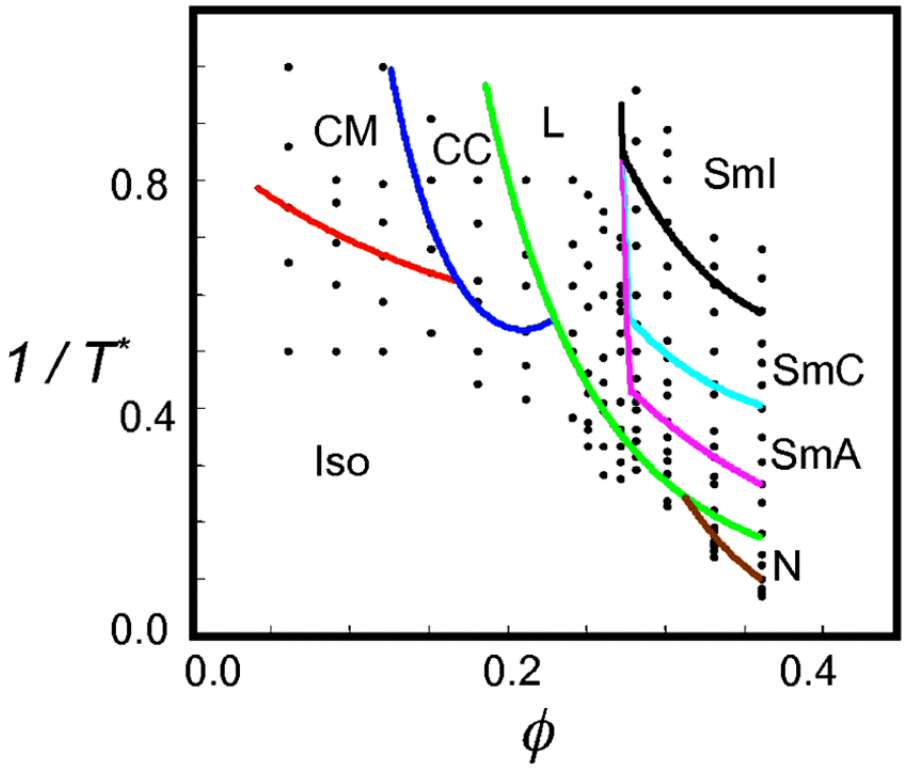

Figure 5: Phase diagram of the bent-core system. T^* is the reduced temperature and $\phi = MN\pi\sigma^3/V_{\text{box}}$ is the volume fraction. At volume fractions greater than 0.21, the system visits the nematic (N), lamellar (L), smectic A (SmA), smectic C (SmC), and smectic I (SmI) phases. At lower densities, chiral features develop, including chiral micelle (CM) and chiral column (CC) phases. The isotropic (Iso) phase occurs at high temperatures for all volume fractions.

At high volume fractions, the system visits a range of traditional liquid crystalline phases. A lamellar phase (L) exists at volume fractions beyond $\phi = 0.21$. This phase is characterized by layers formed by the Lennard-Jones portion of the model, separated by disordered layers of the purely repulsive WCA portion. Regions of smectic ordering are formed at volume fractions greater than 0.27 including smectic A, smectic C, and smectic I phases. The

smectic I phase possesses local hexagonal ordering along with an inlayer tilt towards the hexagonal apex. The presence of attractive and replusive regions in the model here naturally favors zigzag configurations of particles at high density. Thus, the origin of the in-layer tilt is believed to arise for steric reasons, as occurs in systems composed of purely repulsive zigzag shaped particles[144]. The tilt angle varies with temperature and pressure, and has a maximum of 27.0°. The large system size employed here ensures that at least three discrete smectic layers form in the periodic simulation box. A nematic phase (N) is also observed to form at higher temperatures, for volume fractions between $\phi = 0.33$ and $\phi = 0.36$.

At volume fractions below $\phi = 0.15$ on the phase diagram, a phase composed of chiral micelles (CM) forms. A snapshot of this phase is shown in Fig. 6(a). The micelles are stabilized due to the attractive LJ sections' tendency to adhere to each other, which is counterbalanced by the space-filling, purely repulsive nature of the WCA portions. This balance leads to a racemic polydisperse size distribution of micelles. The noteworthy feature of this result is found in the chiral nature of the micelles. There is a discernible twist in each, shown in Figs. 6(f) and 6(g), that is also observed in parallel tempering simulations and energy minimizations of small clusters of the model system.

To determine the thermodynamic basis for the stability of the chiral micelles, the potential energy surfaces of clusters of 2, 4, 8, and 60 molecules were explored by using energy minimization techniques and Monte Carlo parallel tempering simulations (see chapter 3). For clusters of 2, 4, and 8 molecules, minimizations are performed using the basin hopping technique[68] with the Polak-Ribiere conjugate gradient method as the underlying minimization scheme[145]. Monte Carlo parallel tempering simulations[69] were performed for systems containing 60 molecules, a typical size for a chiral micelle in simulations, inside a spherical enclosure of radius 25σ. These simulations used Monte Carlo moves that changed the center of mass position and orientation of randomly selected molecules. Eighteen parallel tempering replicas were used, all at a low temperature of $T^* = 0.6$. The temperatures of other replicas were allowed to adaptively vary until the swapping ratios were optimized[138]. Low energy configurations from these simulations were stored and energy minimized. The minimizations indicate that the discrete nature of the interactions in the model cause twisting as a means to minimize the potential energy, as demonstrated by the staggered alignment of molecules

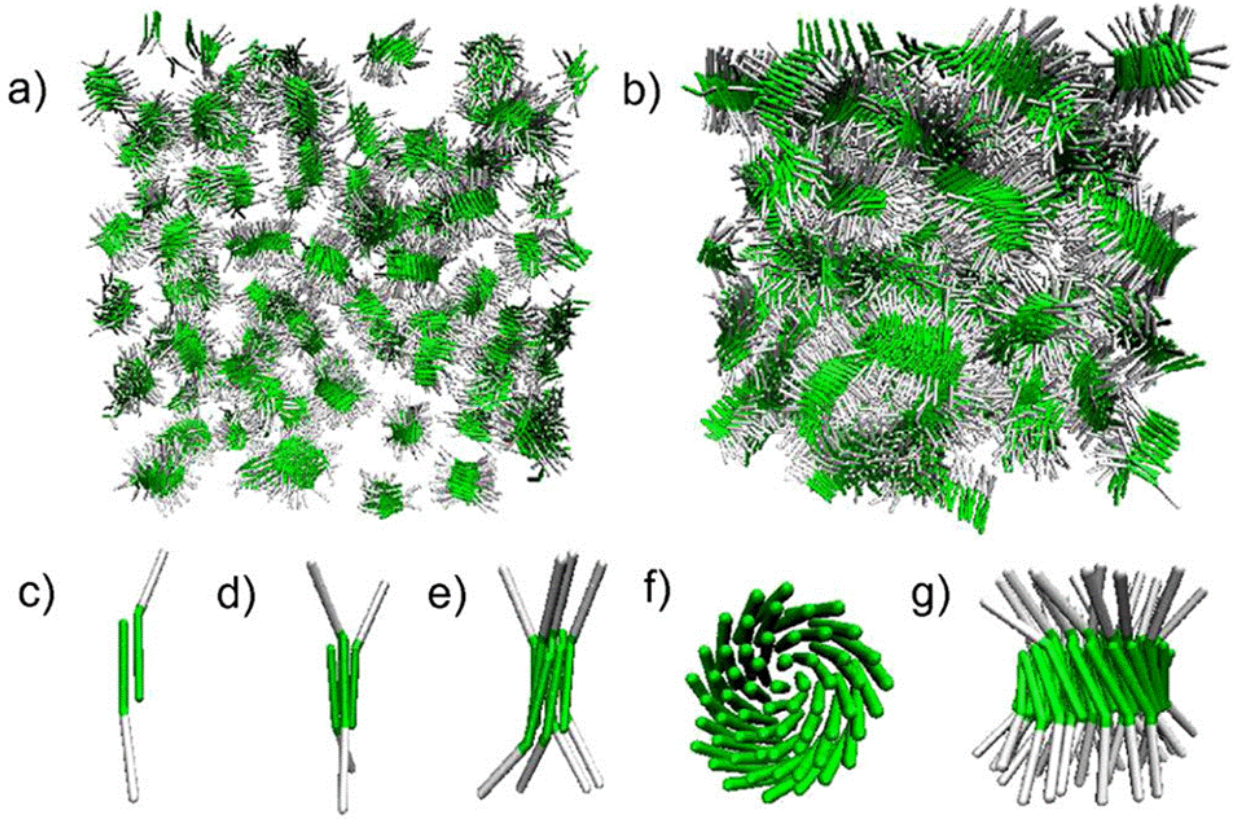

Figure 6: (a) Chiral micelle snapshot. (b) Chiral column snapshot. Energy minimized structures of (c) two, (d) four, and (e) eight molecule clusters of the model system. Minimization of the energy requires maximum overlap between attractive sites, which ultimately manifests as a structural twist. Parallel tempering simulations reproduce the observed twisted micelle shape which is shown (f) from a top down view with the WCA sections removed and (g) from the side.

shown in Figs. 6(c)-6(g). This corresponds to an off-center alignment in the two molecule system, a staggered square arrangement in the four molecule system, and the beginnings of a twisted barrel in the eight molecule system. The parallel tempering simulations found twisted barrel shaped structures with both possible twist directions with nearly identical energies, which is consistent with the observed racemic mixture in the CM phase. Untwisted micelles were only observed in higher temperature replicas and had unfavorable energies compared to the twisted structures. In simulations of flexible polymer-tethered nanorods, Horsch *et*

al.[28, 26] also observed ordered micelle phases. In their laterally tethered system[28], the micelles formed by stacking into a staircase shape, which lacked twisting. In their end-tethered system[26], twisting barrel shapes formed. Because of the similarity of the rigid LJ portion of the model molecule here to those in their studies, the thermodynamic argument explaining the stability of the twisted superstructures is expected to be the same in both cases.

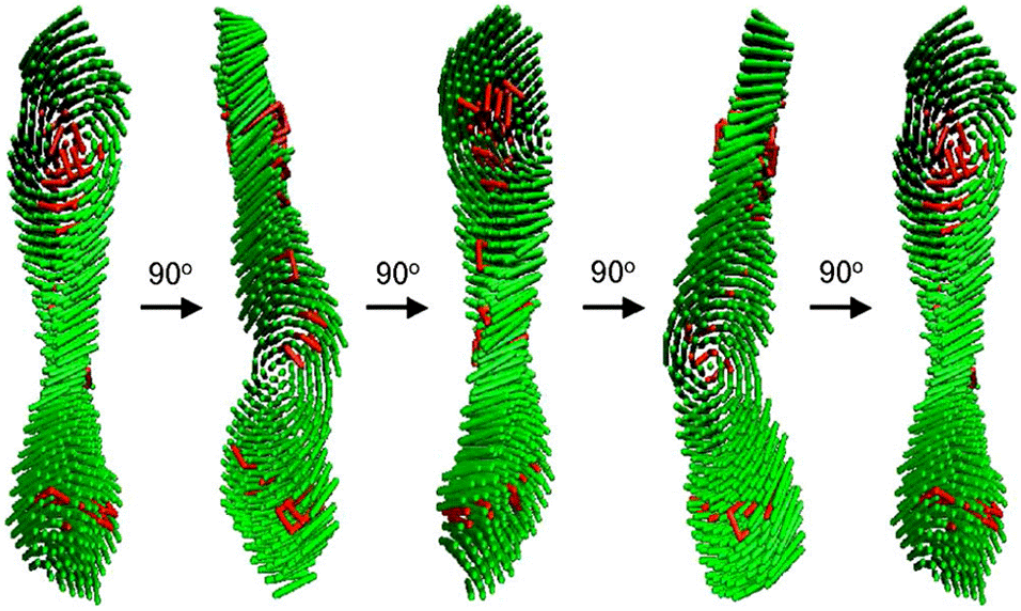

Figure 7: Rotated views of a single chiral column structure with dopant molecules [shown in dark shade (red)] incorporated. The WCA particles in the bent-core molecules have been removed to show the underlying structure of the column. As the dopants strongly influence the twist of the individual micelles into which they incorporate, the uniformity of the twist direction can be described as a packing effect.

A second chiral phase is noted in Fig. 5. This phase, described as a chiral column phase (CC), is located between $\phi = 0.12$ and 0.21 and is pictured in Fig. 6(b). A more detailed view of the interior of an individual column can be seen in Fig. 7. In this phase, the structures possess a helical twist about the long axis of each column, which is interrupted if columns with differing handedness merge. Within the columns, a barrel-like chiral twist is evident. Though the nature of the chirality of the isolated micelles has been explored, explaining the

helical twist observed in this phase is more complicated. Certainly, the packing of chiral objects together is likely to form a chiral structure, as would be the case for several micelles merging to form the column. However, the free energy of the double twist structure observed is stabilized by the rotational entropy gained by an off-parallel stacking between all pairs of adjacent molecules, when compared with the achiral layered structures that are found at higher densities, although the twisted barrel-like structures within the columns are stabilized for the same energetic reasons as in the CM phase. It should be noted that a helical twist was observed in the flexible-tether system of Horsch *et al.*[26] that was explained as an entropic effect, and a long ribbon phase was observed for laterally tethered rods[28].

To investigate whether the handedness of the chiral superstructures formed in the CM and CC phases could be controlled, molecular dynamics simulations were conducted at the densities at which these phases are found, where 1%, 2%, and 4% of the molecules in the system were replaced with chiral dopants. A schematic diagram showing the chiral dopant molecule used in the study is shown in Figs. 4(b) and 4(c). An angle of $\alpha = 15^{\circ}$ is used between the two long axes of the dopant, corresponding to a righthand twist sense for chiral dopants when added to nematic phases[146]. It was found that if a dopant molecule was incorporated into an individual micelle barrel then, due to packing effects, the handedness of the barrel's twist matched that of the chiral dopant. This result holds for all cases where a dopant molecule is incorporated into the structure. It was also found that the addition of as little as 4% dopant can cause the entire system to exhibit a uniform handedness. For doped chiral column systems the helical twist along the long axis of a column is completely uninterrupted, and the structure has a continuous double twist motif. Shown in Fig. 7 is an example of a doped column where the underlying twist sense within, and about, the column is right handed.

4.4 CONCLUSION

That chiral structures can be found in a material composed of rigid achiral building blocks is of further interest because it rules out any nucleation mechanism requiring transient chirality[56, 147]. In systems composed of flexible achiral molecules, although the constituent molecules are achiral on average, each molecule can instantaneously adopt a chiral configuration, and one may argue that the clustering of molecules with the same handedness results in the formation of chiral structures (although there would be an overall racemic mixture of chiral structures). In this study, then, no such mechanism is possible as our constituent molecules are fixed in an achiral conformation. Thus, these results may have implications for the underlying physics behind the formation of some of the liquid crystal banana phases[14], for the stability of blue phases when doped with banana molecules[148], and for the design and synthesis of chiral fibers[149] and crystals[56].

5.0 COMPUTER SIMULATIONS OF LINEAR RIGID PARTICLES THAT FORM CHIRAL SUPERSTRUCTURES AND TILTED SMECTIC PHASES

This part is partially reproduced from our following work[67]:

Yan, F.; Hixson, C. A.; Earl, D. J. Soft Matter, 2009, 5, 4477.

5.1 INTRODUCTION

In the previous chapter, the superstructures and phases formed by rigid bent-core molecules composed of Lennard-Jones and soft-repulsive Weeks-Chandler-Andersen beads were studied, and it was found that chiral micelle and column structures spontaneously self-assemble from these molecules.[52] The rigid nature of the molecules excluded any mechanism requiring transient conformational chirality in the assembly of these structures.

In this chapter the phase behaviour of a coarse-grained linear rigid molecule system is studied by using molecular dynamics simulations in the isothermal-isobaric ensemble (NPT). The interactions between molecules in the system are in the form of simple Lennard-Jones (LJ) and soft-repulsive Weeks-Chandler-Andersen (WCA) potentials[143], yet a rich phase behaviour that includes nematic, untilted smectic and tilted smectic phases is observed. In addition, these molecules are observed to self-assemble into chiral structures, and the novel behaviour of this system is demonstrated to be caused by the discrete nature of the interactions in the molecules by using Monte Carlo parallel tempering simulations. By altering the spacing of interaction sites in the molecules, the relative stability of chiral and achiral superstructures can be tuned. Remarkably, linear segments composed of Lennard-

Jones particles are shown to display superstructural chirality for a range of separations between interaction sites. The rest of the chapter is arranged in the following way. In section 5.2, the computational model and the employed methods are discribed; in section 5.3, the simulation results are presented and their implications are discussed; and the conclusion is made in section 5.4.

5.2 COMPUTATIONAL DETAILS

The model system used here consists of a rigid linear molecule shown in Fig. 8a, where each molecule is composed of N beads, each of mass m.

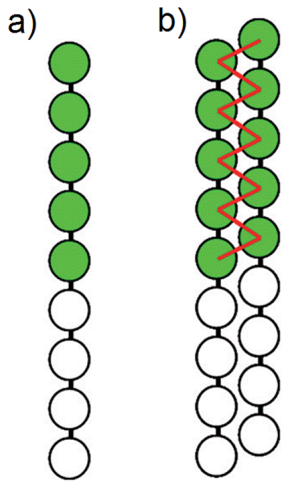

Figure 8: (a) Schematic diagram of the linear rigid molecule that consists of $N_A = 5$ LJ (green) and $N_B = 4$ WCA (white) particles. (b) The minimum energy packing arrangement of two molecules with interaction sites spaced by 1σ showing an off-centre parallel alignment. The lines in the figure represent the optimal energetic distance for two beads to be separated, and is the distance at the minimum of the LJ potential ($2^{1/6}\sigma$). When interaction sites are spaced at larger distances ($> 1.2\sigma$) the molecules align exactly parallel with no off-centre translation.

Of these N beads, a subset of N_A beads interact with each other through an intermolec-

ular, truncated and shifted Lennard-Jones (LJ) potential, and the remaining $N_B = N - N_A$ beads interact with each other through an intermolecular soft-repulsive Weeks-Chandler-Andersen (WCA) potential. Intermolecular A-B interactions are of the WCA form. The σ and ε parameters for the LJ and WCA potentials are chosen to be the same. It should be noted that linear sections of LJ particles were used in the formulation of the commonly utilized Gay-Berne potential[61], and have recently been used to represent nanorods in simulations of polymer-tethered nanorods.[11, 25, 26, 28] Linear sections of WCA sites can be considered as the discrete site version of soft repulsive spherocylinders.[150] By combining these two potential forms into one molecule, these molecules can be considered as amphiphiles in an implicit solvent, where the solvent is good for the WCA section. These potentials in the molecules are used due to their simplified form, that should be realisable in synthetic systems, and which is computationally tractable therefore allowing one to thoroughly map out the superstructures and phases formed by these molecules.

In this work different systems of $M = 4000$, 5000, 6000 and 10 000 molecules are characterized to avoid system size effects, and with periodic boundary conditions were employed in the simulations. Molecules with $N_A = 5$ and $N_B = 4$ are studied, and each adjacent bead in a molecule is separated by a distance of σ unless otherwise stated, allowing for a comparison with the previous work on bent-core molecules in chapter 4.[52] All quantities related to the simulations are expressed in reduced units.[88] A pair potential cutoff of 2.5σ and a time step of 5×10^{-3} t^* are used. The NO_SQUISH integrator of Miller *et al.*[111] is chosen for molecular dynamics of the rigid bodies, and an operator splitting method similar to that proposed by Kamberaj *et al.*[112] is utilized. In the NPT simulations, the system is prepared in an isotropic state at a variety of pressures and then sequentially cooled by 0.25 reduced temperature units over 1.5×10^5 steps followed by an equilibration period of 4.5×10^5 steps. Near phase transitions this process is slowed by increasing the number of equilibration steps, and manually observed to ensure that equilibrium is maintained. Phase transitions are identified by monitoring the energy and volume, and thus the enthalpy, and the order parameter of the system as a function of the temperature during the annealing process. Superstructures and phases are characterized and identified using a variety of techniques including the calculation of radial and pair distribution functions, the calculation of

tilt with respect to the orientational order parameter, and through visualization.

To explore the energy landscape and to determine the energy minima of clusters composed of the rigid linear molecules both basin-hopping[68] and Monte Carlo parallel tempering simulations[69] are performed on clusters containing between 2 and 50 molecules. These simulations are performed inside a spherical enclosure of radius 23.25 σ. The use of a spherical enclosure significantly improves the efficiency of the parallel tempering scheme by keeping molecules in high temperature replicas relatively close to each other. The size of the enclosure is chosen to be a balance between keeping molecules relatively close together, and yet being large enough not to influence the clusters formed in the simulation. In the basin-hopping scheme, a step is performed by carrying out a perturbation of the system followed by energy minimization, and the step is accepted using the Metropolis criterion. This method has been successfully employed in the global optimization of numerous systems, for example in the study of low energy LJ clusters[139] and protein conformations[140]. Monte Carlo moves are performed by changing the centre of mass position and orientation of randomly selected molecules. In the parallel tempering scheme, twenty replicas are used with the lowest temperature set to $T^* = 0.455$. The temperatures of other replicas are allowed to vary until the swapping ratios were optimized.[138] The choice of the lowest temperature is a balance between being close enough to zero temperature to provide good low-energy candidates for energy minimization and having a broad enough energy distribution to allow for parallel tempering swaps between adjacent replicas. The total number of replicas used ensures that the high-temperature replica is isotropic. Low-energy configurations from the simulations are stored and energy minimized.

5.3 RESULTS AND DISCUSSION

Shown in Fig. 9 are the superstructures and phases formed by the linear rigid molecules described in Fig. 8 with a spacing of σ between adjacent interaction sites, at a range of reduced temperatures and pressures.

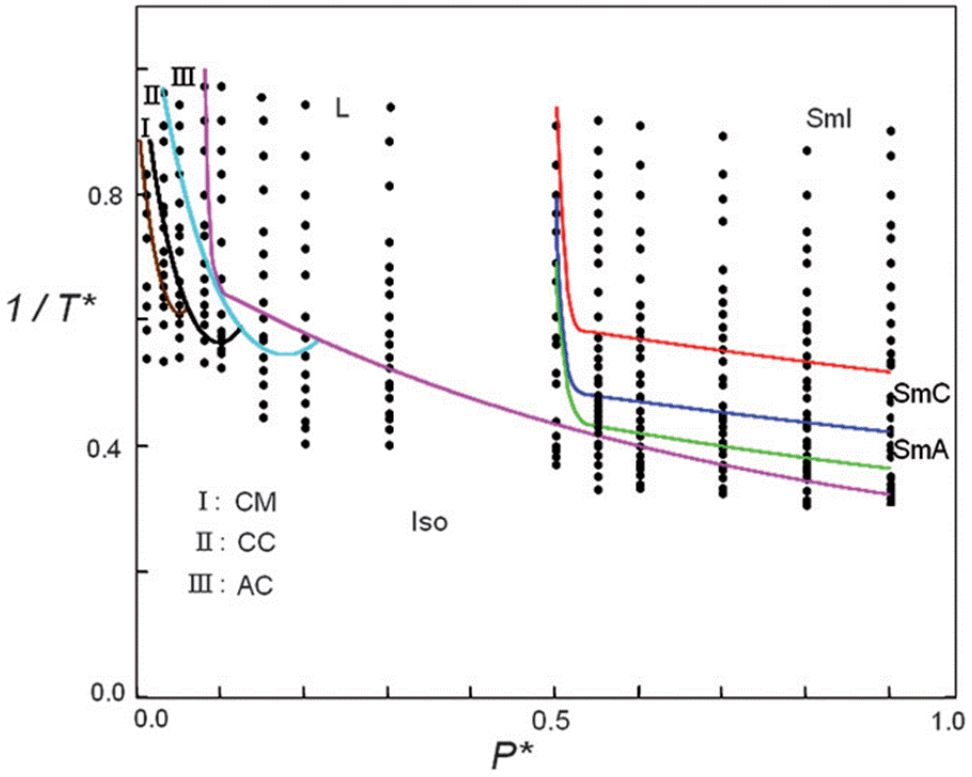

Figure 9: Diagram showing the structures and phases formed by our linear rigid molecules at a range of temperatures and pressures. T^* is the reduced temperature and P^* is the reduced pressure. At low pressures less than $P^* = 0.21$, chiral micelle (CM) and chiral column (CC) structures self-assemble, and at lower temperatures or higher pressures the chiral columns lose their chirality and achiral columns (AC) are formed; at pressures between $P^* = 0.55$ and 0.9, smectic A (SmA), smectic C (SmC) and smectic I (SmI) phases develop; a lamellar phase (L) is also formed at a range of temperatures and pressures.

The system exhibits a rich phase behavior including the isotropic (Iso), chiral micelle (CM), chiral column (CC), achiral column (AC), nematic (N), lamellar (L), smectic A (SmA),

smectic C (SmC) and smectic I (SmI) structures and phases. We now proceed by describing these structures and phases in turn.

At low pressures from $P^* = 0.01$ to $P^* = 0.05$ the molecules self-assemble to form chiral barrel/micelle (CM) structures (Fig. 10a). The chiral micelles are formed such that the attractive Lennard-Jones regions of each molecule stack together to form a central chiral barrel with the soft-repulsive WCA regions of the molecules above and below (Fig. 10d).

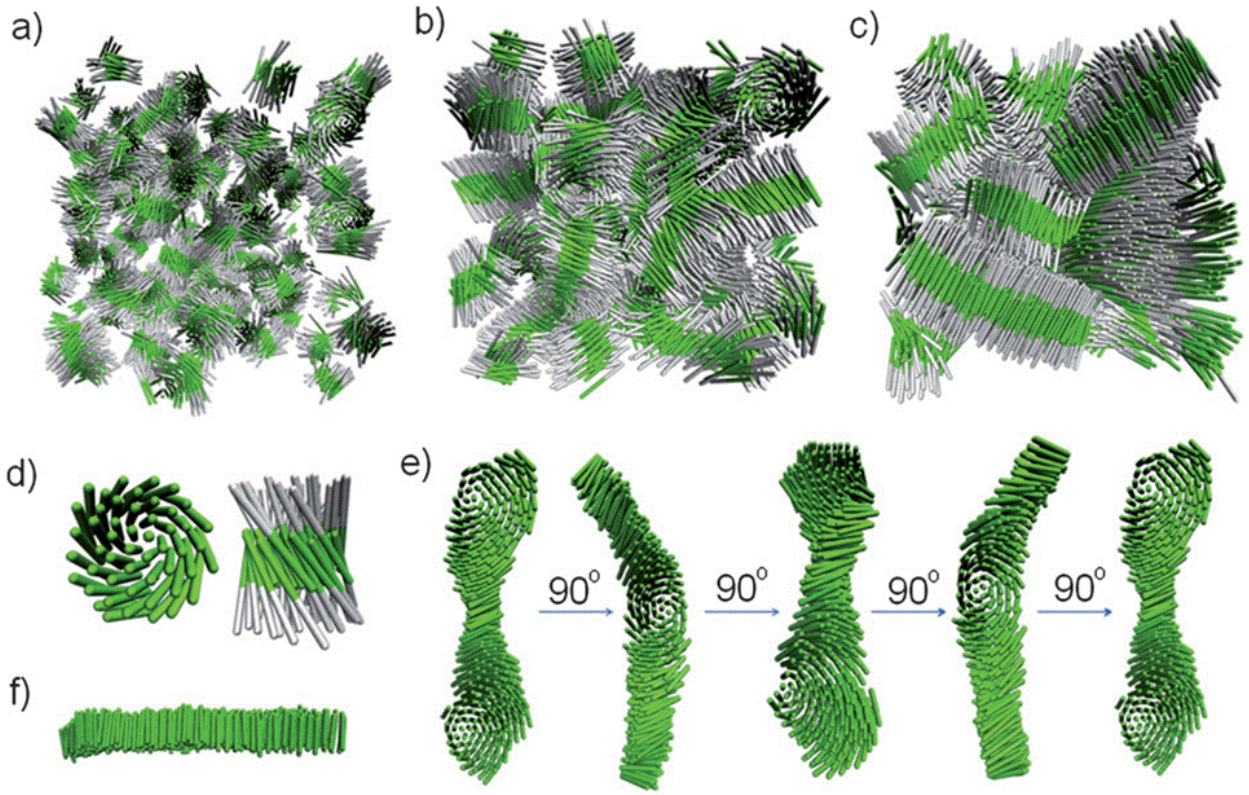

Figure 10: Snapshots taken from our simulations of (a) chiral micelle (CM) structures, (b) chiral column (CC) structures, (c) achiral column (AC) structures. (d) A chiral micelle extracted from the simulation. Left: top view, where WCA particles are removed to guide the viewing; right: side view. (e) Rotated views of a single chiral column structure from the simulation. The column displays a chiral twist both within and about the column. (f) An achiral column from the side view, showing the lack of twist along the column.

A racemic polydisperse size distribution of micelles was found in the simulations. The asphericity parameter[151], A_s, was calculated to obtain information about the micelle shape. For the micelles containing 50 ± 10 molecules, the result was $A_s = 0.06 \pm 0.02$, indicating that the micelles are approximately spherical in shape (Fig. 10d). Energy minimization and parallel tempering simulations of clusters of 50 molecules, which is a typical size of a chiral micelle, demonstrate that chiral micelles are minima of the potential energy surface. The structure of these clusters is described below.

Upon cooling from systems composed of chiral micelles, the molecules assemble into double-twist chiral columns (CC), as shown in Fig. 10b. The double-twist chiral columns have a helical twist about the long-axis of each column, and there is a barrel-like chiral twist within each column, as shown in Fig. 10e. However, the helical twist can be interrupted if columns with different handedness merge. As in a previous study with bent-core molecules, addition of as little as 4% chiral dopant can cause the entire system to exhibit a uniform handednss.[52] The core geometry of these double-twist structures is similar to those proposed in the structure of liquid crystalline blue phases.[152]

Further cooling, or an increase in pressure, results in the formation of achiral columns (AC), shown in Fig. 10c. These structures were not previously observed for bent-core molecules[52]. It is posited that the rotational entropy about the long-axis of the bent-core molecules in chiral column structures stabilizes the chiral structures relative to the achiral column structures observed here for linear molecules. This concept is most easily understood by considering a pair of molecules arranged in a side-by-side parallel configuration as opposed to a slightly off-parallel twisted configuration. In the linear case there is no contribution from the rotational entropy about the long-axis of the molecules (as the molecules are linear). In the case of bent-core molecules, the rotational entropy about the long-axis of the molecules is greater in the off-parallel twisted configuration due to the larger number of overlapping configurations that are not allowed in the parallel configuration, as the molecules are rotated about their long-axis. This argument still holds as the number of molecules in a cluster is increased.

At very high pressures $P^* \geq 3.9$, not shown on Fig. 9, a nematic (N) phase is observed and shown in Fig. 11a, between the isotropic and smectic phases.

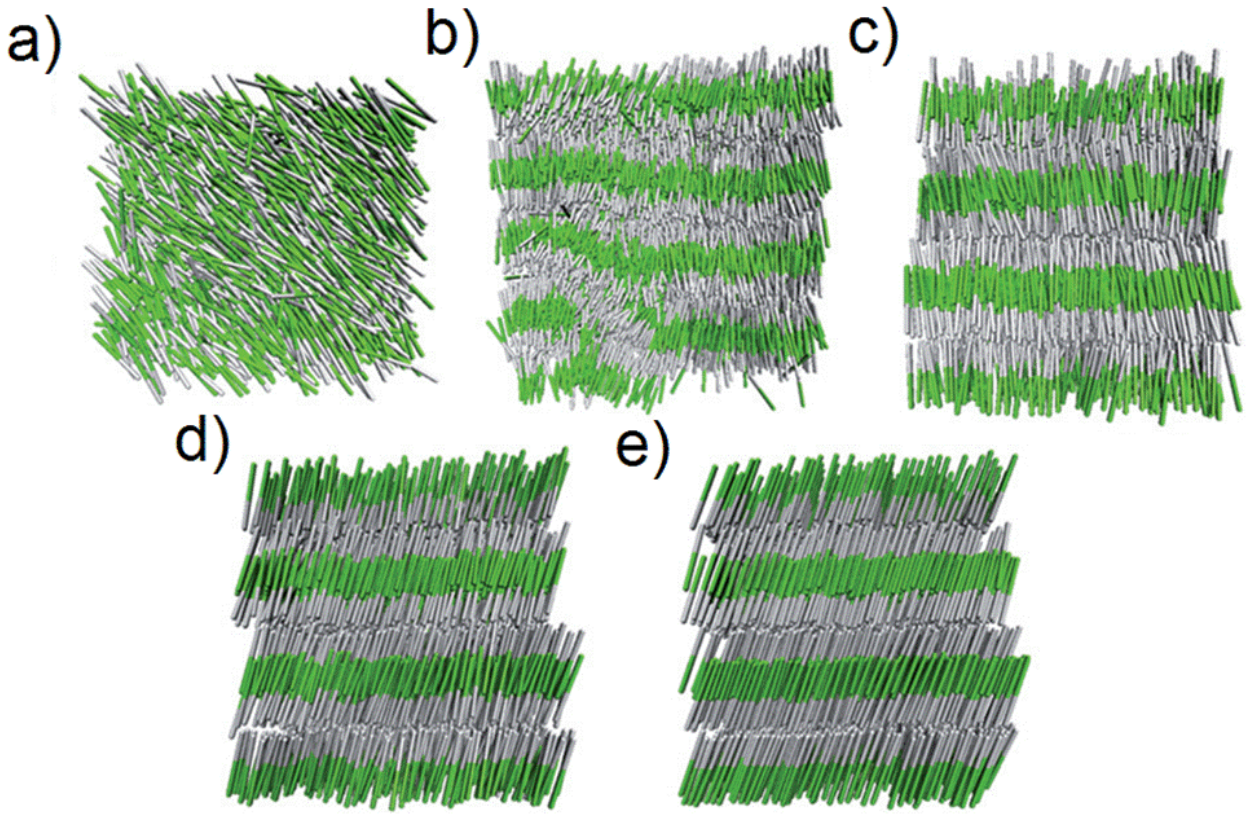

Figure 11: Snapshots taken from our simulations of (a) a nematic phase (N), (b) a lamellar (L) phase, (c) a smectic A phase (SmA), (d) a smectic C phase (SmC), and (e) a smectic I phase (SmI).

The well depth of the side-to-side interaction of two molecules compared to the end-to-end well depth is approximately 9 : 1. This difference is significantly larger than that for traditionally parameterized Gay-Berne particles,[153, 154] and favors layering at higher values of the reduced temperature than one would observe if the LJ section of the molecule were replaced by a traditionally parameterized Gay-Berne particle. Nematic phases are observed for hard spherocylinders with length-to-width ratios greater than 4.5 : 1 and the region of nematic stability increases as the length-to-width ratio increases.[22] Therefore, in the absence of attractive interactions for the present model, a much wider region of nematic

stability would be expected than what is actually observed: as the model molecules have a length to width ratio of 9 : 1, and the attractive interactions in the molecule clearly favour layer formation.

A lamellar phase (L) is observed for pressures beyond $P^* = 0.08$. This phase is characterized by layers formed by the Lennard-Jones portion of the model, separated by disordered layers of the soft-repulsive WCA portion (see Fig. 11b). At higher pressures between $P^* = 0.55$ and $P^* = 0.9$, the layers become ordered and form smectic phases. Three smectic phases are observed: smectic A (SmA), smectic C (SmC) and smectic I (SmI). The smectic A layers are untilted (see Fig. 11c) and display no long range order within the layer. Decreasing the temperature results in the formation of a smectic C phase with tilted layers and no long-range positional ordering within the layers (see Fig. 11d). A further reduction in the temperature results in the formation of a smectic I phase which, in addition to having a tilted layer structure (see Fig. 11e), is characterized by local hexagonal ordering along with an in-layer tilt towards the hexagonal apex.

In order to characterize the smectic layer structures, the longitudinal distribution function, $g_{\parallel}(r)$ was calculated and is shown in Fig. 12a. There are periodic peaks indicating order along the layer normal. In the smectic A phase, the oscillatory peaks are significant, indicating ordered layer packing. The periodic peaks become both sharper and more intense in the smectic C and smectic I phases. The average separation between the peaks can be used to determine the layer spacing, and are calculated as 13.5σ, 13.0σ, and 12.5σ for the smectic A, smectic C and smectic I phases respectively. To explore the structure within each smectic layer, the in-plane distribution function, $g_{\perp}(r)$, was calculated and is shown in Fig. 12b. In both the smectic A and smectic C phases the structure within the layer is clearly liquid like, and the in-plane distribution function shows no long range structure. In the smectic I phase, there is hexagonal ordering and the in-plane order extends to large distances with a fine structure evident in the long range peaks. The separation distance between the peaks constituting this fine structure is approximately 1.0σ (Fig. 12b), and can be attributed to the hexagonal order within the layer. Because of the hexagonal order and the long range oscillations in the in-plane distribution function, this may be a deformed Crystal J phase, although due to the size of the simulation it is not possible to differentiate between the two.

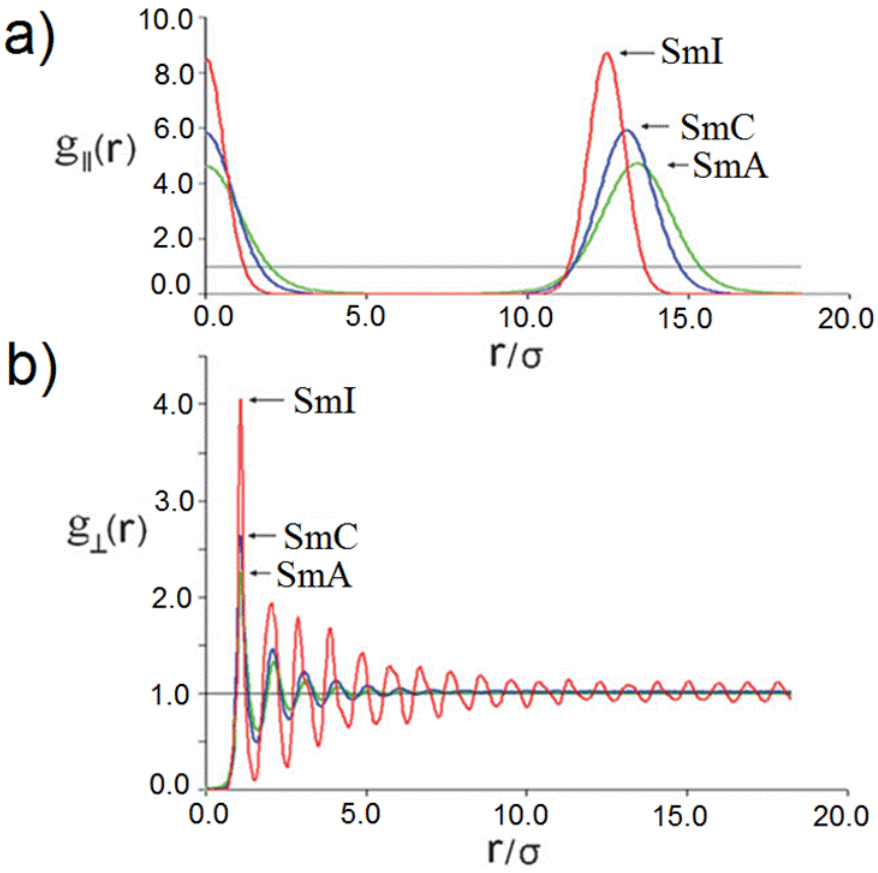

Figure 12: (a) The longitudinal distribution function, $g_{\parallel}(r)$, for a system of $M = 4000$ molecules at $P^* = 0.7$. (b) The in-plane distribution function, $g_{\perp}(r)$, for a system of $M = 4000$ molecules at $P^* = 0.7$. The distribution functions are shown for the smectic A (green), smectic C (blue), and smectic I (red) phases.

The average tilt angle relative to the layer normal was also calculated in each of the smectic phases at $P^* = 0.7$. The tilt angle is temperature dependent and varies from $5° - 15°$ in the smectic C phase to approximately $18°$ in the smectic I phase.

Rigid linear molecules typically only display isotropic, nematic, smectic A and smectic B phases,[22, 150, 155, 156] although a recent study of hard ellipsoids also discovered a simple monoclinic crystal, termed SM2.[157] In addition, Dewar and Camp have studied linear rigid molecules composed entirely of LJ particles.[158] In their system, the molecules assembled into alternating tilted smectic layers with no global tilt. They also describe a tilted smectic B

phase, which may be similar to our smectic I phase. In Xu *et al.*'s work[159], zig-zag shaped molecules composed of WCA beads with a bending angle of 5° form a smectic C phase upon the application of a strong electric field. Comparing the rigid linear model with these two studies, it is evident that the addition of WCA sites to the rigid linear model molecules results in a global tilt of the entire phase, whilst the inclusion of LJ sites stabilizes the tilting of layers without need for the application of an electric field. Other notable computational studies that found tilted smectic structures include that of Withers *et al.*[160] where the tilted smectic J phase was formed from an internally rotated Gay-Berne potential and the site-site interaction resembled that of two zig-zag molecules, systems composed of Gay-Berne particles with the addition of a quadrupole,[161] and in the system of Maiti *et al.*[144] composed of zig-zag shaped repulsive molecules. Also, Horsch *et al.*'s study of polymer-tethered nanorods,[25, 26] where each molecule is composed of a rigid linear section of LJ beads and a flexible WCA section, found a smectic C phase but found no evidence for the formation of the nematic, smectic A or smectic I phases. Their tilted smectic phase appears to us to arise due to the discrete nature of the LJ sites because a similar study undertaken with a smoothly interacting model had no tilt at equivalent state points.[27] By comparison with Horsch *et al.*'s model, the introduction of rigidity in the WCA sections of the molecule clearly stabilizes the nematic and smectic A phases.

To investigate the hypothesis that discrete Lennard-Jones interaction sites are responsible for the novel chiral behaviour that is observed in both this linear system and the bent-core system that was previously reported in chapter 4,[52] linear rigid molecules were systematically studied, as shown in Fig. 8a, with all adjacent interaction sites separated by between 0.5σ and 1.5σ in steps of 0.1σ. Both basin-hopping energy minimization and Monte Carlo parallel tempering simulations were utilized to explore the energy landscape of clusters varying in size from 2 to 50 molecules per cluster. When the interaction sites are spaced by between 0.5σ and 1.2σ, the minimum energy configurations for 2 molecules have energies of -14.8263ε (0.5σ spacing), -12.9288ε (0.6σ spacing), -11.6602ε (0.7σ spacing), -10.8067ε (0.8σ spacing), -10.2331ε (0.9σ spacing), -9.8477ε (1.0σ spacing), -9.5882ε (1.1σ spacing), and -9.4125ε (1.2σ spacing), and the corresponding configurations have a shifted off-centre parallel alignment, as shown in Fig. 8b. In this configuration, 4 of the 5 LJ sites in each

molecule can each be situated at an optimal distance to interact with 2 LJ sites on the other molecule in the cluster. For molecules with interaction sites spaced by greater than 1.2σ the minimum energy configuration for 2 molecules is an unshifted parallel alignment, and each LJ site in each molecule is situated to optimally interact with one LJ site on the other molecule. The minimum energies found for these systems are -9.2926ε (1.3σ spacing), -9.2101ε (1.4σ spacing), and -9.1526ε (1.5σ spacing). For clusters containing 7 molecules, when interaction sites are spaced at small to intermediate distances, between 0.5σ and 1.0σ, the minimum energy structures have a shell of 6 molecules that form around a central molecule. Each molecule in the shell is tilted with respect to the central molecule. These structures are chiral and left- and right-handed clusters have equal energies. The minimum energies found are -186.497ε (0.5σ spacing), -164.507ε (0.6σ spacing), -147.533ε (0.7σ spacing), -134.997ε (0.8σ spacing), -125.627ε (0.9σ spacing), -118.443ε (1.0σ spacing). When interaction sites are spaced by 1.1σ and 1.2σ achiral clusters of 7 molecules have energies comparable with that of the chiral clusters, although achiral clusters are found to be the minimum energy structures with energies of -114.049ε (1.1σ spacing), and -111.174ε (1.2σ spacing). For larger spacings, clusters of 7 molecules are achiral and the minimum energies found are -110.433ε (1.3σ spacing), -111.340ε (1.4σ spacing), -113.242ε (1.5σ spacing). For larger clusters, further shells form and, for intermediate interaction spacings between 0.7σ and 1.1σ, each shell is tilted with respect to the shell inside it in the cluster, and the clusters are chiral indicating that chiral structures are the energy minima of clusters composed of these achiral rigid molecules. These clusters have identical structures to the chiral micelles (CM) described earlier. An example of a cluster composed of 50 molecules for a spacing of 1.0σ between interaction sites is shown in Fig. 13.

The central molecule is untilted with respect to the layer normal and the tilt angle for each molecule in the structure is shown in the figure. The formation of shells with increasing tilt is clearly evident. For larger clusters, with interaction sites spaced $\geq 1.2\sigma$ the structures are arranged in shells that are untilted with respect to each other resulting in an achiral barrel-shaped configuration. When the interaction sites are spaced at distances of less than 0.7σ although chiral structures are observed for small cluster sizes, achiral structures are the minimum energy structures for large cluster sizes. For the smaller clusters, the tilt that

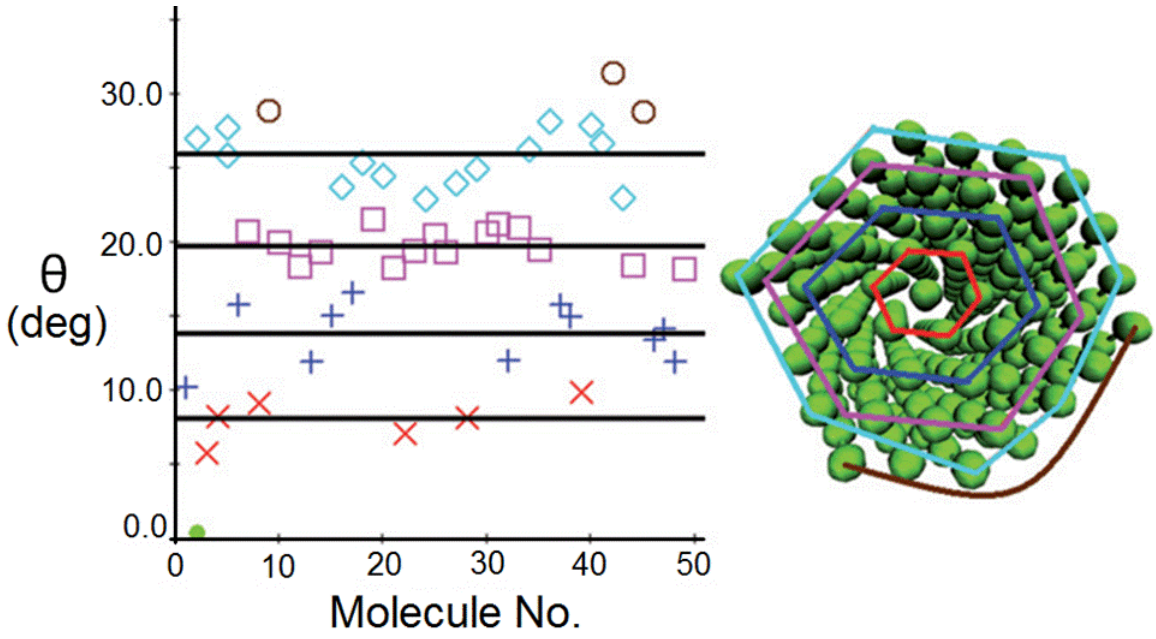

Figure 13: Shell model characterizing a chiral micelle. The micelle is divided into four shells based on the tilt angle, θ, of the molecules with respect to the layer normal. The average tilt angle for each shell increases from the inner to the outer shells: $8.0 \pm 2.0°$, $13.8 \pm 3.0°$, $19.7 \pm 1.7°$, and $25.5 \pm 2.6°$, for the first (red), second (blue), third (magenta), fourth (turquoise) and fifth (brown) shells respectively. The central molecule (molecule number 2) is untilted with respect to the layer normal. Tilt angles for individual molecules are shown in the graph with colours corresponding to the shells in which they are present.

creates the chirality promotes optimal contacts for molecules on the edge of the cluster, although an untilted structure would optimize the energy of the central molecule of the cluster. In larger structures, the ratio of the number of molecules fully coordinated compared to those on the edge is greater and an untilted achiral micelle becomes the minimum energy structure. The minimum energies found for clusters of 50 molecules are -1983.150ε (0.5σ spacing), -1735.725ε (0.6σ spacing), -1549.636ε (0.7σ spacing), -1429.631ε (0.8σ spacing), -1329.361ε (0.9σ spacing), -1255.961ε (1.0σ spacing), -1204.764ε (1.1σ spacing), -1208.849ε (1.2σ spacing), -1229.378ε (1.3σ spacing), -1282.014ε (1.4σ spacing), and -1338.036ε (1.5σ spacing).

The spacing of the Lennard-Jones sites has thus been observed in the above simulations to control the superstuctural chirality of micelle structures, and the correct spacing of sites is also a required component in the formation of the chiral column structures that are also observed here. This feature, then, may act as a design principle by which these structures can be realized, for example with colloidal building blocks.[9] In addition, discrete interaction sites also favour the tilting of smectic phases and can easily be rationalized by the preferential alignment of two molecules as shown in Fig. 8b.

5.4 CONCLUSION

In this chapter, the phase behaviour of linear rigid molecules that are chemically patterned with Lennard-Jones and Weeks-Chandler-Andersen beads has been studied using molecular dynamics simulations in the isothermal-isobaric ensemble. Interesting chiral superstructures have been observed at low pressures, including micelles and columns. At higher pressures and/or lower temperatures, achiral columns and untilted and tilted smectic phases including the smectic A, smectic C and smectic I phases have been observed. A nematic phase has also been observed at high pressures. Superstructural chirality has been shown to be tuned into rigid linear molecules by the appropriate spacing of Lennard-Jones sites, pointing to design rules that can be manipulated for the experimental synthesis of chiral structures from achiral molecules. It is also posited that the discrete nature of the interactions in the model are responsible for the observation of tilted smectic phases.

6.0 A COMPREHENSIVE SIMULATION STUDY OF THE PHASE BEHAVIOR OF RIGID BENT-CORE MOLECULES

Manuscript in preparation

Yan, F.; Hixson, C. A.; Earl, D. J.

6.1 INTRODUCTION

In previous chapters[52, 67], molecular dynamics simulations were performed on a rigid achiral bent-core molecule model in both the canonical (NVT) ensemble and the isotropic-isobaric (NPT) ensemble in chapter 4, and on a linear rigid molecule model in the isotropic-isobaric (NPT) ensemble in chapter 5. In that bent-core model, the bending angle γ was fixed at 150°. The number of Lennard-Jones (LJ) particles per molecule N_A is 5, and the number of Weeks-Chandler-Andersen (WCA) particles per molecule N_B is 4. The number of LJ and WCA particles preserved, but the angle γ was changed to 180° to make the linear model. In both models, chiral micelle (CM) and chiral column (CC) were observed to form at low volume ratios ϕ in the NVT simulations, or at low pressures in the NPT simulation. And liquid crystalline phases, such as smectic A (SmA), smectic C (SmC) and smectic I (SmI), were observed to form at high volume ratios ϕ in the NVT simulations, or at high pressures in the NPT simulations.

In this chapter, the previous work is extended to investigate the molecular shape effect on the phase behavior of the bent-core molecules by varying the bending angle γ, where $\gamma = 150°$, 120°, or 90°; and the arm length ratio N_A / N_B, where N_A is fixed as 5, and N_B is varied from 4 to 1. Molecular dynamics (MD) simulations are used to study these systems

in both the canonical ensemble and the isothermal-isobaric ensemble, and construct 1 / T^* (inverse temperature) vs. ϕ (volume ratio) phase diagrams in the canonical ensemble, and 1 / T^* (inverse temperature) vs. P^* (the reduced pressure) phase diagrams in the isothermal-isobaric ensemble. Two important features have been found for the model systems. First, the molecular shape has a strong effect on the phase behavior of bent-core model systems. Second, three phases, including staired micelles (SM), staired columns (SC), and achiral short layers (ASL), have been found which did not form in the previous study.

This work is organized as follows. The bent-core model and simulation method are presented in Sec. 6.2. In Sec. 6.3, the phase behavior of bent-core molecules at a bending angle $\gamma = 150°$, with $N_A = 5$ and $N_B = 4$, is first discussed, followed by the phase behaviors of bent-core molecules at different bending angles γ and different arm length ratios N_A / N_B. Finally the conclusion is made in Sec. 6.4.

6.2 COMPUTATIONAL DETAILS

An example of a bent-core model molecule was previously shown in chapter 4 (Fig. 4a). In this chapter, the number of LJ particles N_A is fixed at a value of 5, and different numbers of WCA particles N_B are used and the values are equal to 1, 2, 3 or 4. This corresponds to varying the arm length ratio, N_A / N_B. At each arm length ratio, different bending angles γ are used with values equal to 90°, 120°, or 150°. To avoid system size effects, different simulation sizes are used with a total number of molecules M = 2500, 3000, 4000, 4500, 4800, 5000, 6000 and 9600 molecules in the NVT ensemble, and 3000 and 6000 molecules in the NPT ensemble. All quantities related to the simulations are expressed in reduced units[88]. A time step of 5 $\times$ 10^{-3} t^* is used in both NVT and NPT simulations. The NO_SQUISH integrator of Miller *et al.*[111] is chosen for rigid bodies, and an operator splitting method proposed by Kamberaj *et al.*[112] is used. In the NVT simulations, the systems are prepared at a variety of volume ratio ϕ, and heated until they are isotropic. The systems are then slowly cooled at a rate of 0.25 reduced temperature units for 1.5 $\times$ 10^5 steps followed by an equilibration period of 3.0 $\times$ 10^5 steps. Near phase transitions, this process

is slowed by increasing the equilibration steps and manually observed to ensure that equilibrium was maintained. The observed phases are recorded from these trajectories. In the NPT simulations, the systems are prepared in the isotropic phase at a variety of pressures and then slowly annealed following the same procedures as in the NVT simulations. The NPT simulations were also performed in a different way, where the systems are prepared in the isotropic phase at a variety of temperatures, and then the pressures of these systems are slowly increased at a rate of 0.25 reduced pressure units for 1.5×10^5 steps followed by an equilibration period of 4.5×10^5 steps. Near phase transitions, this process is slowed down and checked to ensure the equilibrium was maintained. All phases are observed in both NVT and NPT simulations.

Monte Carlo parallel tempering simulations[69] were also performed to understand the thermodynamic basis for the micelle formation at low densities. Parallel tempering simulations are performed inside a spherical enclosure of radius 25 σ for systems containing 50 molecules, a typical size for a micelle. These simulations use Monte Carlo moves that change the center of mass position and orientation of randomly selected molecules. Eighteen parallel tempering replicas are used, by employing a low temperature of $T^* = 0.45$. The temperatures of other replicas are allowed to vary adaptively until the swapping ratios are optimized and close to 0.20[138].

6.3 RESULTS AND DISCUSSION

In this section, the phase behaviors of bent-core molecules at bending angles $\gamma = 150°$, $120°$, and $90°$, with $N_A = 5$ and $N_B = 4$, will be presented first, followed by those of bent-core molecules at bending angles $\gamma = 150°$, $120°$, or $90°$, with a fixed $N_A = 5$ at each arm ratio defined by $N_B = 3$, 2, or 1.

6.3.1 $N_A = 5$ and $N_B = 4$, $\gamma = 150°$

The phase diagram in the NVT has been shown in chapter 4 in Fig. 5, and for a comparison, the phase diagram in the NPT is shown here in Fig. 14.

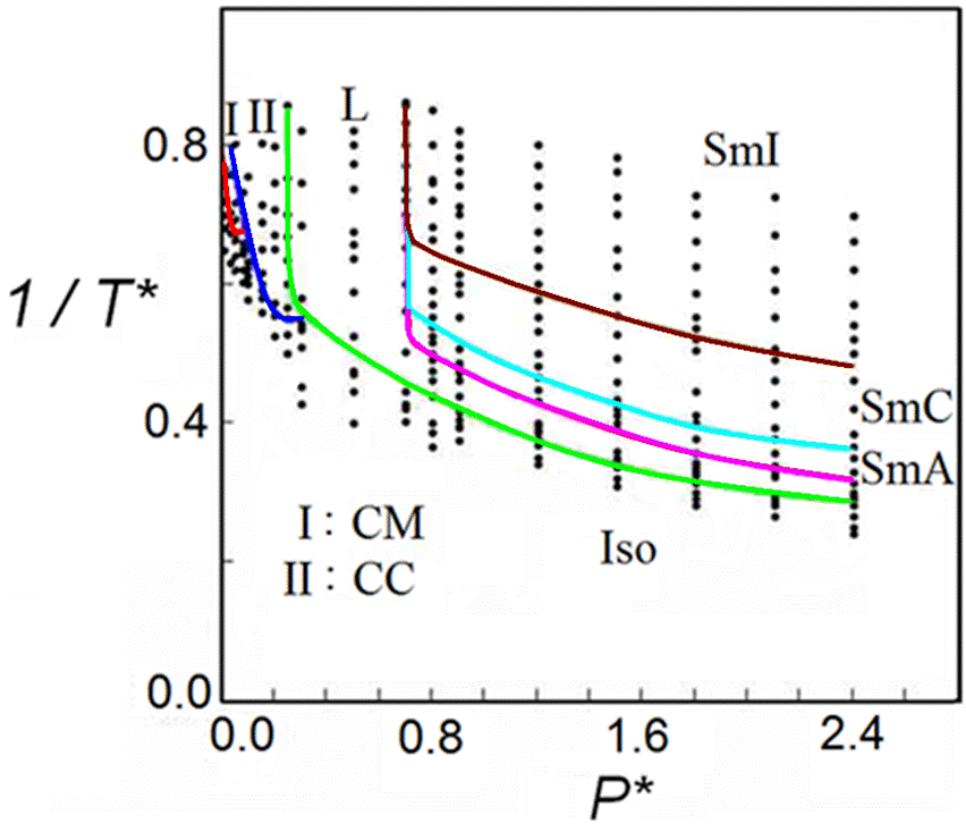

Figure 14: Phase diagram of bent-core molecules with the bending angle $\gamma = 150°$ and the arm length ratio N_A / N_B = 5 / 4 in the isothermal-isobaric (NPT) ensemble. At reduced pressures greater than 0.30, the system forms the nematic (N) (not shown), lamellar (L), smectic A (SmA), smectic C (SmC) and smectic I (SmI) phases. At lower pressures, the chiral phases form, including chiral micelle (CM) and chiral column (CC) phases. The isotropic (Iso) phase is found at high temperatures for all pressures.

In both simulations, (Figs. 5 and 14) the systems exhibit rich phase behavior including the isotropic (Iso), chiral micelle (CM), chiral column (CC), nematic (N), lamellar (L), smectic A (SmA), smectic C (SmC), and smectic I (SmI) phases. The properties of all these

phases are discussed as follows.

A detailed discription of the chiral micelle phases (CM and CC) formed by bent-core molecules has been given in chapter 4. Thus, only liquid crystalline phases are discussed here. All the liquid crystalline phases are listed in Fig. 15.

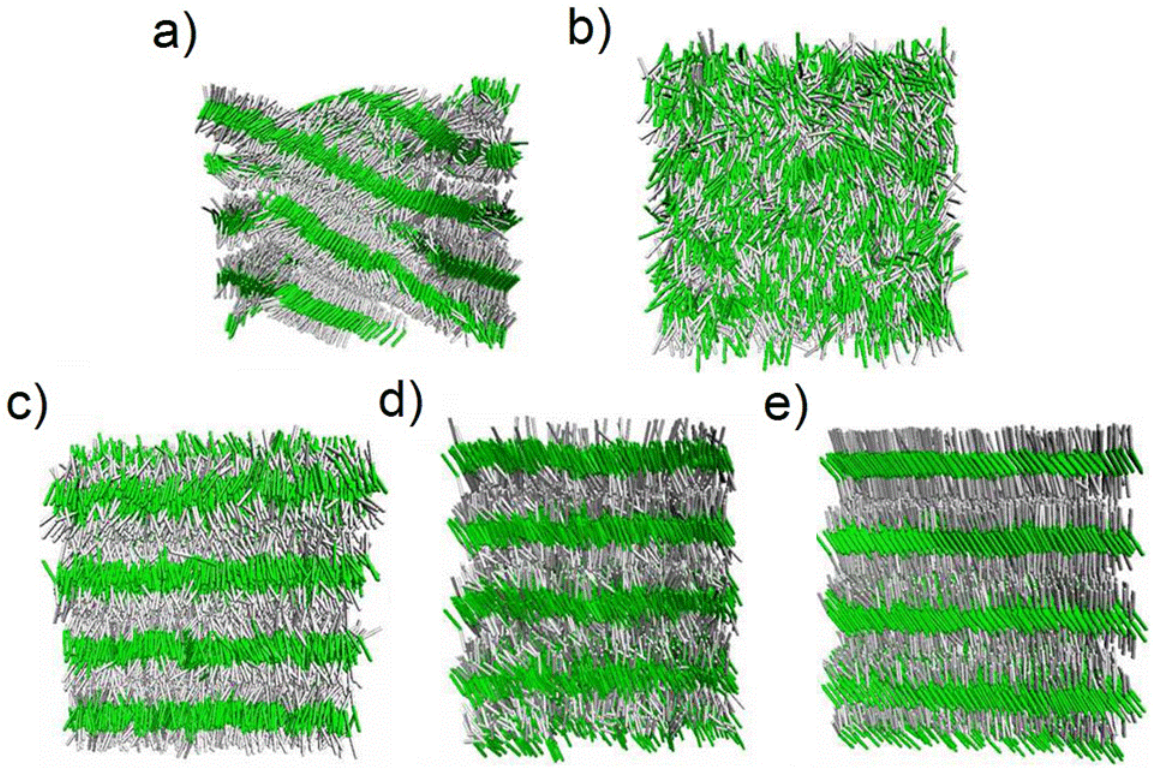

Figure 15: (a) A lameller (L) phase obtained from a system of $M = 4800$ bent-core molecules at $\phi = 0.24$ and $1/T^* = 0.8$ in the NVT simulation. (b) A nematic (N) phase obtained from a system of $M = 3000$ bent-core molecules at $P^* = 7.0$ and $1/T^* = 0.16$ in the NPT simulation. (c) A smectic A (SmA) phase obtained from a system of $M = 4800$ bent-core molecules at $\phi = 0.28$ and $1/T^* = 0.43$ in the NVT simulation. (d) A smectic C (SmC) phase obtained from a system of $M = 9600$ bent-core molecules at $\phi = 0.30$ and $1/T^* = 0.50$ in the NVT simulation. (e) A smectic I (SmI) phase obtained from a system of $M = 9600$ bent-core molecules at $\phi = 0.30$ and $1/T^* = 1.13$ in the NVT simulation. All bent-core molecules have a bending angle $\gamma = 150°$, with $N_A = 5$ and $N_B = 4$.

The lamellar phase (L) is shown in Fig. 15a. This phase forms for $\phi \geq 0.21$ in the NVT

simulations, and for reduced pressures $P^* \geq 0.30$ in the NPT simulations. This phase has layers formed by the Lennard-Jones portion of this model, with each layer being separated by disordered layers of the WCA portion. At higher volume ratios ϕ in the NVT simulations, or higher P^* in the NPT simulations, the layers become ordered and form smectic phases. And at even higher volume ratios or P^*, a nematic (N) phase forms. We now proceed to discuss the N and the smectic phases.

A nematic (N) phase (Fig. 15b) is observed to form for volume ratios $\phi \geq 0.33$ in the NVT simulations, and for $P^* \geq 7.0$ in the NPT simulations. The N phase has orientational order along the system director, but no formation of layers, indicating that it has no positional order.

Three smectic phases including SmA, SmC and SmI, are observed to form for volume ratios ϕ between 0.28 and 0.36 in the NVT simulations, and for P^* between 0.70 and 3.50 in the NPT simulations. The SmA phase forms at higher temperatures than the other two smectic phases. As shown in Fig. 15c, the SmA phase has definite layers, which have no tilt relative to the layer normal of the system. Inside the layer, the molecules show no long-range ordering and are liquid-like. As the temperature decreases, a phase transition from SmA to SmC phase occurs in both the NVT and NPT simulations. As shown in Fig. 15d, the SmC phase is the tilt analogue of the SmA phase, and inside the layer, there is also no positional ordering. At even lower temperatures, a phase transition from SmC to SmI occurs in both NVT and NPT simulations. Although similar to the SmC phase with the tilted layer structure, the SmI phase (see Fig. 15e) differs by having local hexagonal ordering within the layer and an in-layer tilt towards the hexagonal apex.

In order to gain more information on the structure of smectic phases, two distribution functions were calculated: a longitudinal distribution function $g_{\parallel}(r)$ was used to characterize the smectic layers, and an in-plane distribution function $g_{\perp}(r)$ to characterize the structure within the layers.

The longitudinal distribution function $g_{\parallel}(r)$ is shown in Fig. 16a. The oscillatory peaks are shown in the SmA phase, indicating ordered layer packing. In the SmC and SmI phases the periodic peaks become both sharper and more intense. The largest intensity is found for the SmI phase, indicating it has the highest positional order along the layer. The average

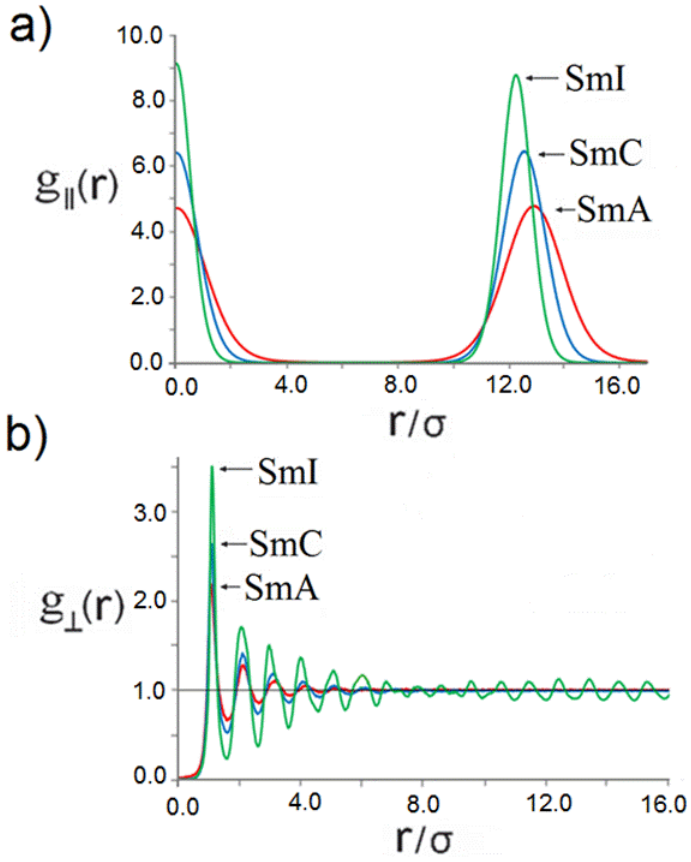

Figure 16: (a) The longitudinal distribution function, $g_{\parallel}(r)$, for a system of $M = 3000$ bent-core molecules at $P^* = 0.8$ in the NPT simulation. (b) The in-plane distribution $g_{\perp}(r)$, for a system of $M = 3000$ bent-core molecules at $P^* = 0.8$ in the NPT simulation. All bent-core molecules have a bending angle $\gamma = 150°$, with $N_A = 5$ and $N_B = 4$. The distribution functions for SmA, SmC and SmI are in green, blue and red, respectively.

separations between the peaks can be used to determine the layer spacing, and are calculated to be 12.78σ, 12.50σ and 12.19σ for SmA, SmC and SmI, respectively. The in-plane distribution function $g_{\perp}(r)$ is shown in Fig. 16b. In both SmA and SmC phases, the structures within the layers are liquid-like with no long range structure. In the SmI phase, however, the in-plane order extends out to a larger distance and a fine structure occurs in the long range peaks. The peaks constituting this fine structure is separated by a distance of 1.0σ, which can be attributed to a hexagonal order within the layer. Because of the long range

oscillations and hexgonal order within the layer, this phase may also be a deformed crystal J phase[38], although the simulation system size is not enough to differentiate between the two. The average tilt angle relative to the layer normal is also measured in each of the smectic phases in each of the NPT simulations. The tilt angle increases during the phase transition from SmC to SmI phase, and reaches a maximum at approximately 28.0° in the SmI phase at $P^* = 1.5$.

In the smectic phases, the LJ particles of the system tend to stack together in order to minimize the free energy of the system, and the rotational entropy from the purely repulsive WCA particles can also contribute to lower the free energy, thus stabilize the formation of these phases. A number of notable computational studies of coarse-grained model systems[158, 162, 159, 144, 25, 26, 52, 67] have found tilted smectic phases, including the rigid bent-core and linear models described in chapters 4 and 5. Dewar and Camp[158] have found that rigid bent-core molecules composed entirely of LJ particles can form an alternating tilted smectic B (SmB) phase with no global tilt. Nguyen *et al.*[162] have found that by attaching flexbile WCA particles along only one end of rigid bent-core LJ particles, a SmC phase with a global tilt can form, and the SmC phase disappears after attaching flexible WCA particles on the other end of the bent-core LJ particles. Although purely repulsive linear or bent-core model molecules have not been found to form SmC phase, Xu *et al.*[159] have shown that zig-zag shaped molecules composed of entirely WCA particles with a bending angle of 5.0° can form a SmC phase by applying a strong electric field. Also Maiti *et al.*[144] have used a zigzag model by linking three hard spherocylinders in a zigzag configuration, and found that by increasing the bending angle of the zig-zag model molecules up to 28.0° or higher, a SmC phase can form. Comparing the model here and Nguyen *et al.*'s[162] model, on one hand, to the other three models, it is evident that the addition of WCA sites to our model molecules results in a global tilt of the entire SmC phase, whilst the inclusion of LJ sites stabilizes the tilting of layers in the absence of an external electric field, and finally the use of a zig-zag shape model also favors the SmC formation. On the other hand, the difference between the results from our model and those from Nguyen *et al.*'s[162] model is that there is no chiral micelle phase found in their model. However, very interestingly, the SmC phase formed in their model has chirality varying randomly for neighboring

smectic layers, which is reminiscent of the chiral smectic C phase (B2)[40] although their system size is not enough to confirm this finding. Moreover, in a polymer-tethered nanorod model, which is made of rigid LJ particles attached by flexible WCA particles along one end of LJ particles, Horsch *et al.*[25, 26] have found chiral micelle phases and SmC phase. Thus, comparing the model here and Horsch *et al.*'s[25, 26] model, on the one hand, with that of Nguyen *et al.*'s[162], the introduction of a bending angle γ of 140° in the rigid LJ particles of Nguyen *et al.*'s model causes a steric effect which results in no formation of chiral micelle phases. On the other hand, in Horsch *et al.*'s[25, 26] model, there is no nematic, SmA or SmI phases formed. By comparing ours with Horsch *et al.*'s[25, 26] model, the introduction of rigidity in the WCA section clearly stabilizes the nematic and smectic A phases.

6.3.2 $N_A = 5$ and $N_B = 4$, $\gamma = 120°$ and 90°

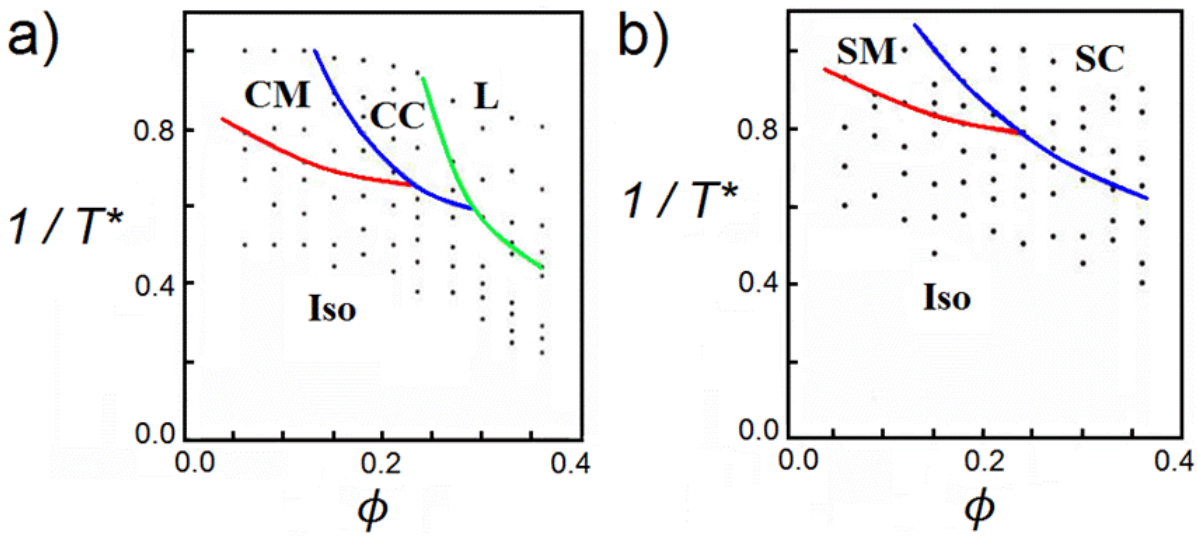

Figure 17: Phase diagram of bent-core molecules with $N_A = 5$ and $N_B = 4$ at different bending angles γ in the NVT simulations. (a) $\gamma = 120°$. At volume ratios ϕ higher than 0.23, the L phase forms; at lower volume ratios, chiral micelles including the CM ($\phi < 0.23$) and CC ($0.15 \leq \phi < 0.29$) phases develop. (b) $\gamma = 90°$. At volume ratios higher than 0.15, the SC phase forms; at volume ratios lower than 0.23, the SM phase forms.

To investigate the angle effect on the phase behavior of bent-core molecules with $N_A = 5$ and $N_B = 4$, both NVT and NPT simulations were performed for model systems with $\gamma = 120°$ and $90°$. All phases found in the NVT simulations were also found in the NPT simulations. The $1/T^*$ vs. ϕ phase diagrams are presented for model systems with $\gamma = 120°$ in Fig. 17a and $\gamma = 90°$ in Fig. 17b.

For the bending angle $\gamma = 120°$, at $\phi < 0.23$, the CM and CC phases develop. At $\phi > 0.23$, the lamellar (L) phase forms. Notably, at higher volume ratios, there was no smectic phases or nematic phase formed. This disappearance of the smectic phases and nematic phase in going from $\gamma = 150°$ to $\gamma = 120°$ may be attributed to the steric effect arising from the purely repulsive WCA particles. The steric effect is stronger at $\gamma = 120°$ (see Fig. 18) than at $\gamma = 150°$ (see Figs. 15c-15e), and interferes with the self-assembly, to such an extent as to prevent any formation of liquid crystalline phases.

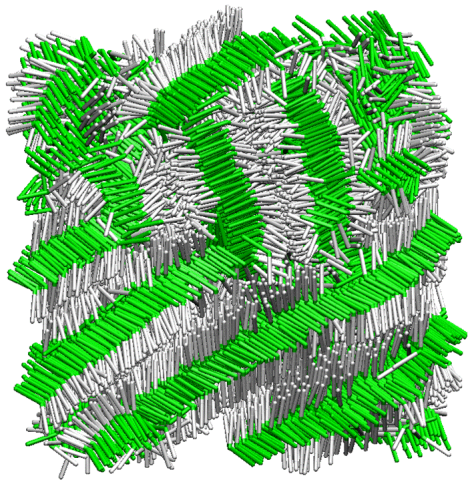

Figure 18: A lamellar phase (L) obtained from a system of $M = 4800$ bent-core molecules with $N_A = 5$, $N_B = 4$ at the bending angle $\gamma = 120°$ with a volume ratio $\phi = 0.36$ and $1/T^* = 1.8333$ in the NVT simulation. The frustrated packing caused by steric effects from a low bending angle can be seen clearly in this figure.

For the bending angle $\gamma = 90°$, at volume ratios lower than 0.23, a staired micelle phase formed (Fig. 19a). Three types of micelles are found in this phase including the achiral,

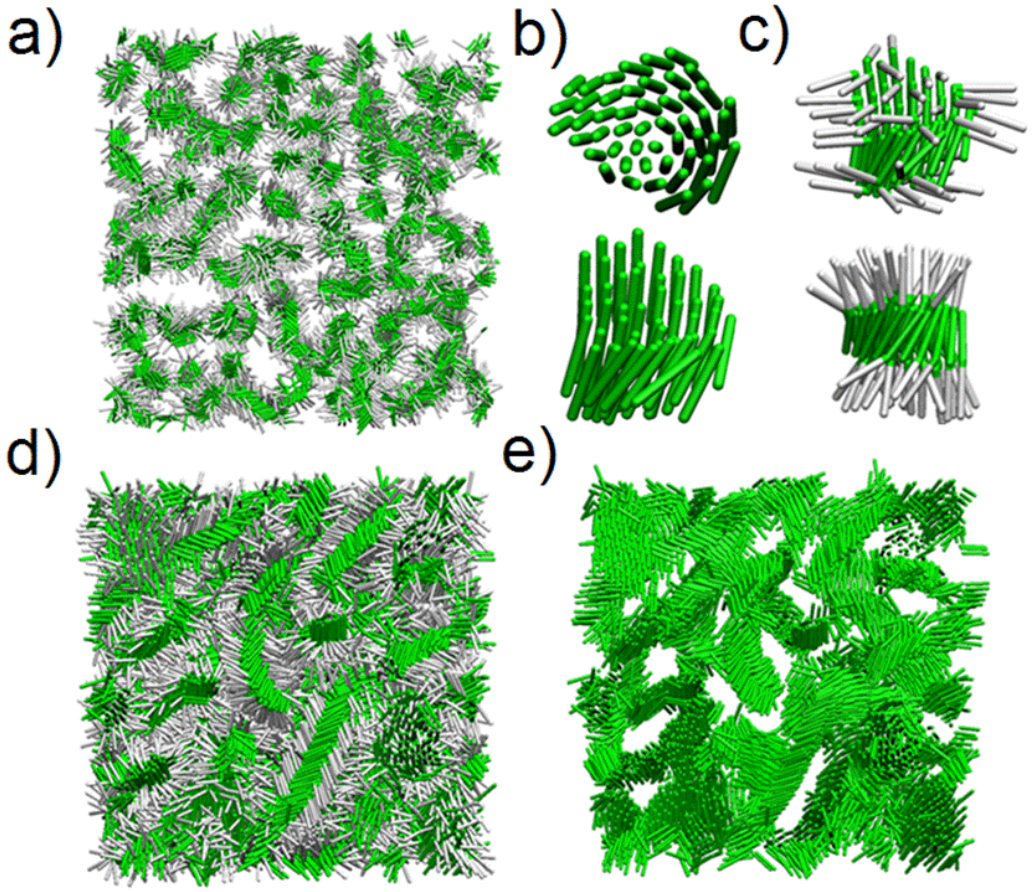

Figure 19: (a) Staired micelle phase (SM) obtained from a system of $M = 4800$ bent-core molecules at $\phi = 0.06$ and $1/T^* = 1.0$ in the NVT simulation. (b) A left-handed staired micelle (SM) extracted from (a), where WCA particles are removed in order to guide viewing. (c) Top: a left-handed staired micelle (SM) for bent-core molecules at $\gamma = 90°$. Bottom: a left-handed chiral micelle (CM) for bent-core molecules at $\gamma = 150°$. (d) The staired elongated column phase (SC) obtained from a system of $M = 4800$ bent-core molecules at $\phi = 0.21$ and $1/T^* = 1.25$ in the NVT simulation. (e) The SC phase with WCA particles removed.

the left- (Fig. 19b) and the right-handed. The asphericity parameter A_s was calculated to quantify the shape of the micelles. It is found that on average $A_s = 0.200 \pm 0.01$. This value is higher than that of chiral micelles (0.06 ± 0.01) and shows that this structure is less

spherical than chiral micelles, as shown in Fig. 19c. To study the thermodynamic basis for the formation of staired micelles, Monte Carlo parallel tempering simulations were performed for a cluster of 50 molecules with $\gamma = 90°$. The structures of the minimal potential energy are found to exhibit achiral, left- and right-handed staired micelles, and thus are consistent with the NVT simulations. By comparing the staired micelle (SM) from $\gamma = 90°$ to the chiral micelle (CM) formed at $\gamma = 150°$, as shown in Fig. 19c, it is evident that the staired micelle is caused by the steric effect due to the smaller bending angle at $\gamma = 90°$.

As the volume ratio increases as high as 0.15, the systems start to form a staired column phase, as shown in Figs. 19d-19e. Just as the chiral columns are formed by aggregation of chiral micelles, the staired columns are formed by the aggregation of staired micelles.

6.3.3 $N_A = 5$, $N_B = 3$ at $\gamma = 150°$, 120° and 90°

In order to investigate the effect of arm length ratio N_A / N_B on the phase behaviors of bent-core molecules, only N_B was varied at values of 3, 2, or 1, since N_A is, as stated earlier in this chapter, always fixed at 5, across all the different systems studied. NVT molecular dynamics simulations were performed for all systems, and the $1/T^*$ vs. ϕ phase diagrams for these systems were constructed. The results of these phase diagrams are summarized in Fig. 20. All the phase diagrams are discussed as follows.

The phase diagrams for bent-core molecules with $N_A = 5$ and $N_B = 3$ at different bending angles of $\gamma = 150°$, 120° and 90° are shown in Figs. 21a, 21b and 21c, respectively.

At $\gamma = 150°$, eight phases formed namely the Iso, CM, CC, L, N, SmA, SmC and SmI phases (Figs. 20 and 21a). At lower volume ratios, the CM ($\phi \leq 0.15$) and CC ($0.09 \leq \phi \leq 0.20$) phases formed. At higher volume ratios, the liquid crystalline phases formed, including the SmA, SmC and SmI phases ($0.30 \leq \phi \leq 0.40$), and the N phase ($0.36 \leq \phi \leq 0.40$). Between the micelle phases and liquid crystalline phases, lies the L phase ($0.21 \leq \phi \leq 0.40$). Compared with the bent-core molecules with $N_A = 5$ and $N_B = 4$ at the same bending angle $\gamma = 150°$ (see Fig. 5 in chapter 4), the phase diagram is similar and all phases which developed in those systems also developed here. The main difference is that first the liquid crystalline phases start to form at higher volume ratios in $N_B = 3$ than those in $N_B = 4$,

a)

Phase	CM	CC	ASL	L	SmA	SmC	SmI	N
$N_B = 4$	$\phi < 0.15$	$0.12 < \phi \leq 0.23$		$0.21 < \phi \leq 0.36$	$0.28 \leq \phi \leq 0.36$	$0.28 \leq \phi \leq 0.36$	$0.28 \leq \phi \leq 0.36$	$0.33 \leq \phi \leq 0.36$
$N_B = 3$	$\phi \leq 0.15$	$0.09 \leq \phi \leq 0.20$		$0.20 < \phi \leq 0.40$	$0.30 \leq \phi \leq 0.40$	$0.30 \leq \phi \leq 0.40$	$0.30 \leq \phi \leq 0.40$	$0.36 \leq \phi \leq 0.40$
$N_B = 2$	$\phi \leq 0.15$	$0.12 \leq \phi \leq 0.18$	$\phi < 0.24$	$0.21 < \phi \leq 0.44$	$0.33 \leq \phi \leq 0.44$	$0.33 \leq \phi \leq 0.44$	$0.33 \leq \phi \leq 0.44$	$0.42 \leq \phi \leq 0.44$
$N_B = 1$			$\phi < 0.30$	$0.24 < \phi \leq 0.44$	$0.36 \leq \phi \leq 0.44$	$0.36 \leq \phi \leq 0.44$	$0.36 \leq \phi \leq 0.44$	

$\gamma = 150°$

b)

Phase	CM	CC	ASL	L	SmA	SmC	SmI
$N_B = 4$	$\phi < 0.23$	$0.15 \leq \phi < 0.29$		$0.23 < \phi \leq 0.36$			
$N_B = 3$	$\phi < 0.20$	$0.15 \leq \phi < 0.26$		$0.24 < \phi \leq 0.36$		$0.30 \leq \phi \leq 0.36$	$0.30 \leq \phi \leq 0.36$
$N_B = 2$	$\phi < 0.19$	$0.09 < \phi < 0.29$		$0.24 < \phi \leq 0.38$		$0.33 \leq \phi \leq 0.38$	$0.33 \leq \phi \leq 0.38$
$N_B = 1$		$\phi < 0.29$	$\phi < 0.32$	$0.27 < \phi \leq 0.42$	$0.35 \leq \phi \leq 0.42$	$0.315 \leq \phi \leq 0.42$	$0.315 \leq \phi \leq 0.42$

$\gamma = 120°$

c)

Phase	SM	SC	CC
$N_B = 4$	$\phi < 0.23$	$0.15 \leq \phi \leq 0.36$	
$N_B = 3$	$\phi < 0.23$	$0.15 \leq \phi \leq 0.36$	
$N_B = 2$	$\phi < 0.16$	$0.12 \leq \phi \leq 0.36$	
$N_B = 1$		$0.21 < \phi \leq 0.33$	$\phi < 0.238$

$\gamma = 90°$

Figure 20: Summary tables for different bent-core model systems, (a) with bending angle $\gamma = 150°$, with $N_A = 5$, and $N_B = 4$, 3, 2, 1; (b) with bending angle $\gamma = 120°$, with $N_A = 5$, and $N_B = 4$, 3, 2, 1; (c) with bending angle $\gamma = 90°$, with $N_A = 5$, and $N_B = 4$, 3, 2, 1.

as shown in the summary table (Fig. 20); and second at the same volume ratio ϕ, the phase transition temperatures are lower in $N_B = 3$ than those in $N_B = 4$. For example, all three smectic phases start to form at $\phi = 0.30$ in $N_B = 3$, compared to $\phi = 0.28$ in $N_B = 4$. Also the nematic phase starts to form at $\phi = 0.36$ in $N_B = 3$, compared to $\phi = 0.33$ in $N_B = 4$. The second difference is exemplified by the fact that at the volume ratio $\phi = 0.36$, the phase transition temperatures for Iso $\longrightarrow$ N $\longrightarrow$ L $\longrightarrow$ SmA are 5.60, 4.95, and 3.92 respectively in $N_B = 3$, compared to the corresponding 12.0, 5.58, and 4.25 in $N_B = 4$. It is posited that

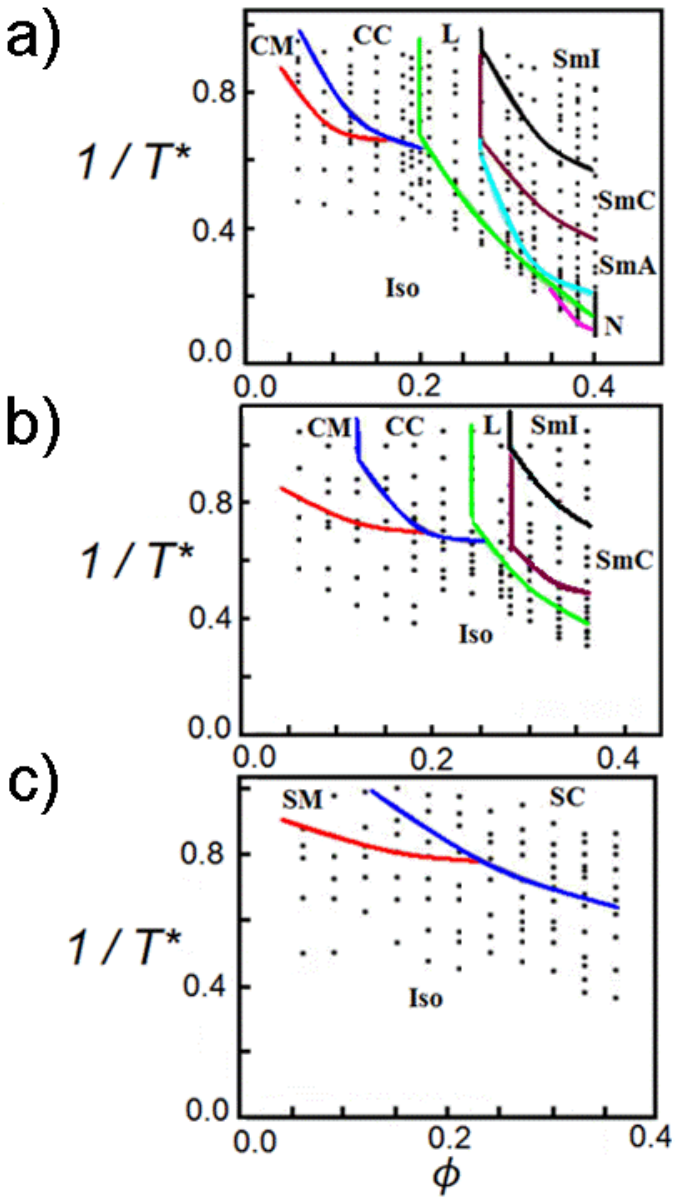

Figure 21: Phase diagram of bent-core molecules of $N_A = 5$ and $N_B = 3$ at (a) bending angle $\gamma = 150°$, (b) $\gamma = 120°$ and (c) $\gamma = 90°$ in the NVT simulations.

this difference in phase behavior between $N_B = 3$ and $N_B = 4$ at the bending angle $\gamma = 150°$ may be caused by a packing effect. As shown in Fig. 22, at the same volume ratio of $\phi = 0.33$ and the same temperature $T^* = 4.25$, the bent-core molecules with $N_B = 4$ are packed more closely, and result in the formation of the SmA layers. In the case of $N_B = 3$, the molecules

are less closely packed and form a lamellar phase (Fig. 22b). And in order to form smectic phases in $N_B = 3$, the temperature needs to be lowered so that LJ particles can more easily stack to form the smectic layers, and thus minimize the free energy of the system. A more significant change is shown in Fig. 22c, where by decreasing N_B further to 2 at the same T^* and ϕ, the molecules have a lower packing density and form only the isotropic phase. The $N_B = 1$ system behaves similarly. This packing effect has also been found in linear molecules ($\gamma = 180°$) with $N_A = 5$, but with different values of N_B, and $N_B = 4$, 3, 2 or 1. For example, for linear molecules with $N_B = 4$, the reduced phase transition temperature for L $\longrightarrow$ SmA is 6.10, compared to 5.70 or 4.75 for linear molecules with $N_B = 3$, or $N_B = 2$, respectively.

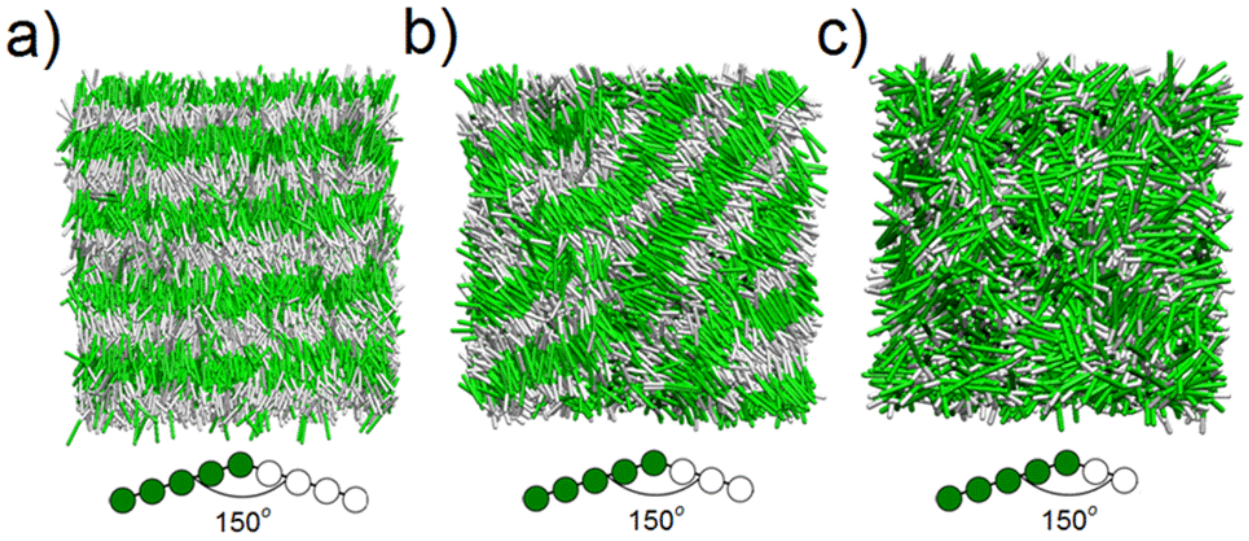

Figure 22: Investigation of arm length ratio N_A/N_B effect on the phase behavior of bent-core molecules with fixed N_A ($N_A = 5$) at the same bending angle $\gamma = 150°$, but with different N_B. All simulations were performed at the same volume ratio $\phi = 0.33$ and the same temperature $T^* = 4.25$ in the NVT simulations. (a) $N_B = 4$, a SmA phase forms from $M = 4800$ molecules; (b) $N_B = 3$, a lamellar phase forms from $M = 5000$ molecules; (c) $N_B = 2$, an isotropic phase forms from 3000 molecules.

At $\gamma = 120°$, six phases form including the Iso, CM, CC, L, SmC and SmI phases (Figs.

20 and 21b). At lower ϕ, the CM ($\phi < 0.20$) and CC ($0.15 \leq \phi < 0.26$) phases formed. At higher ϕ, two liquid crystalline phases developed including the SmC and SmI phases ($0.30 \leq \phi \leq 0.36$). And the L ($0.24 < \phi \leq 0.36$) phase lies between. Compared with the bent-core molecules with $N_A = 5$ and $N_B = 4$ at the same bending angle $\gamma = 120°$ (see phase diagram in Fig. 17a), the major difference is that two liquid crystalline phases, the SmC and SmI phases, formed here. In previous section, it has been found that the small bending angle for bent-core molecules with $N_A = 5$ and $N_B = 4$ causes the packing frustration for the smectic layers so that no smectic phases formed when $\gamma = 120°$ and $90°$. Thus, by decreasing N_B from 4 to 3, the steric effect caused by small bending angles is sufficiently decreased to allow the tilted smectic C and SmI phases to form (see Fig. 18 and Fig. 23a for a comparison).

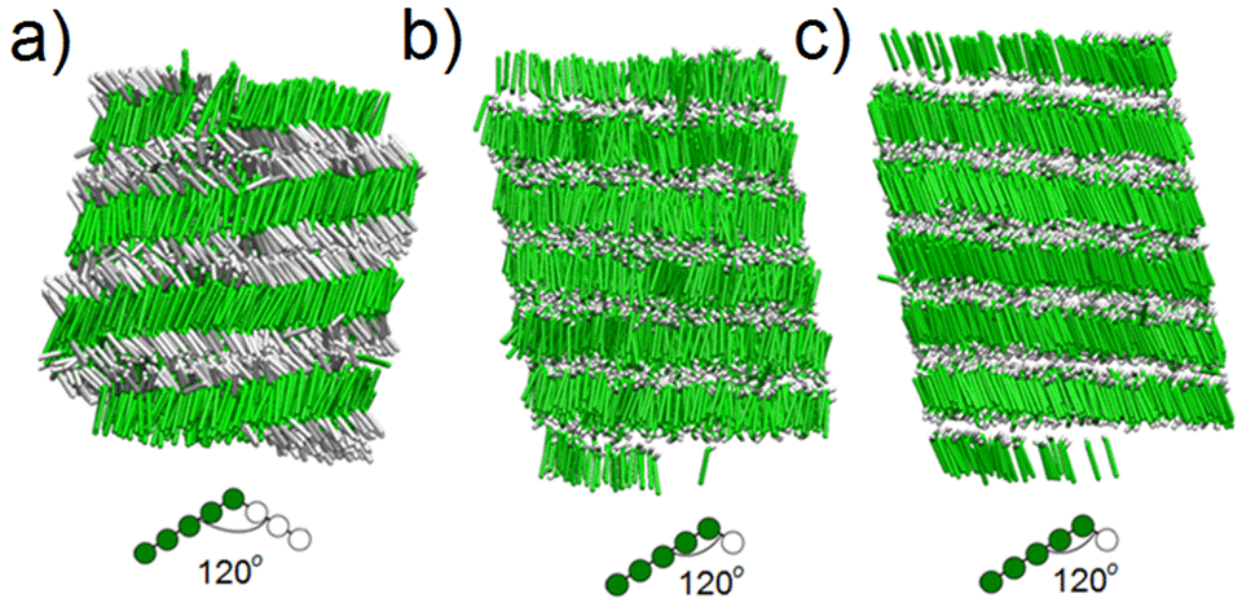

Figure 23: The steric effect from the smaller bending angle $\gamma = 120°$ can be alleviated by a decrease of WCA particles per molecule, which results in (a) forming SmC phase from 2500 bent-core molecules with $N_B = 3$, at a volume ratio $\phi = 0.36$ and $T^* = 2.25$ in a NVT simulation, (b)-(c), SmA and SmC phases form from 3000 bent-core molecules wih $N_B = 1$, at a volume ratio $\phi = 0.36$ and $T^* = 1.65$ for SmA phase, and 1.40 for SmC phase in a NVT simulation.

However, because there is still a steric effect, the SmA phase did not form in this system nor in the system with $N_B = 2$ at $\gamma = 120°$. When N_B is decreased to 1, the steric effect is decreased such that SmA phase also forms, as shown in Figs. 23b-c. This steric effect from small bending angles on liquid crystalline phases is also shown clearly in the summary tables of Fig. 20.

For bent-core molecules with $N_A = 5$ and $N_B = 3$, transition temperature change of liquid crystalline phases at different bending angles of $\gamma = 150°$ and $120°$ has been calculated and compared. It is found that at the same ϕ, the phase transition temperature at $150°$ is higher than that at $120°$. For example, for bent-core molecules with $\gamma = 150°$ at $\phi = 0.36$, the phase transition temperatures for Iso $\longrightarrow$ L $\longrightarrow$ SmC are $T^* = 4.95$ and 2.38, compared to 2.61 and 2.06 for bent-core molecules with $\gamma = 120°$. This may also be caused by a packing effect. At the bending angle of $\gamma = 150°$, the steric effect caused by the WCA particles is alleviated compared to $\gamma = 120°$, so the LJ particles can have a closer packing, and form more ordered smectic layers than the system at $\gamma = 120°$. And these more ordered smectic layers need a higher melting temperature to break the order, which corresponds to a higher phase transition temperature. Thus, by increasing the bending angle, γ, the angle steric effect will be decreased and LJ particles are easier to stack together to form layers, which results in higher phase transition temperatures from the less ordered phase to the liquid crystalline phases. The same trend has also been found between linear molecules and bent-core molecules with the same values of N_A and N_B. For example, for the same $N_A = 5$ and $N_B = 3$ at $\phi = 0.36$, the phase transition temperature for linear molecules for L $\longrightarrow$ SmA is 5.70, compared to 3.92 for the corresponding bent-core molecules at $\gamma = 150°$.

At $\gamma = 90°$, only the Iso, SM and SC phases formed (Figs. 20 and 21c): SM at the lower volume ratios ($\phi < 0.23$), and SC at the higher volume ratios ($0.15 \leq \phi \leq 0.36$). The phase diagram (Fig. 21c) is very similar to that of bent-core molecules with $N_A = 5$, $N_B = 4$ at bending angle $\gamma = 90°$ in Fig. 17b.

6.3.4 $N_A = 5$, $N_B = 2$ at $\gamma = 150°$, $120°$ and $90°$

The phase diagrams for bent-core molecules with $N_A = 5$ and $N_B = 2$ at different bending angles of $\gamma = 150°$, $120°$ and $90°$ are shown in Figs. 24a, 24b and 24c, respectively.

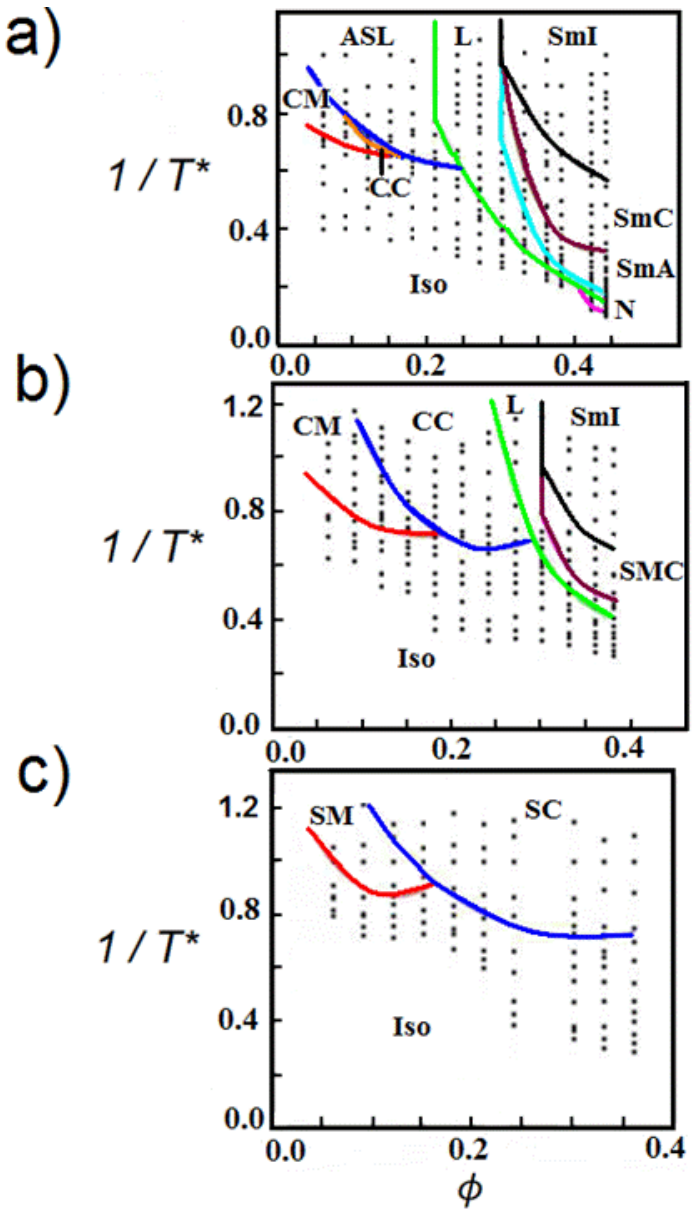

Figure 24: Phase diagram of bent-core molecules of $N_A = 5$ and $N_B = 2$ at (a) bending angle $\gamma = 150°$, (b) $\gamma = 120°$ and (c) $\gamma = 90°$ in the NVT simulations.

At $\gamma = 150°$, nine phases formed: these are the Iso, CM, CC, achiral short layer (ASL), L, N, SmA, SmC and SmI phases (See Figs. 20 and 24a). The CM ($\phi \leq 0.15$), the CC ($0.12 \leq \phi \leq 0.18$) and the ASL ($\phi < 0.24$) phases formed at the lower volume ratios, while the liquid crystalline phases [the SmA, SmC and SmI ($0.33 \leq \phi \leq 0.44$)] and the N phase ($0.42 \leq \phi \leq 0.44$) formed at higher volume ratios. The L phase ($0.21 \leq \phi \leq 0.44$) lies between the micelle phases and liquid crystalline phases. Compared to bent-core models at the same $\gamma = 150°$ with $N_B = 4$ and 3, two main differences were found. First, in the lower volume ratios, the CC phase is destablized and occupies a very small phase region in the phase diagram (Fig. 24a). And at the lower temperatures, both chiral micelles (CM) and chiral columns (CC) aggregated to form achiral short layers (ASL). The ASL phase, shown in Fig. 25, is similar to the L phase in that both have layered structures, but the ASL phase forms at lower volume ratios with much larger spacing between layers.

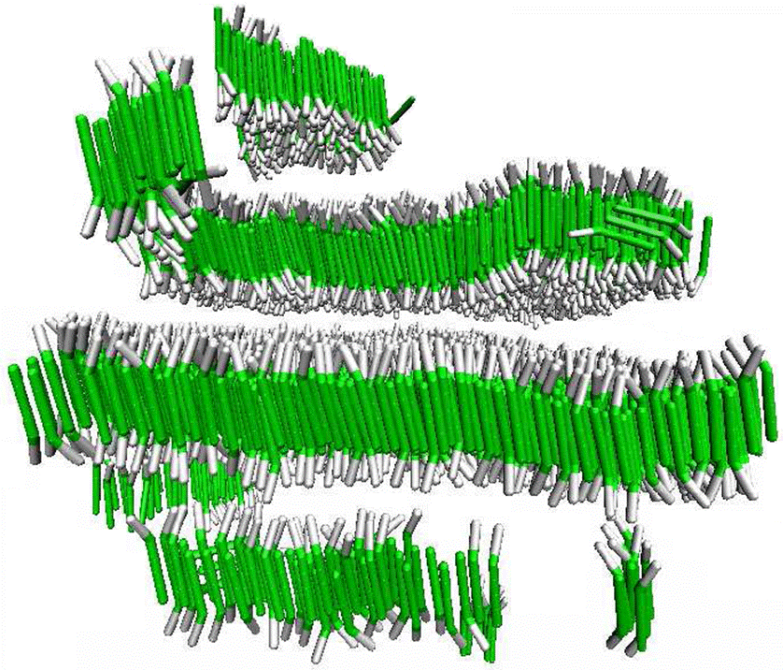

Figure 25: Simulation snapshots of the achiral short layers (ASL) phase from a system of $M = 3000$ molecules with $N_A = 5$, $N_B = 2$ and $\gamma = 150°$ at $\phi = 0.09$ and $1/T^* = 1.14$ in a NVT simulation.

It is posited that by decreasing the value of N_B, the steric effect caused by these particles

is alleviated and at low temperatures, chiral micelles or chiral columns can aggregate together to form layers to minimize the potential energy. Also because ϕ is low, all the layers are distributed randomly in the simulation box, which is different from the lamellar phase at the higher volume ratio where all layers are packed together. The second difference is that, at the same volume ratio, the phase transition temperatures for liquid crystalline phases for $N_B = 2$ are higher than those for $N_B = 4$ or 3, which is likely to be due to a packing effect, as described previously in Fig. 23.

At $\gamma = 120°$, six phases formed: namely the Iso, CM, CC, L, SmC and SmI phases (Figs. 20 and 24b). At lower ϕ, the CM ($\phi \leq 0.19$), CC ($0.09 \leq \phi \leq 0.29$) formed. At higher ϕ, the liquid crystalline phases formed including the SmC and SmI phases ($0.33 \leq \phi \leq 0.38$), but not SmA phase. And the L phase ($0.24 \leq \phi \leq 0.38$) lies in between. Two main differences are found between the bent-core molecules with $N_B = 3$ and $N_B = 2$. The first is that the CC phase started to form at lower ϕ, which may also be caused by a packing effect: by decreasing the WCA particles per molecule, the LJ particles can stack together more closely. The second is that the chiral micelles tend to aggregrated to form chiral columns at a lower volume ratio than in the case of $N_B = 3$ or 4.

At $\gamma = 90°$, only three phases formed. These are the Iso, SM and the SC phases (Figs. 20 and 24c). SM formed at lower volume ratios ($\phi < 0.16$), while SC formed at higher volume ratios ($0.12 < \phi \leq 0.36$). The phase diagram is shown in Fig. 24c, which is very similar to those of bent-core molecules with $N_B = 4$ in Fig. 17b and $N_B = 3$ in Fig. 22c. Compared to the bent-core molecules with $N_B = 4$ or $N_B = 3$, there are two main differences. The first is that the phase region for SM decreases, and disappears at the volume ratio $\phi = 0.16$, compared to $\phi = 0.23$ for both $N_B = 4$ and $N_B = 3$. The second is that the SC phase started to form at a lower volume ratio of 0.12, compared to the volume ratio of 0.15 for both $N_B = 4$ and $N_B = 3$. These two differences can also be interpreted as a packing effect. By decreasing the WCA particles per molecule, the steric effect is alleviated in the system and the staired micelles can aggregate together to form staired columns at lower volume ratios.

6.3.5 $N_A = 5$, $N_B = 1$ at $\gamma = 150°$, $120°$ and $90°$

The phase diagrams for model systems with $N_A = 5$ and $N_B = 1$ at different bending angles $\gamma = 150°$, $120°$ and $90°$, are shown in Figs. 26a-c, respectively.

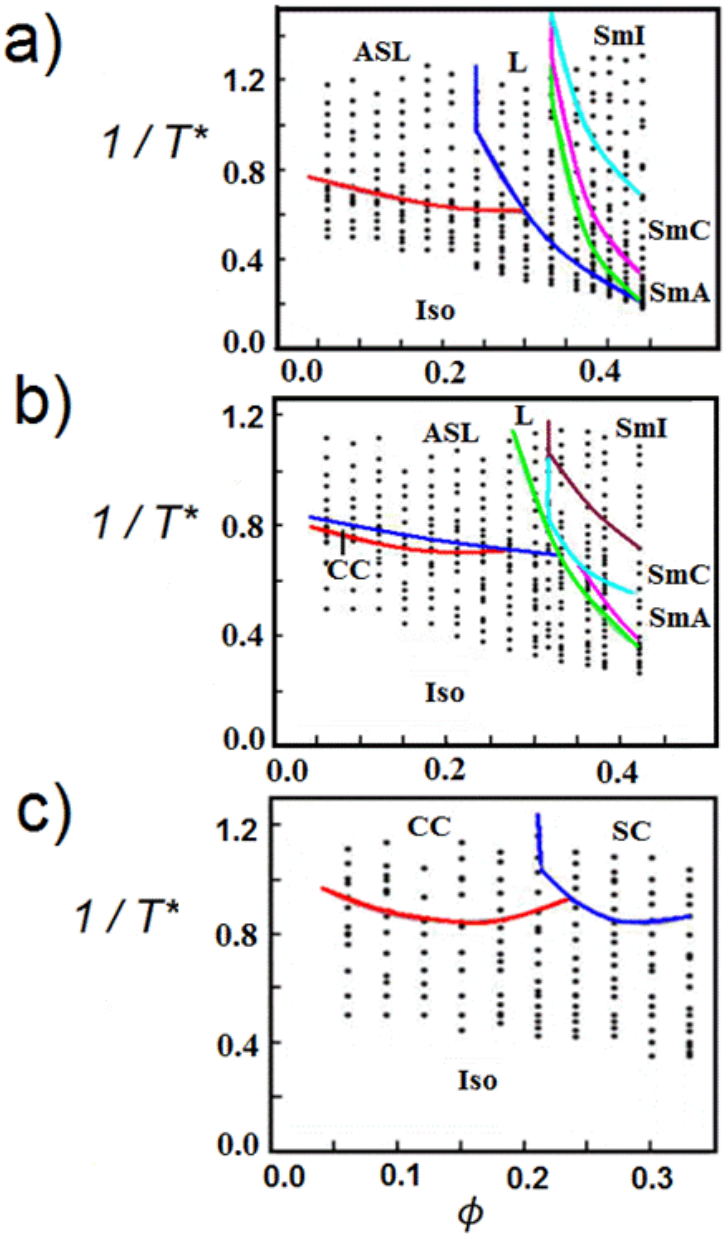

Figure 26: Phase diagram of bent-core molecules of $N_A = 5$ and $N_B = 1$ at (a) bending angle $\gamma = 150°$, (b) $\gamma = 120°$ and (c) $\gamma = 90°$ in the NVT simulations.

At $\gamma = 150°$, six phases formed including the Iso, ASL, L, SmA, SmC and SmI phases (Figs. 20 and 26a). At lower volume ratios ($\phi < 0.30$), the achiral short layers (ASL) formed. At higher volume ratios, the liquid crystalline phases developed, including not only the SmC and SmI phases, ($0.36 \leq \phi \leq 0.44$), but the SmA phase as well. In the intermediate region, the L phase forms ($0.24 \leq \phi \leq 0.44$). The significant change here is that the chiral micelles did not form at low volume ratios, and the N phase did not form at high volume ratios. This indicates that by decreasing N_B to one, the steric effect from the purely repulsive interactions decrease significantly and the LJ particles can stack together to directly form archiral short layers without forming micelles or columns first. The disappearance of the N phase may be caused by the low length-to-width ratio ϕ_{l-w}. As discussed in chapter 5, that nematic phase has been observed for hard spherocylinders with length-to-width ratios greater than $4.5 : 1$ and the region of nematic phase increases as the length-to-width ratio increases.[22] In the present case, due to the attractive LJ particles, the lowest length-to-width ratio of bent-core molecules for forming nematic phase is expected to be higher than $4.5 : 1$. The length-to-width ratio of a bent-core molecule ϕ_{l-w} is defined as

$$\phi_{l-w} = (N_A + N_B)\sin(\gamma/2) : 1 \tag{6.1}$$

Because the nematic phase disappears for $N_B = 1$, the lowest length-to-width ratio for bent-core molecules at $\gamma = 150°$ is expected to lie between 5.8 ($N_B = 1$) and 6.8 $N_B = 2$. The linear case ($\gamma = 180°$) with $N_A = 5$ and $N_B = 1$, for which $\phi_{l-w} = 6.0$, did not form the nematic phase. It should be noted that bent-core molecules made of pure LJ particles can also form the nematic phase. Based on Dewar and Camp's work[158], a symmetric bent-core model molecule made of seven LJ particles at a bending angle $\gamma = 160°$ can form a nematic phase, which disappears at $\gamma = 140°$. By using eq. (6.1), the lowest length-to-width ratio for bent-core molecules made of seven LJ particles are calculated to lie between 6.6 ($\gamma = 140°$) and 6.9 ($\gamma = 160°$).

At $\gamma = 120°$, seven phases formed. These are the Iso, CC, ASL, L, SmA, SmC and SmI phases (Figs. 20 and 26b). The CC ($\phi < 0.29$) and the ASL ($\phi < 0.30$) formed at lower volume ratios, while the liquid crystalline phases [the SmA, SmC and SmI ($0.315 \leq \phi \leq 0.42$)] formed at higher volume ratios. In between lies the L phase ($0.27 < \phi \leq 0.42$).

Compared to $N_B = 4$, 3, or 2, two points may be noted. First, the chiral micelles do not form here. Second, at low volume ratios, the chiral columns do form, but as the temperature decreases, the chiral columns start to aggregate to form achiral short layers. These two changes can be explained by a packing effect, as discussed in previous sections. A SmA phase is also found to form here, which is absent for model systems with $N_B = 4$, 3 or 2. This can also be explained by a packing effect. That is, by decreasing the WCA particles per molecule, the steric effect from the WCA particles can be decreased and results in the formation of an untilted SmA phase.

At $\gamma = 90°$, only three phases formed, namely the Iso, CC and ASL phases (Figs. 20 and 26c). At lower volume ratios ($\phi < 0.24$), the CC phase formed. At higher volume ratios ($0.21 \leq \phi \leq 0.33$), the ASL phase formed. Compared to $N_B = 4$, 3, or 2, a significant change here is the formation of the chiral column phase (CC). It is only in this system that the chiral features developed for $\gamma = 90°$. This indicates that by decreasing N_B, the steric effect from the small bending angle $\gamma = 90°$ decreases and the LJ particles can pack more closely to form chiral columns, instead of stair-like columns (see Fig. 19c). However, at volume ratio higher than 0.21, the steric effect becomes significant and the staired columns form instead.

6.3.6 Summary of phase diagrams

The results of phase diagrams are summarized in Fig. 20.

At low volume ratios, micelle phases formed. At $\gamma = 150°$ and 120°, chiral micelles (CM) and chiral columns (CC) developed, however, by decreasing the purely repulsive WCA particles per molecule, the chiral micelle phases (CM and CC) aggregated to form achiral short layers (ASL). At $\gamma = 90°$, staired micelles formed which lack chirality for most micelles, surprisingly, for bent-core molecules with $N_B = 1$, chirality is regained by forming chiral columns in the system.

At high volume ratios, liquid crystalline phases formed. At $\gamma = 150°$, four liquid crystalline phases formed including the N, SmA, SmC and SmI phases. At $\gamma = 120°$, when $N_B = 4$, no liquid crystalline phases formed, but by decreasing N_B, the liquid crystalline phases formed. For example, for $N_B = 3$ and 2, the SmC and SmI phases formed. And for

$N_B = 1$, all three smectic phases formed. At $\gamma = 90°$, staired micelles (SM) and staired columns (SC) formed.

At moderate volume ratios, the L phase formed at both $\gamma = 150°$ and $120°$, but not $\gamma = 90°$.

The phase transition temperatures for liquid crystalline phases at the same bending angle γ but with different N_B have also been compared. Decreasing the N_B has been found to increase transition temperatures. And for the systems with the same N_B but at different bending angles, the higher the bending angle, the higher the transition temperatures for liquid crystalline phases.

6.4 CONCLUSION

In this work the phase behavior of rigid achiral bent-core model systems has been studied by varying the bending angle γ and the arm length ratio of N_A / N_B by using molecular dynamics simulations in both the canonical ensemble and the isothermal-isobaric ensemble.

Eleven phases have formed in different model systems, namely the isotropic (Iso), chiral micelle (CM), chiral column (CC), staired micelle (SM), staired column (SC), achiral short layer (ASL), lamellar (L), nematic (N), smectic A (SmA), smectic C (SmC), and smectic I (SmI) phases. At low volume ratios ϕ, the micelle phases developed, of which there are five types of micelle phases including the CM, CC, SM, SC and ASL phases. At high volume ratios four liquid crystalline phases formed, including the N, SmA, SmC and SmI phases. Increasing the bending angle γ has been found to favor the formation of chiral phases and liquid crystalline phases. And decreasing the value of N_B results in the lower transition temperatures and higher volume ratios to form the liquid crystalline phases. Decreasing N_B has been found to offset the steric effect caused by the bending angle γ and effectively results in the formation of chiral phases and/or liquid crystalline phases at the smaller bending angles. These results show that chiral phases and liquid crystalline phases can be tuned by altering the bending angle γ and the arm length ratio N_A / N_B, and thus to provide the possibility of guiding experimentalists in synthesizing bent-core molecules with desired

phase behaviors.

7.0 AN ALL ATOM COMPUTER SIMULATION STUDY OF THE LIQUID CRYSTALLINE PHASE BEHAVIOR OF ALKENIC FLUOROTERPHENYLS

Manuscript in preparation

Yan, F.; Earl, D. J.

7.1 INTRODUCTION

In this chapter, the influence of regiospecific fluorine substitutions on the liquid crystal phases formed by di-, tri- and tetrafluoroterphenyls is studied by using molecular dynamics simulations in the isothermal-isobaric (NPT) ensemble at the all atom level. The choice of system is inspired by the experimental work of Gasowska *et al.*[1], where increasing substitution of hydrogen atoms with fluorine atoms in the aromatic ring groups of alkenic terphenyl molecules was found to destabilize the smectic phases that were observed for the difluoroterphenyl molecule. System sizes of 1500 molecules are employed in order to allow for the formation of at least three smectic layers in simulations, and these simulations are conducted from the isotropic phase to the liquid crystalline phases by using a simulated annealing method. The difluoroterphenyl system forms isotropic, nematic, smectic A and smectic C phases; the trifluoroterphenyl system forms isotropic, nematic and smectic C phases; and the tetrafluoroterphenyl system forms only isotropic and nematic phases. To our knowledge, these are the largest atomistic simulations of liquid crystal phase behavior, and demonstrate the formation of smectic phases from a more disordered state at the all atom level. These simulation results are also in good agreement with experiment[1], and show that small variations in molecular

structure can have a significant impact on liquid crystalline phase behavior and this impact can be theoretically predicted. Thus, this work provides a glimpse of the potential for designing new materials through computational modeling. The rest of the paper is arranged as follows: the computational model and the employed methods are described in section 7.2; the simulation results and their implications are discussed in section 7.3; and the conclusion is made in section 7.4.

7.2 COMPUTATIONAL DETAILS

The molecular structures and ab initio optimized geometries of the alkenic fluorinated terphenyls, di-, tri- and tetra-fluoroterphenyls are shown in Fig. 27.

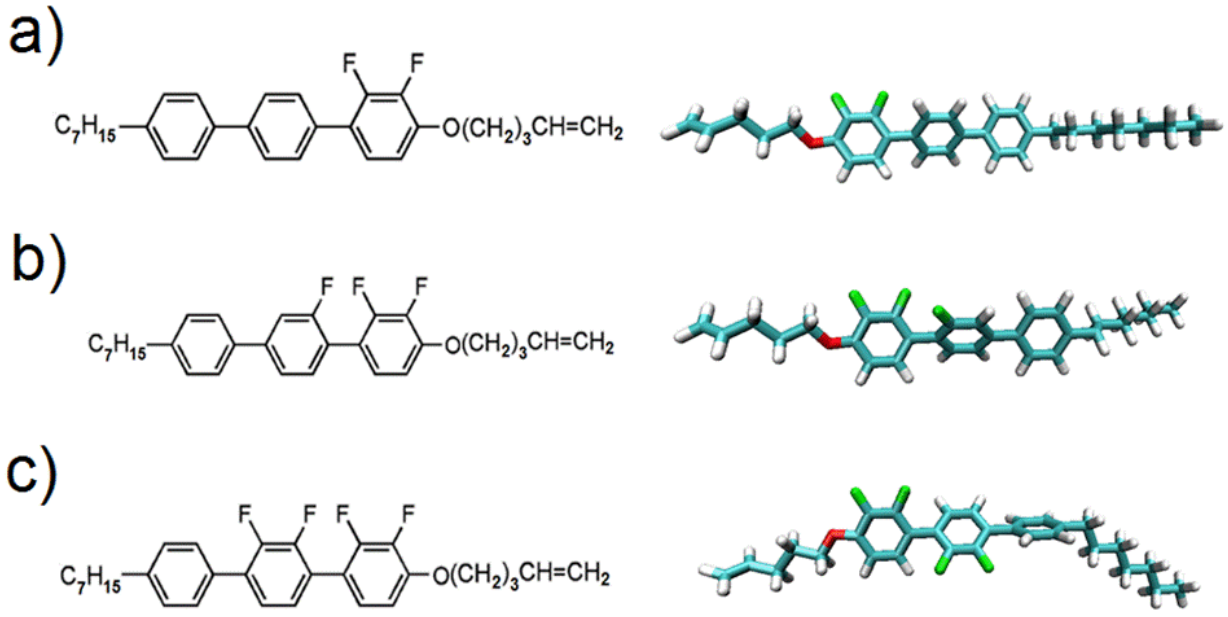

Figure 27: Molecular structures (Left) and ab-initio optimized geometries (Right) of (a) alkenic di-, (b) tri- and (c) tetra-fluoroterphenyls.

The optimized geometries were calculated by density functional theory at the B3LYP/6-31(d,p) level[7]. All the alkenic fluorinated terphenyls contain a terphenyl group at their

core, an n-heptyl side chain at one end of the core and a pent-4-enyloxy side chain at the other, with the only differences among them being the number and position of the fluorine substituents on the middle phenyl ring. Gasowska *et al.* recently investigated the phase behavior of this series of molecules experimentally and motivated this investigation[1].

All atom molecular dynamic simulations are conducted by using a parallel version of the Gromacs simulation code[163, 164, 165, 166]. A simulated annealing protocol is utilized to study the phase behavior as a function of temperature, at a fixed pressure of 1 atmosphere. The potential energy of the system is calculated using the liquid crystal force field (LCFF) of Wilson and co-workers[8]. The potential energy expression is given by:

$$\begin{aligned} U_{total} &= \sum_{angle} \frac{1}{2} K_\theta (\theta - \theta_{eq})^2 + \sum_{improper} V_\phi (1 + \cos(m\phi - \delta_0)) + \sum_{proper} \sum_{n=0}^{5} C_n (\cos(\phi - 180^\circ))^n \\ &+ \sum_{i<j} \left(\frac{q_i q_j}{r_{ij}} + 4\epsilon_{ij} \left[\left(\frac{\sigma_{ij}}{r_{ij}} \right)^{12} - \left(\frac{\sigma_{ij}}{r_{ij}} \right)^{6} \right] \right) f_{ij} \end{aligned} \tag{7.1}$$

where K_θ and V_ϕ are force constants for angle bending and improper torsional motion, respectively; m is the multiplicity and set at $m = 2$; δ_0 is the phase angle and set at $\delta_0 = 180^\circ$. C_n is the Rychaert-Bellemans force constant[167] for proper torsional motion; the nonbonded energy terms are represented by Coulomb and Lennard-Jones (LJ) potentials, where Lorentz-Bertelot rules are applied for the LJ parameters; the scaling factor $f_{i,j} = 0.5$ for 1,4 LJ nonbonded terms and $f_{i,j} = 1$ for all other nonbonded terms. As the force constants for dihedral angles betweeen the aromatic rings in di-, tri- and tetrafluoroterphenyls are not available in LCFF, the six-term Ryckaert-Bellemans parameters (see equation 1) are fitted to density functional theory calculations at the B3LYP/6-31(d,p) level[7]. Details of these fitting calculations will be discussed in section 7.3.

The LINear Constraint Solver (LINCS)[168] method is used to constrain all bonds, and a time step of 2 fs is utilized in the simulations. Long range electrostatic interactions are treated with the smooth particle mesh Ewald (SPME) method[169] with a 4th order PME and an Ewald convergence of 1×10^{-5}. A cut-off distance of 1.2 nm is used for short-range van der Waals interactions and real-space electrostatic interactions. All simulations are conducted in the isothermal-isobaric ensemble (NPT) at 1 atmosphere using a Nosé-Hoover thermostat[97, 98] and an isotropic Parrinello-Rahman barostat[170] with relaxation times

of 1 and 5 ps, respectively. Each simulation contains 1500 molecules for a total of 100500 atomic sites. The simulations are conducted as follows. Each simulation starts in a cubic box of 60.0 nm along each side with periodic boundary conditions employed. The systems are compressed quickly using a high pressure of 10000 bar at 50 K until they reach a density of approximately 0.70 g cm^{-3}. The systems are then heated up to 800 K for 5.5 ns, and become isotropic at equilibrium. Following this, each system is cooled using a simulated annealing procedure.

Fast annealing was performed for systems at temperaures above 600 K, which is significantly higher than experimental transition temperatures[1] from the isotropic to the nematic phase for difluoroterphenyls (436 K), trifluoroterphenyls (385 K) and tetrafluoroterphenyls (370 K). Systems were sequentially cooled from 800 K to 700 K and then to 600 K with 2 ns of cooling and 2 ns of equlilibration time for each 100 K interval. A slightly slower annealing was performed between 600 K and 500 K. In this range, 50 K temperature intervals were chosen with 3 ns of cooling and 3 ns of equilibration time for each interval. Below 500 K we employed temperature intervals of between 30 K and 10 K, until the systems became crystalline, with 4 or 5 ns of cooling time and 4 ns of equilibration time for each temperature interval.

Phase transition temperatures from the isotropic to nematic phase were determined as follows. From the annealing simulations an estimate of the transition temperature was obtained by monitoring the energy and volume of the system, the nematic order parameter, and through visualization. The annealing procedure is expected to determine a transition temperature that was slightly too low, due to the temperature intervals used in the annealing procedure. Therefore, a series of molecular dynamics simulations were performed at fixed temperatures within 20 K of the estimated temperature, with 2 to 5 K temperature intervals between simulations, at 1 atmosphere in the NPT ensemble. Each of these simulations was carried out until the nematic order parameter did not drift significantly, and then continued for a further 5 ns for equilibration. Then transition temperature of the isotropic to nematic phase was determined by following the method utilized by Berardi *et al.*[75] by fitting the nematic order parameters to the Haller equation[6].

Other phase transitions were identified in a similar way, with a number of fixed tem-

perature simulations performed close to the estimated temperatures from the annealing run. Liquid crystal phases were characterized and identified using a variety of techniques including the calculation of radial and pair distribution functions, the calculation of tilt with respect to the orientational order parameter, and through visualization methods. Total simulation times were on the order of 100 ns.

7.3 RESULTS AND DISCUSSION

Shown in Fig. 28 are snapshots of the isotropic (Iso), nematic (N), smectic A (SmA) and smectic C (SmC) phases formed by difluoroterphenyls at a range of temperatures and at a constant pressure of 1 atmosphere from the simulations. The time dependence of the nematic order parameter S_2 for the simulated annealing simulations was calculated. S_2 is defined as:

$$S_2 = \frac{1}{2} < 3\cos^2\theta - 1 > \tag{7.2}$$

where θ is the angle between the molecular axis and the system director. There are several options for choosing the molecular axis, and the eigenvector corresponding to the largest eigenvalue of the moment of inertia tensor for the whole molecule was chosen. In order to investigate the influence of the flexible chain on the stabilization of the smectic layers, the moment of inertia tensor for the aromatic part of the molecules was chosen for comparison. Fig. 29 shows the time evolution of the nematic order parameter S_2 during the annealing simulation and shows that the nematic order parameter calculated from the moment of inertia tensor for the whole molecule is higher than that calculated from only the rigid aromatic part of the molecules, indicating that the flexible chains effectively increase the order of the smectic layers, similar to the simulation results for a nematic mixture E7[82], which contains four components: 4-cyano-4′-*n*-pentyl-biphenyl (5CB), 4-cyano-4′-*n*-heptyl-biphenyl (7CB), 4-cyano-4′-*n*-octyloxy-biphenyl (80CB) and 4-cyano-4″-*n*-pentyl-*p*-terphenyl (5CT).

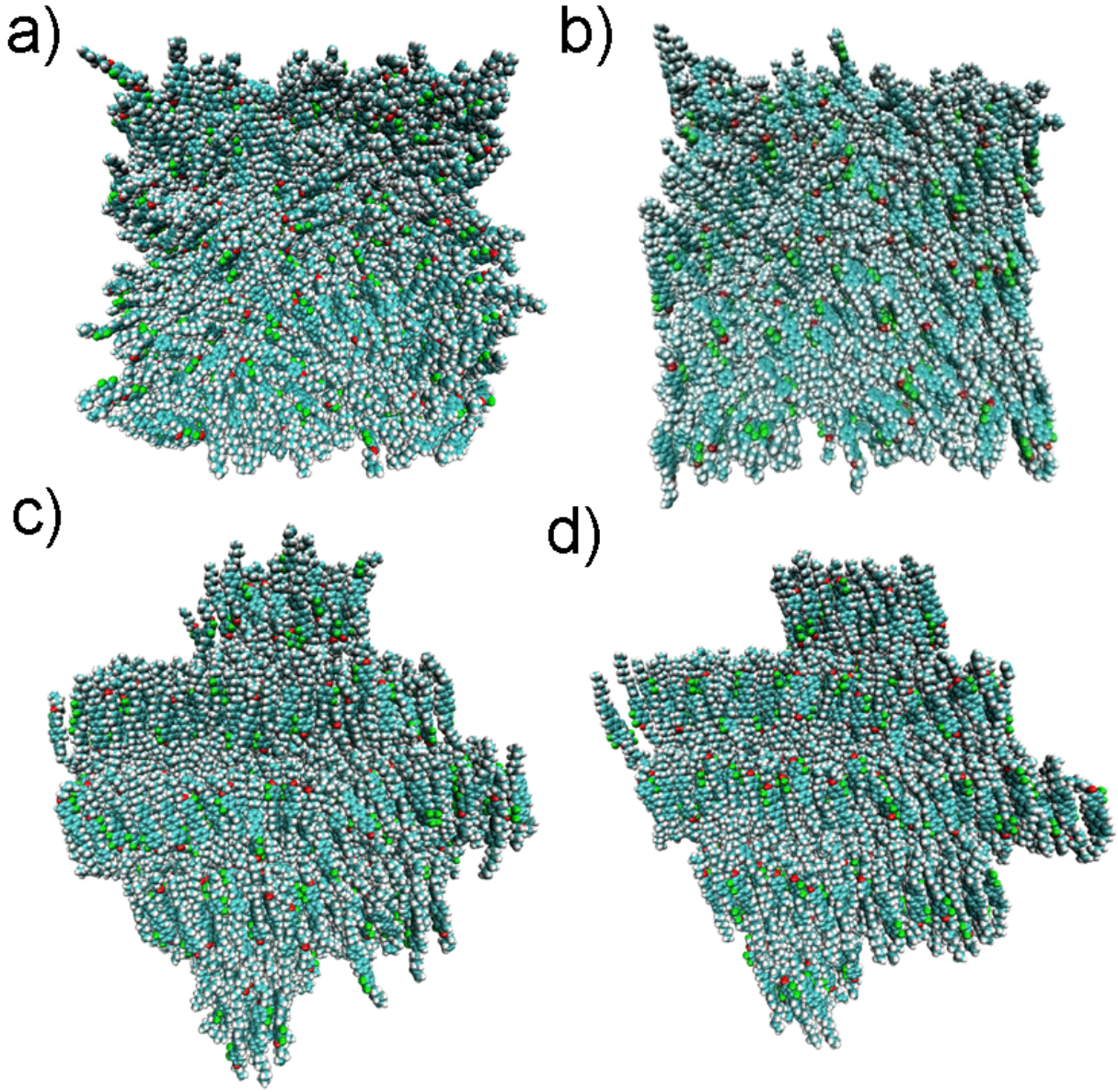

Figure 28: All phases formed by the alkenic di-fluoroterphenyls. Snapshots taken from our simulations of (a) an isotropic phase (Iso), (b) a nematic phase (N), (c) a smectic A phase (SmA), (d) a smectic C phase (SmC).

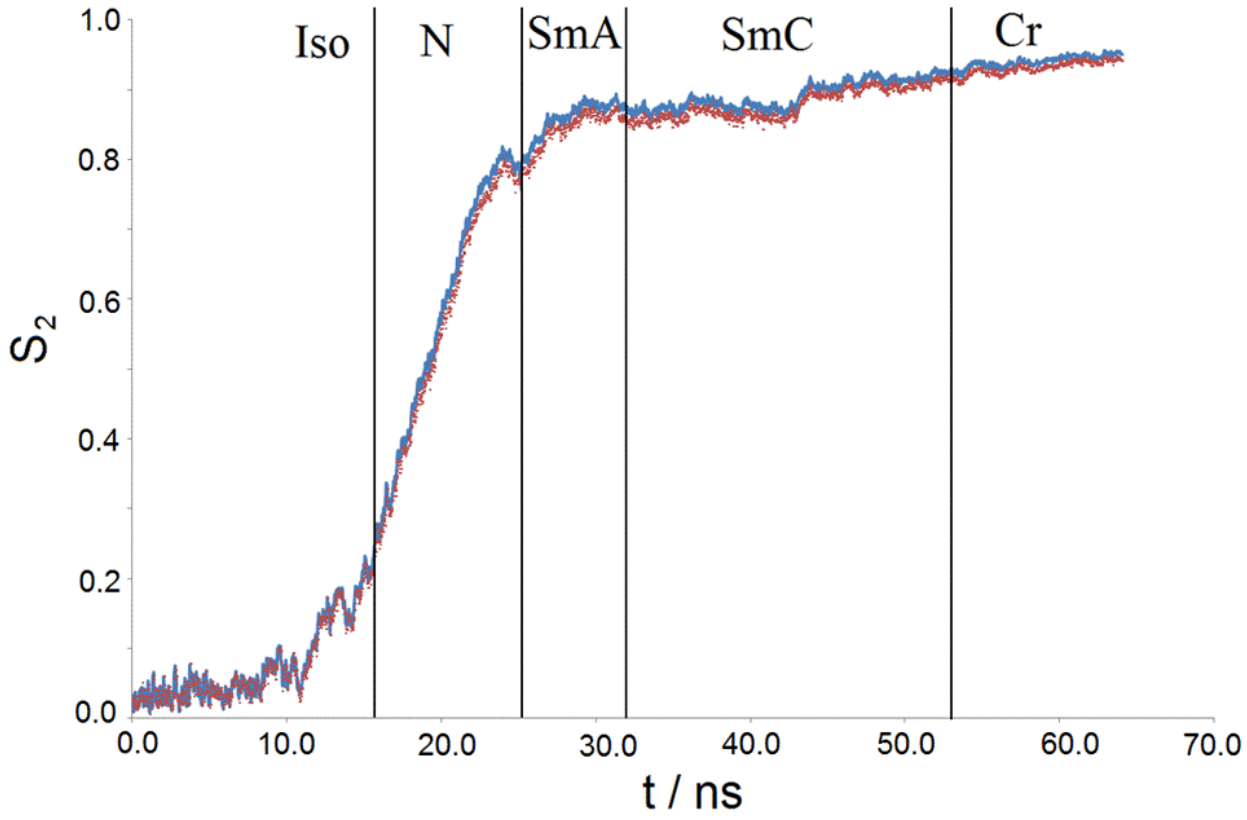

Figure 29: The time dependence of nematic order parameter S_2 by simulated annealing using molecular dynamics simulation for difluoroterphenyls in the isothermal-isobaric ensemble (NPT). The system started with an isotropic phase at $T = 800$ K and was cooled down to form crystal phase at $T = 420$ K. Four phase transitions occur for the process, these are isotropic to nematic (Iso-N), nematic to smectic A (N-SmA), smectic A to smectic C (SmA-SmC) and smectic C to crystal (SmC-Cr). The blue bold line represents S_2 calculated from the inertia tensor for the whole molecule and the red dotted line represents S_2 calculated from the inertia tensor for the aromatic part of the molecules.

The structures and phases formed by the difluoroterphenyl system are described as follows. At temperatures from $T = 509$ K to $T = 487$ K the molecules self-assemble to form a nematic phase (See Fig. 28b). The nematic phase has orientational order along the system director, but the observed absence of layer formation indicates no positional order. Following a number of fixed temperature simulations in the interval over which the phase transition was observed, the temperature dependence of the nematic order parameter was fitted to the Haller equation[6],

$$< S_2 >_{Haller} \quad = \quad (1- < S_2 >_{iso})(1 - \frac{T}{T_{NI}})^{\beta} + < S_2 >_{iso}, \quad T \leq T_{NI} \tag{7.3}$$

where β is the critical exponent for the $N - I$ transition. T_{NI} was chosen as the smallest of the temperatures with $< S_2 > \leq 0.25$. $< S_2 >_{iso}$ was calculated by averaging all $< S_2 >$ values corresponding to $T \geq T_{NI}$. The fitting curve is shown in Fig. 30.

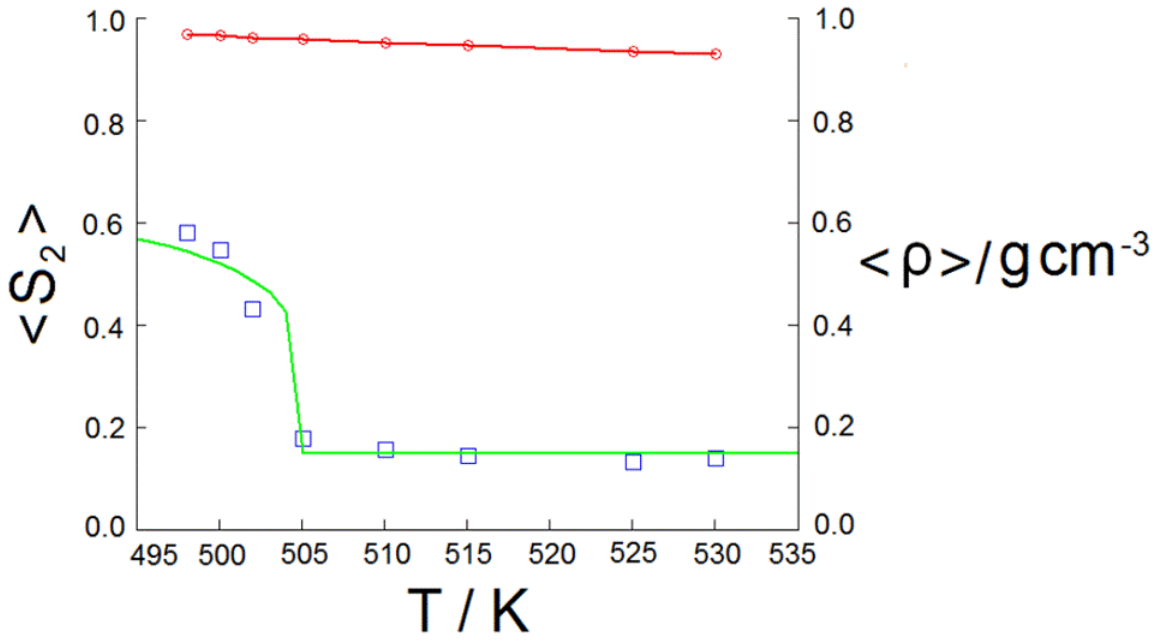

Figure 30: The temperature dependence of the average nematic order parameter $< S_2 >$ (blue boxes) and Haller fit[6] (green line, see eq. (7.3)), and the average density (red circled line) for difluoroterphenlys.

The value for the critical exponent β is 0.195 and close to $\beta = 0.2$, which yields a satisfactory fit[171] and T_{NI} was calculated to be 509 K. It is observed that the phase transition temperature in the simulation is 73 K higher than the experimental value[1], and that the nematic phase is stable over a larger temperature range than in the experiment, where the nematic phase is only stable over a 5 K region. The reason for this discrepancy may be caused by inaccuracies in the force field, the system size or the annealing speed utilized. We also calculated the average density as a function of temperature, and found that the density decreased linearly with increasing temperature, similar to the nematic system in Berardi *et al.*[75], indicating a NI transition.

At lower temperatures smectic phases and a crystal phase formed: smectic A (SmA), smectic C (SmC) and crystal (Cr). The phase transition from the nematic to the smectic A phase was monitored by observing smectic layer formation which was performed by visualization[91], and through the calculation of radial distribution functions (RDFs). The nematic phase is more liquid-like than the smectic phases, as demonstrated in the radial distribution function, $g(r)$, in Fig. 31a, which shows a first peak at a distance between 0.52 and 0.53 nm for all phases, with the intensity increasing from the nematic to smectic phases, and which is most intense in the crystal phase. A second peak at a distance between 0.96 and 0.98 nm is almost indistinguishable for the nematic phase, but is shown clearly for the smectic phases. In the crystal phase, a fine structure appears in the long range oscillations. The smectic A phase is characterized by untilted layers (see Fig. 28c) and no long range order within the layer. Decreasing the temperature results in the formation of a smectic C phase with tilted layers and no long-range positional ordering within the layers (see Fig. 28d). A further reduction in the temperature results in the formation of a crystal phase which, in addition to having a tilted layer structure, is characterized by local hexagonal ordering along with an in-layer tilt towards the hexagonal apex.

In order to characterize the smectic layer structures, The longitudinal distribution function, $g_{\parallel}(r)$, was calculated and shown in Fig. 31b. There are periodic peaks indicating order along the layer normal. In the smectic A phase, the oscillatory peaks are significant, indicating ordered layer packing. The periodic peaks become both sharper and more intense in the smectic C and the crystal phases. The average separation between the peaks can be used

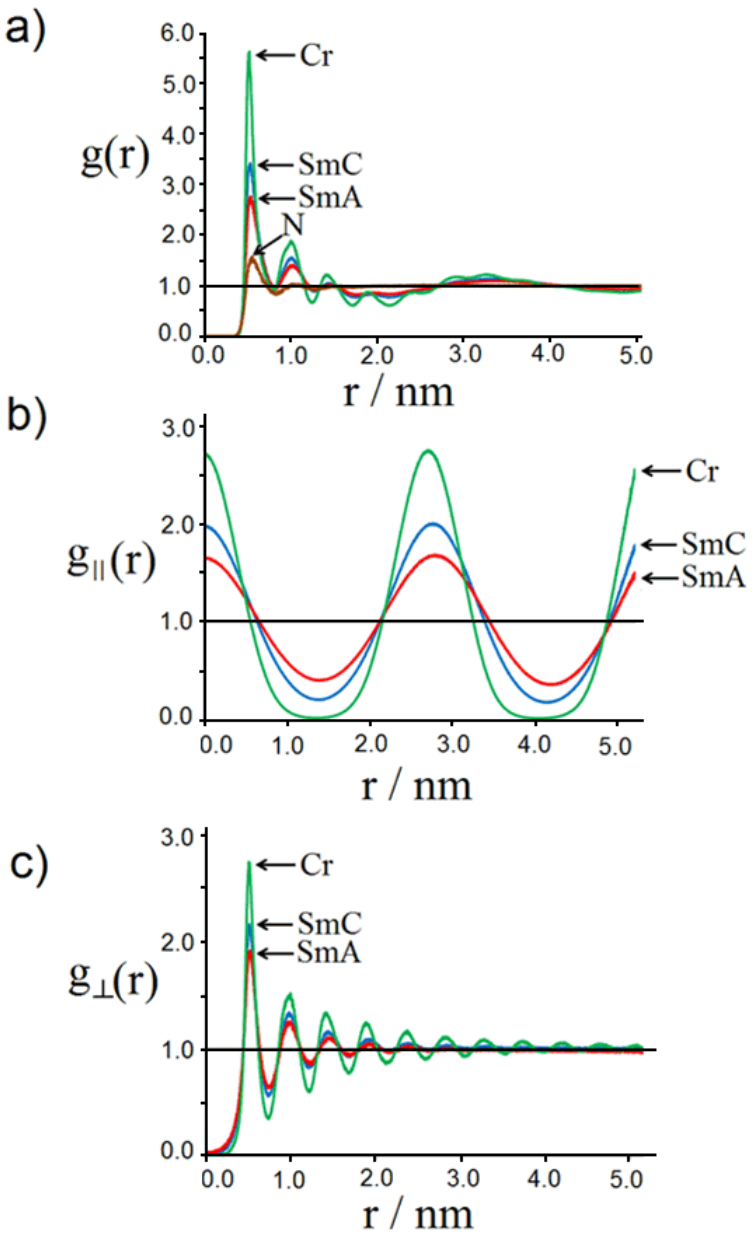

Figure 31: (a) The radial distribution function, $g(r)$, calculated with respect to the centre atom which is closest to the molecular centre of mass of each molecule, for 1500 difluoroterphenyls at 1 atomsphere. (b) The longitudinal distribution function with relative to the system layer normal, $g_{\parallel}(r)$, for a system of 1500 difluoroterphenyls at 1 atomsphere. (c) The in-plane distribution function, $g_{\perp}(r)$ with relative to the system layer normal, for a system of 1500 difluoroterphenlys at 1 atomsphere. The distribution functions are shown for the nematic (brown), smectic A (red), smectic C (blue), and smectic I (green) phases.

to determine the layer spacing, and are calculated as 2.72 ± 0.01 nm, 2.69 ± 0.01 nm, and 2.67 ± 0.01 nm for the smectic A, smectic C and crystal phases respectively, which is comparable to the molecular length of 2.75 nm. To explore the structure within each smectic layer, the in-plane distribution function, $g_{\perp}(r)$, was calculated and shown in Fig. 31c. In both the smectic A and smectic C phases the structure within the layer is clearly liquid like, and the in-plane distribution function shows no long range structure. In the crystal phase, there is hexagonal ordering and the in-plane order extends to large distances with a fine structure evident in the long range peaks. The first peak appears at a distance of 0.502 nm, and the separation distance between the peaks constituting this fine structure is approximately 0.45 nm (Fig. 31b), which is about $1/2^{\frac{1}{6}}$ nm of the distance relative to the first peak, and can be attributed to the hexagonal order within the layer. Because of the hexagonal order and the long range oscillations in the in-plane distribution function, this may be a deformed or SmI or Crystal J phase. The average tilt angle relative to the layer normal in each of the smectic phases was also measured. The tilt angle is temperature dependent and varies from $4^{\circ} - 14^{\circ}$ in the smectic C phase to approximately 16.5° in the crystal phase. The experimental tilt angle for pure difluoroterphenyls in smectic C and crystal phases are not avaiblable to us in literature, however, the tilt angle for difluoroterphenyls doped with 10 $wt\%$ BE8OF2N is available and has a maximum tilt angle of 17.5°[1], which is close to the result here.

In order to investigate whether molecular simulation is capable of predicting the large scale phase behaviour changes that accompany only small changes in the chemical structure in this series of molecules, molecular dynamics simulations of tri- and tetrafluoroterphenyls were also performed (see Figs. 27b and 27c) by using the same simulation protocol as described for the difluoroterphenyl system. The phases exhibited in the trifluoroterphenyls are isotropic, nematic, smectic C and crystal phases, and in the tetrafluoroterphenyls are isotropic, nematic and crystal phases. This is consistent with experimental observations[1].

In order to understand the different phase behaviours of di-, tri- and tetrafluoroterphenyls, the fluoro substitution effect on the dihedral angles between the phenyl rings of di-, tri- and tetrafluoroterphenyls was studied.

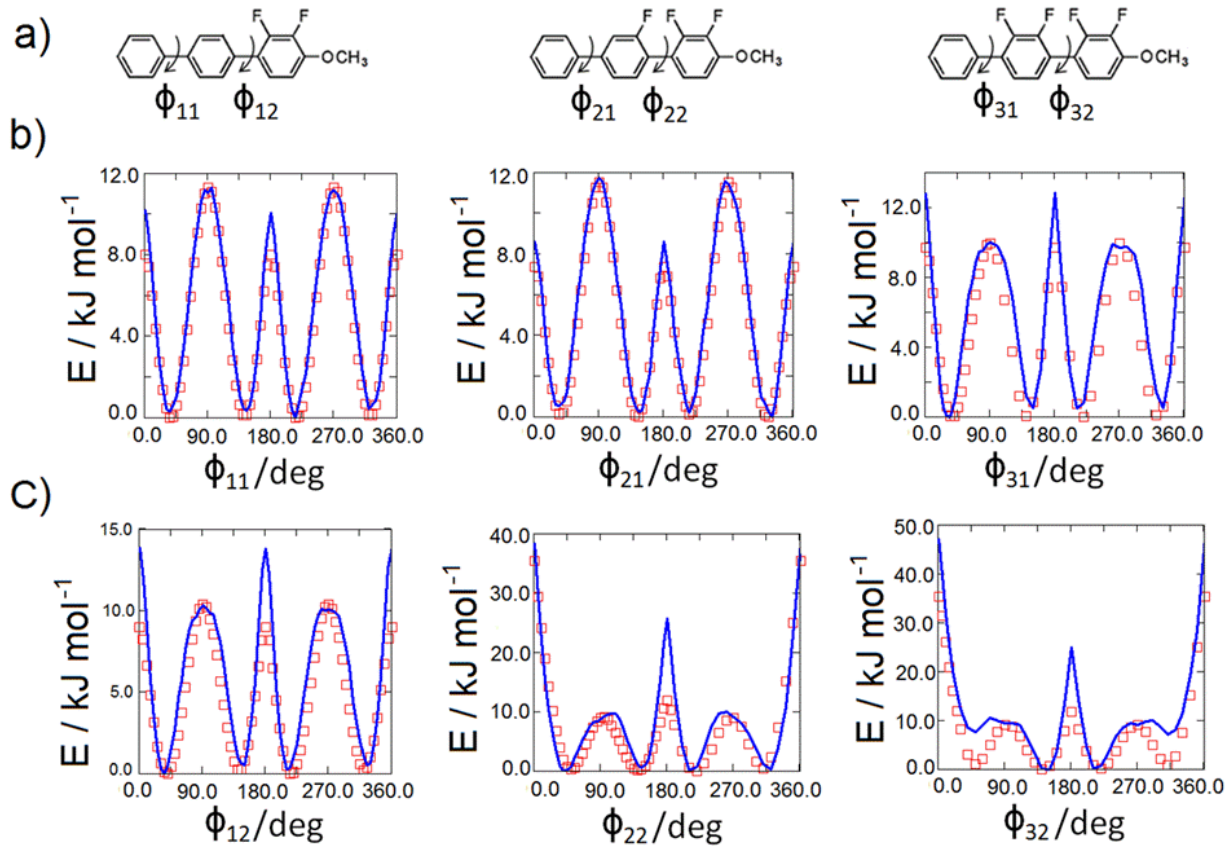

Figure 32: (a) The definition of ϕ_{11} and ϕ_{12} in difluoroterphenyl, ϕ_{21} and ϕ_{22} in trifluoroterphenyl, and ϕ_{31} and ϕ_{32} in tetrafluoroterphenyl. (b) The dihedral angle potential distributions of ϕ_{11}, ϕ_{21} and ϕ_{31}. (c) The dihedral angle potential distributions of ϕ_{12}, ϕ_{22} and ϕ_{32}. Both ab initio calculations and the fitting results are shown, where ab initio calculations are shown in red squares, and fitting curves are shown in blue line.

As shown in Fig. 32a, in difluoroterphenyl, ϕ_{11} is defined as the dihedral angle between the terminal phenyl ring with no fluoro substituents and the middle phenyl ring, and ϕ_{12} the dihedral angle between the middle phenyl ring and the terminal phenyl ring with two fluoro substituents.

ϕ_{21} and ϕ_{22} in trifluoroterphenyl, and ϕ_{31} and ϕ_{32} in tetrafluoroterphenyl are defined in the same way. Figs. 32b and 32c show the dihedral angle potential distribution for these six dihedral angles. Fig. 32b shows that the fluoro substituents have a small effect on ϕ_{21} and ϕ_{31}, in comparison with ϕ_{11}. For example, all the dihedral angles have the potential minimum located at 35°, 145°, 215° and 325°; and have similar potential barriers at 0°, 90°, 180° and 270°. The potential barriers at 0° and 180° for ϕ_{11}, ϕ_{21} and ϕ_{31} are 8.0, 7.3 and 9.7 kJ mol^{-1}, respectively; at 90° and 270° are 11.3, 11.7 and 10.0 kJ mol^{-1}, respectively. In contrast, Fig. 32c shows that the fluoro substitution has a strong effect on the dihedral angles of ϕ_{22} and ϕ_{32}. ϕ_{12}, ϕ_{22} and ϕ_{32} have the same potential minima located at 45°, 145°, 215° and 315°, whereas they have different potential energy barriers at 0°, 90°, 180° and 270°. The most significant change happens at 0°, where the potential barrier for ϕ_{12} is 8.9 kJ mol^{-1}, but increases to 35.4 kJ mol^{-1} for ϕ_{22} and ϕ_{32}. This significant increase may be caused by two factors. The first is the stronger steric effect arising from the replacement of the small hydrogen by a large fluoro substituent, where the van der Waals radii[172] of hydrogen and fluorine are 0.120 nm and 0.147 nm, respectively. The second is the stronger electrostatic repulsion for the fluoro substituent than the hydrogen substituent, which is caused by the higher absolute charge of fluorine (-0.246)[8] than that of hydrogen (-0.115)[8]. Other potential barriers at 90°, 180° and 270° are not significantly affected by the fluorine substitution, as shown in Fig. 32c (note the scale difference). The reason may be that the steric impact and the Coulomb repulsions are much weaker. Thus, it is clear that the specific fluorine substitution mainly changes the dihedral angle potentials of ϕ_{12}, ϕ_{22} and ϕ_{32}.

To further investigate the effect of the fluorine substitution, the dihedral angle distributions of ϕ_{12} in difluoroterphenyls, ϕ_{22} in trifluoroterphenyls and ϕ_{32} in tetrafluoroterphenyls were calculated and shown in Fig. 33.

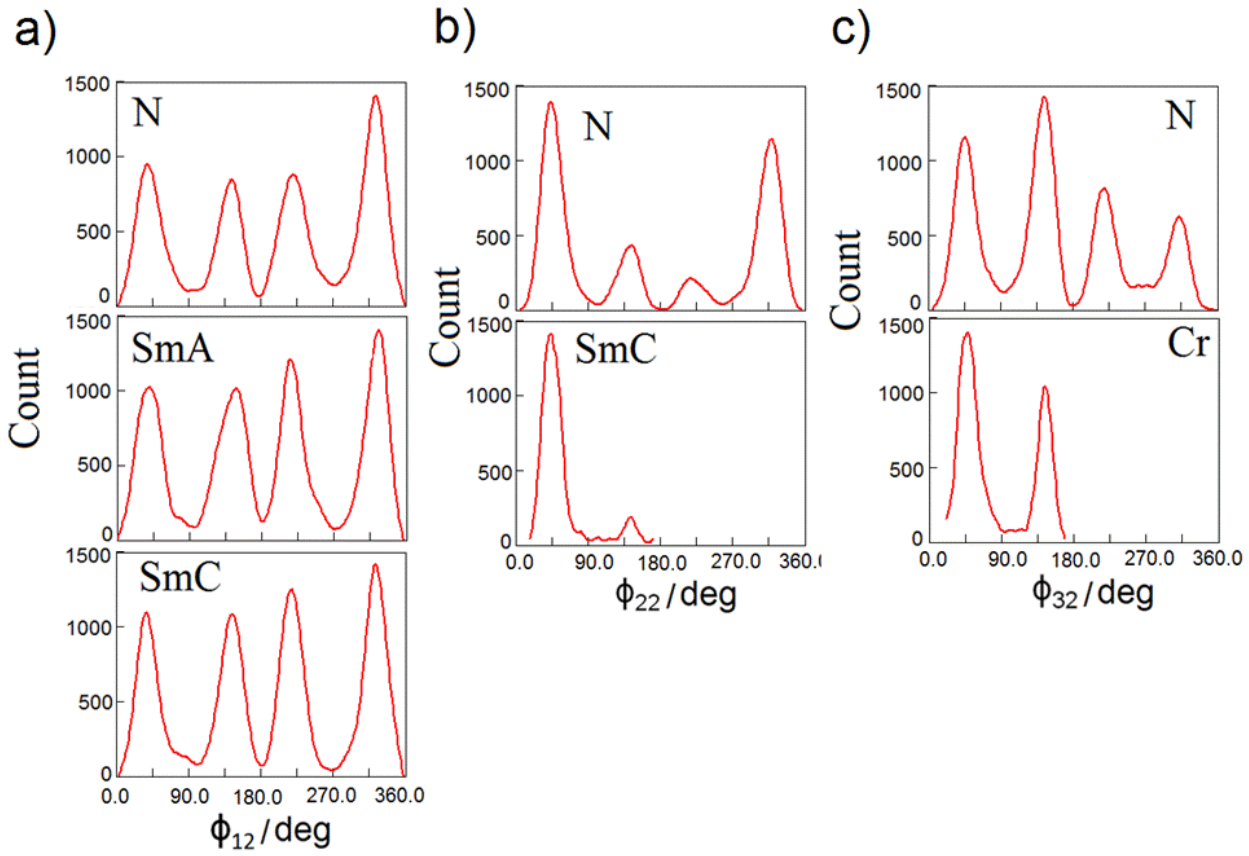

Figure 33: Dihedral angle distributions for (a) ϕ_{12} in difluoroterphenyls, (b) ϕ_{22} in trifluoroterphenyls, (c) ϕ_{32} in tetrafluoroterphenyls. All distributions were calculated based on the trajectories of molecular dynamics simulations of di- and tri- and tetrafluoroterpnenyls. Note the scales of count in different distributions are different.

Fig. 33a shows the dihedral angle distributions of ϕ_{12} in the N, SmA and SmC phases. The distributions are quite similar in all the three phases, where ϕ_{12} is evenly populated at 45°, 145°, 215° and 315°, corresponding to the respective dihedral angle potential minima of ϕ_{12}. Fig. 33b shows the dihedral angle distributions of ϕ_{22} in the N and SmC phases, which are markedly different from the corresponding ones of ϕ_{12}. The populations at 45° and 315° are much higher than those at 145° and 215°, indicating that the fluorine substituents preferentially lie on the same side of the molecule (see Fig. 34a), which is in good agreement with the result of Gasowska *et al.*[1].

Based on their experiment, the fluorine substituents tend to lie on the same side to

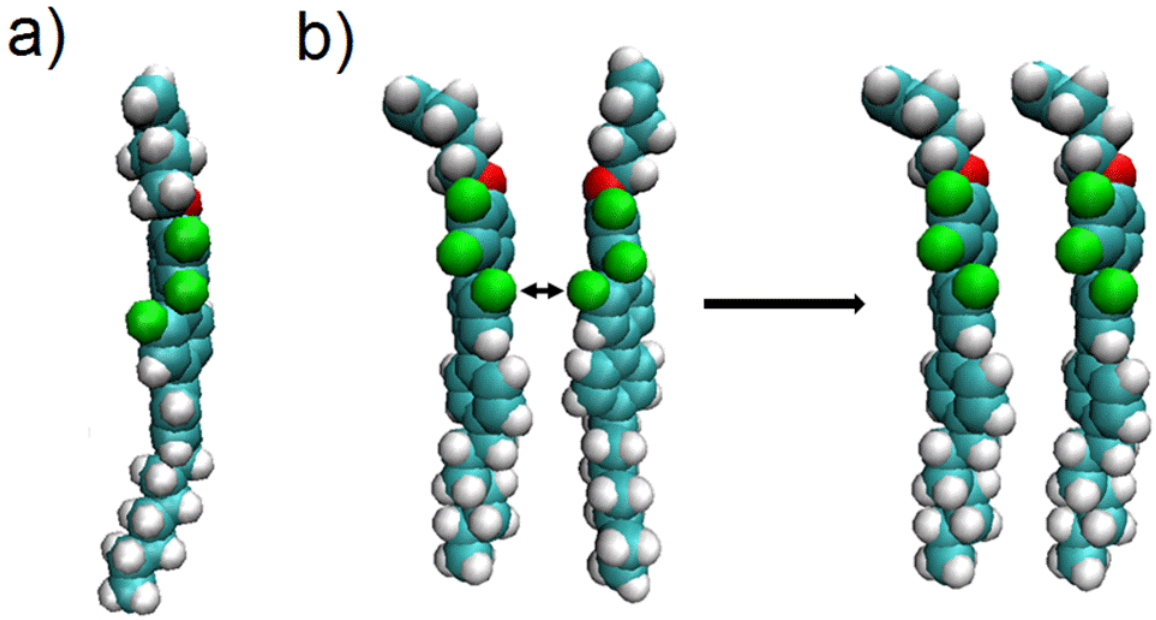

Figure 34: (a) A trifluoroterphenyl molecule is taken from a nematic phase of trifluoroterphenyls, showing that all three fluoro substituents lie on the same side of a trifluoroterphenyl molecule. (b) Suggested mechanism for the preferred configuration (right) for two parallel trifluoroterpheyls.

maximize the fluorine dipolar interactions[1]. Interestingly, in the SmC phase,the highest population is still at 45°, with a small population at 145°; however, there is no population for ϕ_{22} higher than 180°. This zero dihedral angle distribution may be caused by a packing effect, as suggested by Fig. 34b. In Fig. 34b, to minimize the effect of steric effect and Coulomb repulsions from the fluorines from nearby different molecules, one molecule has to rotate to the other side and make the dihedral angle to have the same sign as the other one. Moreover, this packing effect is more significant in the SmC phase than in the N phase, in order to form the smectic layers. It is also posited that this packing effect may cause the disappearance of the SmA phase for the trifluoroterphenyl system.

For tetrafluoroterphenyls, Fig. 33c shows dihedral angle distribution of ϕ_{32}. In the N phase, the populations show peaks at 45°, 145°, 215° and 315°, where the highest population

is at 145°. This seems to contradict the previous discussion of ϕ_{22} and the experimental result[1] that the fluorine substituents preferentially lie on the same side. However, this inconsistency may be caused by an over-fit of ϕ_{32} at 45° and 315°, as shown in Fig. 32c. Fig. 33c also shows the dihedral angle distribution of ϕ_{32} in the Cr phase. As for the SmC phase for ϕ_{22}, no population is found at ϕ_{32} higher than 180°. The disappearance of the SmC phase in tetrafluoroterphenyl may be caused by a packing effect; compared to trifluoroterphenyl, adding one more fluorine substituent significantly increases the steric and Coulomb repulsions resulting in the failure to form stable smectic layers.

Following the same data analysis routine for calculating the phase transition temperatures, the phase sequence diagram (Fig. 35) was constructed for all three fluoroterphenyls, in both simulations and experiments[1]. As shown in Fig. 35, the phase transition temperatures for difluoroterphenyls in experiments and simulations are: T_{NI} = 436 K (exp.) vs. 509 K (sim.) (isotropic to nematic), with a temperature difference of 73 K; T_{N_SmA} = 431 K (exp.) vs. 487 K (sim.) (nematic to smectic A), with a temperature difference of 56 K; T_{SmA_SmC} = 414 K (exp.) vs. 475 K (sim.) (smectic A to smectic C), with a temperature difference of 61 K; and T_{SmC_Cr} = 371 K (exp.) vs. 420 K (sim.) (smectic C to crystal), with a temperature difference of 49 K. In trifluoroterphenyls, the phase transition temperatures in experiments and simulations are: T_{NI} = 385 K (exp.) vs. 470 K (sim.), with a temperature difference of 85 K; T_{N_SmC} = 343 K (exp.) vs. 415 K (sim.), with a temperature difference of 72 K; and T_{SmC_Cr} = 304 K (exp.) vs. 370 K (sim.), with a temperature difference of 66 K. In tetrafluoroterphenyls, the phase transition temperatures in experiments and simulations are: T_{NI} = 370 K (exp.) vs. 465 K (sim.), with a temperature difference of 95 K; and T_{N_Cr} = 338 K (exp.) vs. 410 K (sim.), with a temperature difference of 72 K.

Thus, all phase transitions in the simulations have higher transition temperatures than observed experimentally, which has also been observed in atomistic simulations for other liquid crystal systems and biomolecular systems[173, 174, 175, 176]. For example, Kuprusevicius *et al.*[174] used atomistic molecular dynamics simulation to study the EPR spectra of 4-cyano-4′-n-pentylbiphenyl (5CB) with a doped spin probe by employing the LCFF force field[8] and found that the nematic-isotropic (NI) transition temperature in simulations is 75 K higher than that in experiment. McDonald *et al.*[173] used a united atom model atomistic

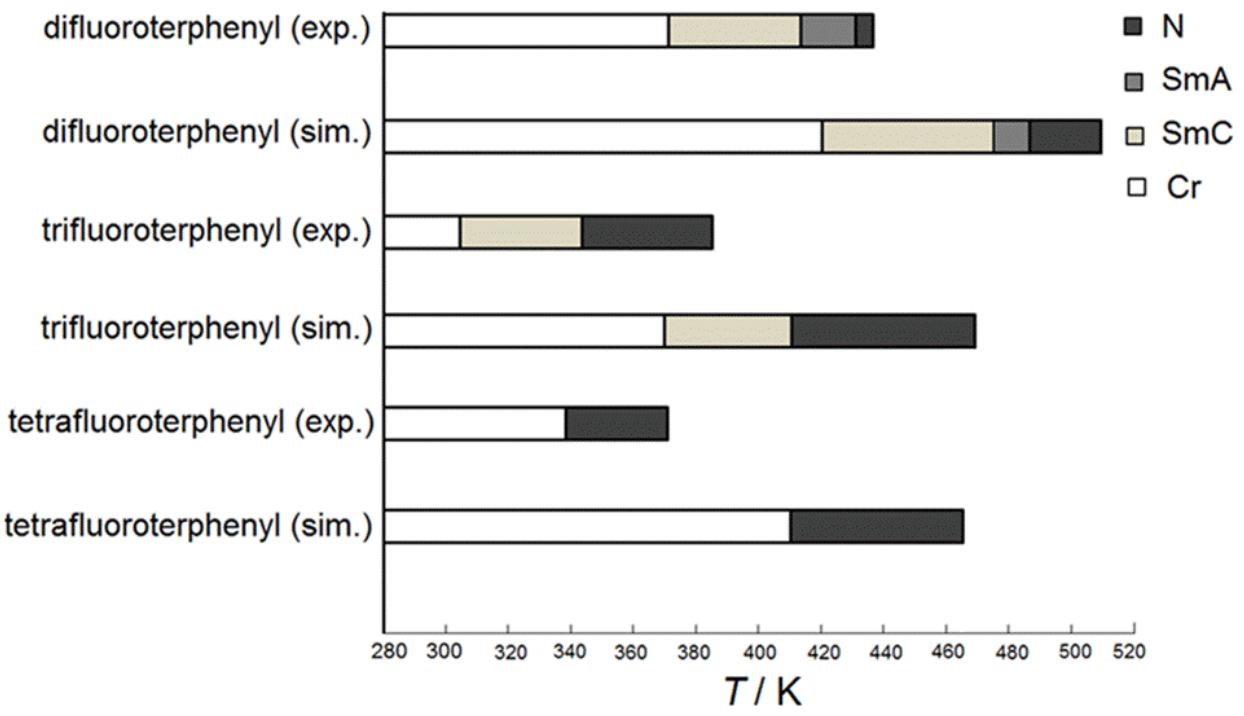

Figure 35: Phase sequences diagram for di-, tri- and tetrafluoroterpheyls in both simulations and experiments[1]. "exp." stands for "experiment" and "sim." stands for "simulation".

molecular dynamics simulation to study the phase behavior of 4-n-octyl-4′-cyanobiphenyl (8CB) by employing the Amber united-atom force field[120] and found the NI transition temperature are $70-85$ K higher than that in experiment. Zhou[175] used atomistic molecular dynamics simulation to study the Trp-cage folding in explicit water by employing OPLS-AA force field[81] and found that the melting transition temperature in simulation is 125 K higher than that in experiment. Pitera[176] used atomistic molecular dynamics simulation to study the Trp-cage folding in implicit water by employing the AMBER94 force field[177] and the GBSA continuum solvent model[178] and found that the melting transition temperature in simulations is 85 K higher than that in experiment. Thus, the failure to predict phase transition temperatures in atomistic molecular dynamics simulations appears to be common, and may be because most modern force fields have been parameterized at

room temperature[175], and do not accurately represent systems far from 300 K. It indicates that the force field we employed here still needs to be improved to provide a more accurate prediction of phase transition temperatures.

The temperature regions over which the different phases are stable have also been determined. In the trifluoroterphenyls, the temperature region for the nematic phase is 42 K compared to 55 K in the simulation; for the smectic C phase, the region is 39 K in experiment compared to 45 K in the simulation. In tetrafluoroterphenyls, the temperature region for the nematic phase is 32 K in experiment compared to 55 K in the simulation. In difluoroterphenyls, the temperature region for the nematic phase is 5 K in experiment compared to 22 K in the simulation; the temperature region for the smectic A phase is 17 K in experiment compared to 12 K in simulation; the temperature region for the smectic C phase is 43 K in experiment compared to 55 K in simulation. Thus, although there is a discrepancy betweeen the experimental and simulation phase transition temperatures, the predicted temperature region of stability for different phases are well matched, especially for tri- and tetrafluoroterphenyls (see in Fig. 35). These results show that the method employed here is able to correctly reproduce the experimentally observed phases formed, and give reasonable predictions of the temperature range over which the phases are stable.

7.4 CONCLUSION

In this chapter the effect of fluoro substituents on the phase behaviour of di-, tri- and tetrafluoroterphenyls has been studied by using molecular dynamics simulations in the *NPT* ensemble at a fully atomistic level. The fluorine substitution on phenyl rings has been found to affect smectic layer formation, in excellent agreement with experiment[1]. As the result that small variations in molecular structure can dramatically change the phase behaviour of liquid crystal molecules has been reproduced in the simulation, it is believed that in the future atomistic simulation will be capable of testing, screening and designing new molecular materials with targeted phase behaviours.

8.0 ATOMISTIC SIMULATIONS OF LIQUID CRYSTAL MIXTURES OF ALKOXY SUBSTITUTED PHENYLPYRIMIDINES 2PHP AND PHP14

Manuscript in preparation

Yan, F.; Earl, D. J.

8.1 INTRODUCTION

Liquid crystal (LC) mixtures are formed by mixing two or more types of liquid crystalline compounds, or by adding non-liquid crystalline additives, such as chiral dopants or UV-stabilizers, to liquid crystalline compounds[179, 38, 2]. Liquid crystal mixtures have many advantages over single-component liquid crystals, and desired properties and new phases can be created with a suitable composition of the different components in the mixture[31, 179]. For example, most LC devices contain liquid crystal mixtures that have been optimized to improve the performance of the device[32], and the addition of chiral dopants into achiral liquid crystal systems can induce chirality in the liquid crystalline phases, a method often employed in liquid crystal displays (LCDs)[180, 181]. Also by proper mixing 6-[4-(butyloxy)phenyl]-3-(octyloxy)pyridazine (6PhPz) with 2-[4-(tetradecyloxy)-phenyl]-5-(tetradecyloxy)pyrimidine (PhP14), where both only exhibit SmC phase, a SmA phase can be generated.[2]

Computer simulations have played an important role in developing theories of liquid crystalline phases and guiding experimentalists in the targeted synthesis of liquid crystals[23, 10, 24]. Most simulations of liquid crystal mixtures have used simplified coarse-grained models, which are capable of determining much of the essential physics for liquid crystalline phase formation and are more efficient than all-atom models[23]. Examples include hard

potential models[182, 183, 184, 185, 186, 187, 188, 189, 190, 191, 192] and simulations using the Gay-Berne potential[193, 194] Hard potential models consider only the shape-based entropic driving force for liquid crystalline phase formation, where a change in system density can induce a phase transition[23]. However, hard potential models are not capable of capturing the effects of temperature, or determining the influence of important classes of interactions, such as van der Waals and electrostatic interactions, on the phase behavior of a system[23, 182, 183, 184, 185, 186, 187, 188, 189, 190, 191, 192]. On the other hand, the Gay-Berne potential models include temperature effect and important intermolecular interactions such as van der Waals and electrostatic interactions[61, 193, 194], and intramolecular interactions such as bond interactions[195, 194]. However, due to the lack of molecular structure details, they are incapable of reproducing the molecular system phase behavior change caused by a subtle chemical change to the structure of constitute molecules.[1, 89] In order to capture this effect, atomistic simulations are necessary. However, atomistic simulations of liquid crystals have been hindered by the long time and length scales required for the formation of liquid crystalline phases, and the need for accurate liquid crystal force fields. This situation has been partially alleviated by the recent development of larger and faster computers, better parallel algorithms[163], and more accurate force fields designed specifically for liquid crystals[8, 78, 83, 84, 85, 79]. There have been a number of notable atomistic simulations of liquid crystals[71, 72, 73, 74, 75, 76, 78, 79, 80, 89, 77, 82]. Among these, only two have been performed on liquid crystal mixtures; one by Lansac *et al.* on smectic mixtures of p,p'-diheptylazobenzene (7AB) and 4-octyl-4′-cyanobiphenyl (8CB) molecules[77], and the other by Pelaez and Wilson on a nematic mixture of E7[82] (see its definition in chapter 7). Compared with nematic mixtures, smectic mixtures are more difficult to simulate at an atomistic level of detail. This difficulty stems from two main factors. First, in order to fully demonstrate smectic phase formation, one needs to assemble the system from a more disordered state, and use a sufficiently large system to form at least three smectic layers in order to rule out the influence of periodic image interactions. Second, polydispersity in the mixtures frustrates the self-assembly of the molecules into ordered smectic layers [86], thus requiring longer equilibration times making the computation more expensive.

In this chapter, simulations of a binary liquid crystal mixture of alkoxy substituted

phenylpyrimides 2-[4-(butyloxy)phenyl]-5-(octyloxy)pyrimidine (2PhP) and 2-[4-(tetradecyloxy)phenyl]-5-(tetradecyloxy)pyrimidine (PhP14) are presented by using molecular dynamics simulations in the isothermal-isobaric (NPT) ensemble at the all atom level, where the molecular length of PhP14 is 1.8 times that of 2PhP. The choice of system is influenced by the experimental work of Kapernaum *et al.*[2], where the length bidisperity was found to dramatically influence the phase behaviour of the binary mixture. System sizes of 1000-1600 molecules are employed in order to allow for the formation of at least three smectic layers in simulations, and the simulations are conducted from the isotropic phase through to the liquid crystalline phases by using a simulated annealing method. Pure 2PhP and pure PhP14 are simulated at the beginning, and then twelve mixtures with the mole fractions of PhP14 as 0.050, 0.076, 0.091, 0.167, 0.286, 0.412, 0.444, 0.681, 0.762, 0.800, 0.833, and 0.909. Mixtures at small mole fractions of PhP14 form isotropic, nematic, smectic A and smectic C phases. A small increase in the mole fraction of PhP14 destablizes the smectic C and nematic phases and stablizes the smectic A phase, which dominates the liquid crystalline phase behavior for large regions of the binary phase diagram. An out-of-layer fluctuation arrangement of molecules is demonstrated to be responsible for the stabilization of the smectic A phase. The simulation results are in good agreement with experiment[2], and show the possiblity of designing liquid crystal mixtures with desired and tunable properties. The rest of this chapter is organized as follows: in section 8.2 the computational method and simulation procedures that was employed are presented in section 8.2; simulation results and their implications are presented in section 8.3; and conclusions are made in section 8.4.

8.2 COMPUTATIONAL DETAILS

Molecular structures and ab initio optimized geometries for 2PhP and PhP14 are shown in Fig. 36,

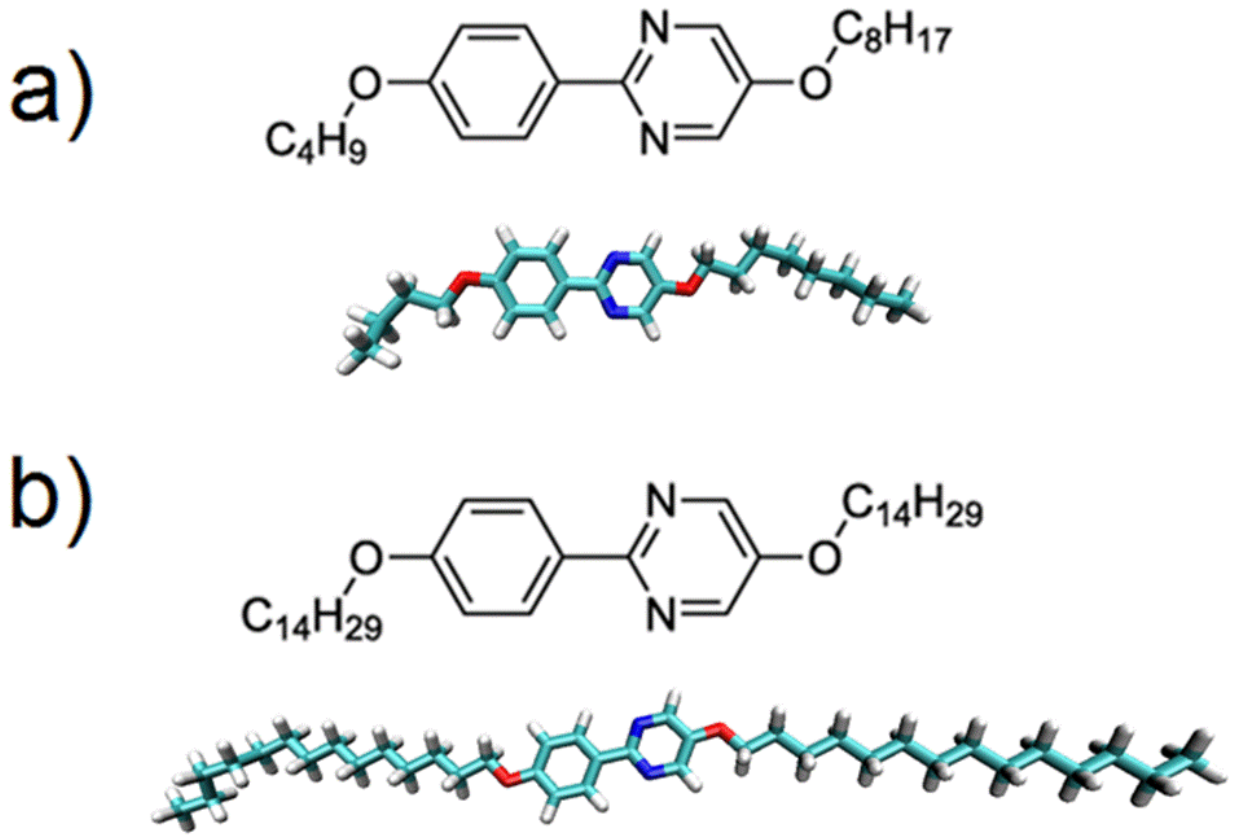

Figure 36: Molecular structures (top) and ab-initio optimized[7] geometries (bottom) of (a) 2PhP (2-[4-(butyloxy)phenyl]-5-(octyloxy)pyrimidine) and (b) PhP14 (2-[4-(tetradecyloxy)phenyl]-5-(tetradecyloxy)pyrimidine).

where the molecular lengths of 2PhP are PhP14 in their optimized geometries are 2.56 and 4.55 nm, respectively. The optimized geometries were calculated by density functional theory at the B3LYP/6-31(d,p) level.[7] Both 2PhP and PhP14 have a phenylpyrimidine core, substituted with alkoxy chains on both sides, where 2PhP has two alkyl groups of C_4H_9 on one side and C_8H_17 on the other side, and PhP14 has one C_14H_29 alkyl group

on each side. All molecular dynamic simulations were conducted with a parallel version of Gromacs 4.0.5[163, 164, 165, 166]. A simulated annealing method was used to keep track of all phase transitions and to construct the phase diagram for mixtures at different mole fractions of PhP14, x_{PhP14}. The intra- and intermolecular interactions were treated with liquid crystal force field (LCFF)[8]. The potential energy expression is given by eq. (7.1).

All bonds were constrained using the LINear Constraint Solver (LINCS)[168] method, and a time step of 2 fs was used. The long range electrostatic interactions were treated with the smooth particle mesh Ewald (SPME) method[169] with a PME of 4th order and an Ewald convergence of 0.00001. A cut-off distance of 1.2 nm was used for both short-range van der Waals interactions and real-space electrostatic interactions. All simulations were conducted in the isothermal-isobaric ensemble (NPT) at 1 atomsphere using a Nosé-Hoover thermostat[97, 98] and an isotropic Parrinello-Rahman barostat[170] with relaxation times of 1 and 5 ps.

Simulation system sizes of 1500 molecules were employed for the pure 2PhP system, and 1024 molecules for the pure PhP14 system, making the total number of atoms 87000 for 2PhP and 108544 for PhP14. The system sizes for simulations of mixtures were between 1000-1600 molecules making the total number of atomic sites between 76384 and 128520. Such large system sizes are used to obtain at least three layers in smectic phases to minimize the influence of periodic boundary conditions. A simulated annealing method was used to track all phase transitions and the annealing procedure was implemented as follows. All simulations started in cubic boxes with densities as low as 0.001 g cm^{-3} and with periodic boundary conditions employed. The systems were compressed over 10 ps using a high pressure of 10000 bar at 50 K until the systems reached a density close to 0.70 g cm^{-3}. The systems were then heated up to 800 K over 5.5 ns at 1 atmosphere, and became isotropic at equilibrium. Following this, all systems were cooled using a simulated annealing procedure. Fast annealing was performed for systems above 600 K, which is much higher than the highest experimental phase transition temperature from the isotropic to liquid crystal phases for the systems studied[2]. Systems were sequentially cooled from 800 K to 700 K using 0.5 ns of cooling and 0.5 ns equilibration, then to 600 K using 1.0 ns of cooling and 2.0 ns equilibration. A slightly slower annealing was performed between 600 K and 550 K. In this range, 2 ns

of cooling and 2 ns of equlibration time were chosen for each interval. Below 550 K we employed a temperature interval of 20 K, until the systems became crystalline, with 4 or 5 ns of cooling time and 4 ns of equilibration time for each temperature interval.

Phase transition temperatures from the isotropic to nematic phase were determined by following the same procedure as described in chapter 7. A series of molecular dynamics simulations were performed at fixed temperatures within 15 K of the estimated temperature, with 0.5 to 3 K temperature intervals between simulations, at 1 atmosphere in the NPT ensemble. Each of these simulations was equilibrated until the nematic order parameter did not drift significantly, and then continued for a further 5 ns. Then the isotropic-to-nematic phase transition temperature was determined by following the method utilized by Berardi *et al.*[75] by fitting the nematic order parameters to the Haller equation[6]. Other phase transitions were identified in a similar way, with a number of fixed temperature simulations performed close to the estimated temperatures from the annealing run. Liquid crystal phases were identified and characterized using a variety of techniques including the calculation of radial and pair distribution functions, the calculation of tilt with respect to the orientational order parameter, and through visualization methods. Total simulation times were 60-100 ns.

After locating all the phase transition temperatures for mixtures of 2PhP and PhP14 at different mole fractions of PhP14, a binary phase diagram of the mixed system as a function of the mole fraction of PhP14, x_{PhP14}, was constructed at different temperatures and at a constant pressure of 1 atmosphere.

8.3 RESULTS AND DISCUSSION

The binary phase diagram of liquid crystal mixtures of 2PhP and PhP14 is shown in Fig. 37.

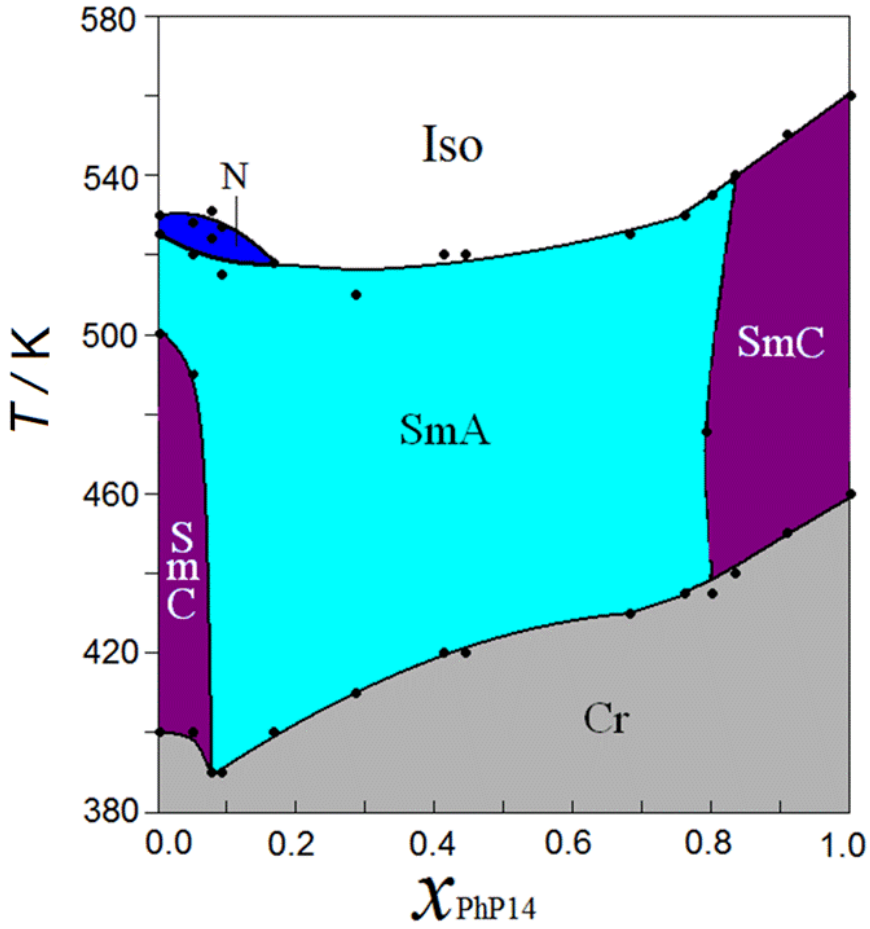

Figure 37: Phase diagram of the binary system 2PhP/PhP14 at a pressure of 1 atmosphere. x_{PhP14} is the mole fraction of PhP14 in the mixture. The nematic (N, blue) phase exists at $0.0 \leq x_{\mathrm{PhP14}} \leq 0.167$. The smectic A (SmA, cyan) phase exists at a very broad phase region at $0.0 \leq x_{\mathrm{PhP14}} \leq 0.833$. The smectic C (SmC, purple) phase exists at lower mole fractions of PhP14 $0.0 \leq x_{\mathrm{PhP14}} < 0.076$ and at higher mole fractions of PhP14 $0.762 < x_{\mathrm{PhP14}} \leq 1.0$. Both isotropic (Iso, white) and crystal (Cr, gray) phases cover the whole phase region, where the Iso exists at the highest temperatures and the Cr at the lowest temperatures.

The pure 2PhP system self-assembles into isotropic (Iso), nematic (N), smectic A (SmA), smectic C (SmC) and crystal (Cr) phases, which are shown in Figs. 38a, 38b, 38c and 38d (Cr phase not shown), respectively.

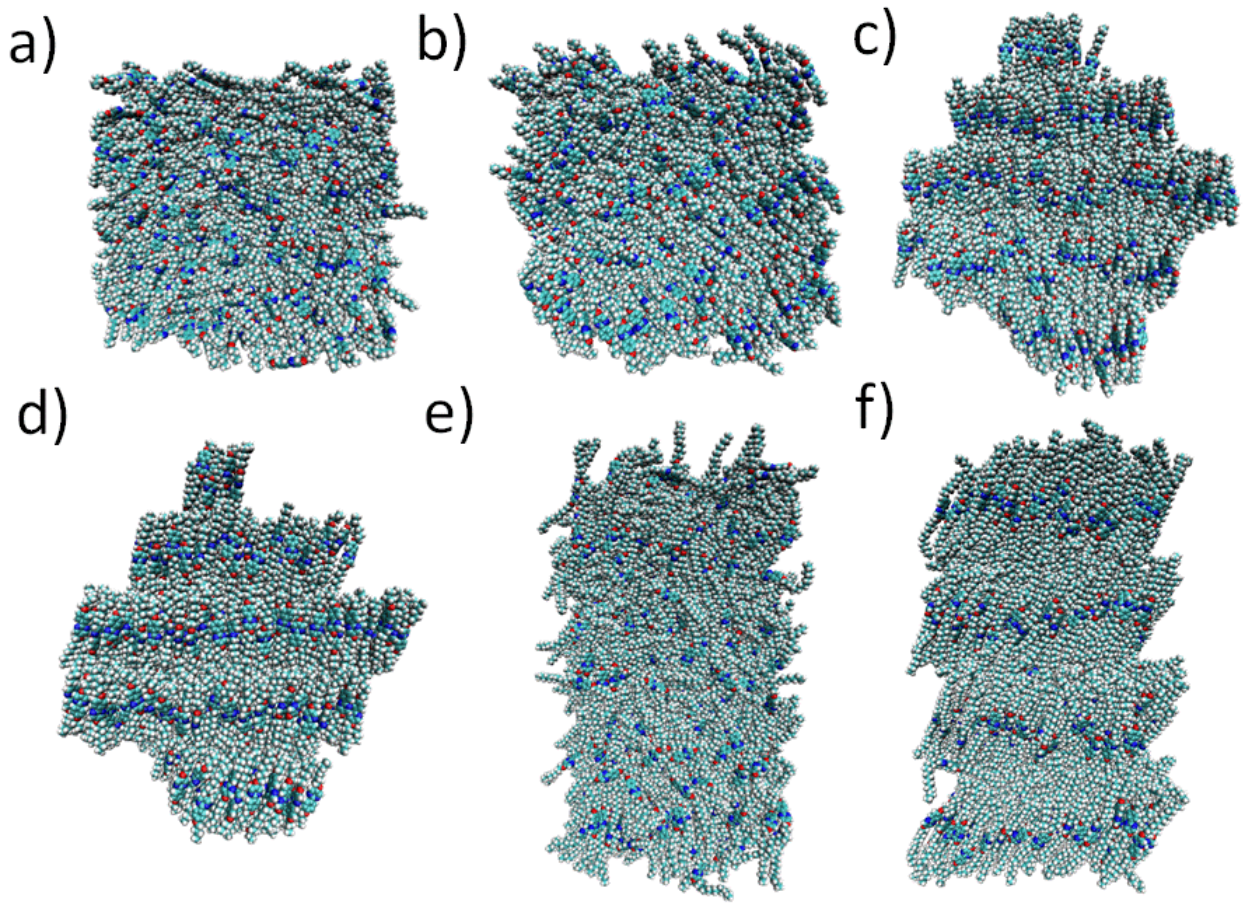

Figure 38: Snapshots taken from our simulations of a pure 2PhP system showing (a) an isotropic phase (Iso), (b) a nematic phase (N), (c) a smectic A phase (SmA), (d) a smectic C phase (SmC); and a pure PhP14 system showing (e) an isotropic phase (Iso) and (f) a smectic C phase (SmC).

The pure PhP14 system self-assembles into Iso, SmC and Cr phases, which are shown in Figs. 38e and 38f (Cr phase not shown). Adding PhP14 into the 2PhP system destablizes the SmC phase significantly, which disappears at a eutectic point of $x_{\mathrm{PhP14}} = 0.076$. Concurrently, the SmA phase becomes stablized over a wider temperature range. The N phase forms over a small temperature range of 13 K, and disappears at $x_{\mathrm{PhP14}} \geq 0.167$.

While the SmC and N phases of the 2PhP system disappear with the addition of small concentrations of PhP14, the SmA phase is stablized and becomes the dominant LC phase across a broad region of the binary phase diagram between $0.076 \leq x_{\mathrm{PhP14}} \leq 0.80$. The SmC phase reappears at $x_{\mathrm{PhP14}} = 0.8$, and becomes the dominant LC phase for higher values of x_{PhP14}. This simulated binary phase diagram agrees well with experiment[2]. A eutectic point at $x_{\mathrm{PhP14}} = 0.075$ was found in experiment and is very close to the value of $x_{\mathrm{PhP14}} = 0.076$ found from our simulations. Compared to simulations, the N phase in the experiment has a broader range of stability, from $0.0 \leq x_{\mathrm{PhP14}} \leq 0.3$, the SmC phase reappears at a lower mole fraction of PhP14, at $x_{\mathrm{PhP14}} = 0.65$, and the SmA phase has a smaller region of phase stability, dominating between $x_{\mathrm{PhP14}} = 0.075$ and 0.65.[2]

Although the phase behavior of the pure and mixed systems show good agreement with experiment, there are larger discrepancies between the phase transition temperatures in the simulations and the experimental[2] values. For example, the greatest discrepancy occurs for the isotropic-to-smectic C transition for the pure PhP14 system, which was found to occur at 555 K in the simulations and at 373 K in experiment. The prediction of higher phase transition temperatures in atomistic simulations than measured experimentally has been reported by several workers[174, 173, 120, 196, 175, 176, 89], including the atomsitic simulation of alkenic fluorotephenyls in chapter 7[89]. The transition temperatures in simulations are dependent on the force field employed. As most modern force fields have been parameterized at room temperature[175], they do not accurately represent systems far from 300 K. This may partly account for the higher predicted transition temperatures and indicates that the force field employed here still needs to be improved to provide a more accurate prediction of phase transition temperatures.

A simulated annealing protocol was used to track the phase transitions in the simulations. Fig. 39 shows the evolution of the nematic order parameter over a simulated annealing simulation for a mixture with $x_{\mathrm{PhP14}} = 0.051$ that spontaneously self-assembles into N, SmA, SmC and Cr phases upon cooling from the Iso phase.

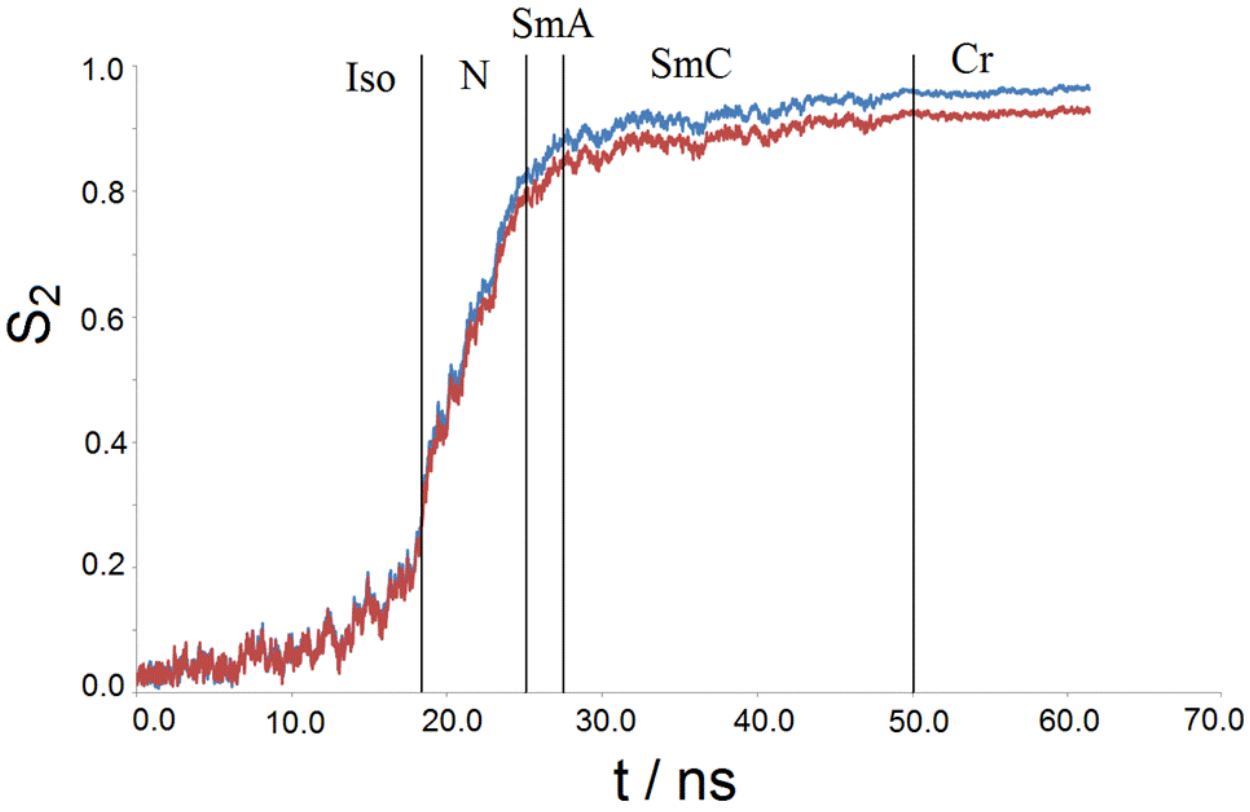

Figure 39: The time dependence of the nematic order parameter, S_2, for a binary mixture with $x_{\mathrm{PhP14}} = 0.051$ by simulated annealing using molecular dynamics in the isothermal-isobaric ensemble. The binary mixture started with an isotropic phase at $T = 800$ K and was cooled down to form a crystal phase at $T = 400$ K. Four phase transitions occur during the process; these are isotropic to nematic (Iso-N), nematic to smectic A (N-SmA), smectic A to smectic C (SmA-SmC) and smectic C to crystal (SmC-Cr). The blue (upper) line represents S_2 calculated from the inertia tensor for the whole molecule and the red (lower) line represents S_2 calculated from the inertia tensor for the phenylpyrimidine core of the molecules.

The nematic order parameter, S_2, is defined as by eq. (7.2). There are several options for choosing the molecular axis, and the eigenvector corresponding to the largest eigenvalue of the moment of inertia tensor for molecules in the mixture was chosen. In order to investigate the flexible chain influence on the stabilization of the smectic layers, the moment of inertia tensor for the phenylpyrimidine core of the molecules in the mixture was also chosen for comparison. Fig. 39 shows that the time evolution of the nematic order parameter calculated from the moment of inertia tensor for the whole molecule is higher than that calculated from only the rigid aromatic part of the molecules, indicating that the flexible chains effectively increase the order of the smectic layers, similar to the simulation results for a series of fluorinated terphenyls[89] in chapter 7, and Pelaez and Wilson's simulation for a nematic mixture E7[82].

All phases formed in our simulations are described as follows. The N phase for pure 2PhP ($x_{\mathrm{PhP14}} = 0.0$) is shown in Fig. 38b, has orientational order along the system director, but the observed absence of layer formation indicates no positional order. For nematic-isotropic transitions, the temperature dependence of the nematic order parameter was fitted to the Haller equation[6], following a number of fixed temperature simulations in the interval over which the transition was observed in the simulated annealing run. The Haller equation is defined by eq. (7.3). T_{NI} was chosen as the smallest of the temperatures with $< S_2 > \leq 0.25$. $< S_2 >_{iso}$ was calculated by averaging all $< S_2 >$ values corresponding to $T \geq T_{NI}$. The fitting curve for a mixture with $x_{\mathrm{PhP14}} = 0.091$ is shown in Fig. 40. The value for the critical exponent, β, is 0.19 and close to $\beta = 0.2$, which yielded a satisfactory fit[171], and T_{NI} was calculated to be 527 K. The average density as a function of temperature was also calculated, and the density was found to decrease linearly with increasing temperature, similar to the nematic system in Berardi *et al.*[75], indicating a $N - I$ transition.

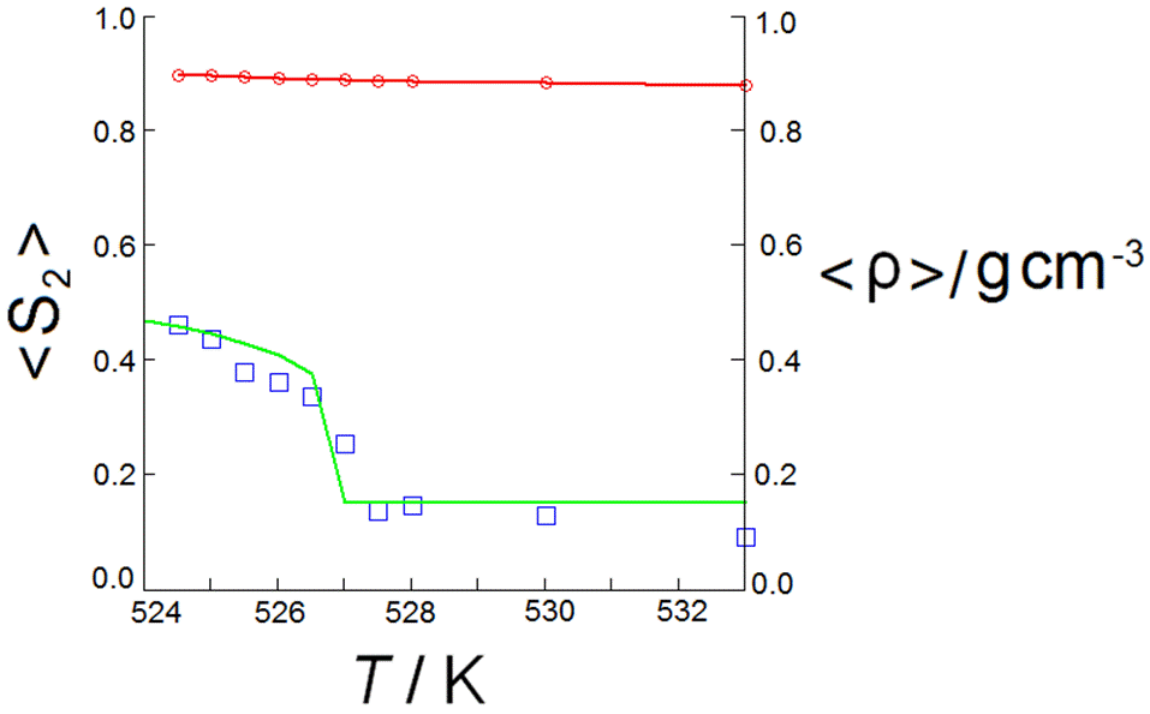

Figure 40: The temperature dependence of the average nematic order parameter $< S_2 >$ (blue boxes) and Haller fit[6] (green line, see eq. (9.3)), and the average density (red circled line) for a binary mixture with $x_{\mathrm{PhP14}} = 0.091$.

For the pure 2PhP system, the SmA, SmC and Cr phases were observed at low temperatures. The N to SmA phase transition was monitored by observing smectic layer formation through visualization and by the calculation of radial distribution functions (RDFs). The N phase is more liquid-like than smectic phases, as demonstrated in the radial distribution function $g(r)$ in Fig. 41a. The radial distribution functions show a first peak at a distance between 0.49 and 0.52 nm for all phases, with the intensity increasing from the nematic to smectic phases, and which is most intense in the crystal phase. A second peak at a distance between 0.87 and 0.90 nm is almost indistinguishable for the nematic phase, but is shown clearly for the smectic phases. In the Cr phase, a fine structure appears in the long range oscillations. As shown in Fig. 38c, the SmA phase is characterized by untilted layers. Decreasing the temperature results in the formation of a SmC. The SmC phase is characterized

by tilted layers (Fig. 38d). The Cr phase formed upon cooling from the SmC is a "frozen" tilted smectic phase, which may correspond to a deformed SmI or crystal J phase.

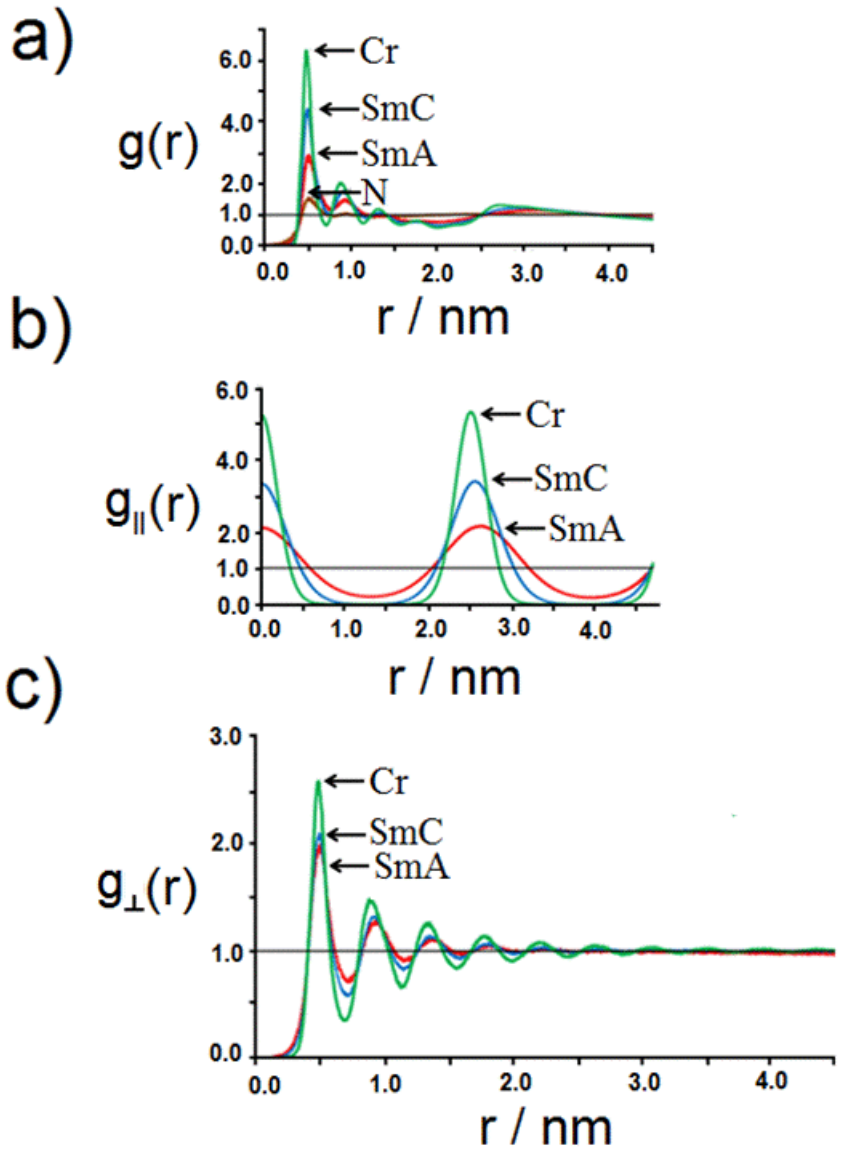

Figure 41: For a system of 1500 molecules at 1 atmosphere the (a) The radial distribution function, $g(r)$, calculated with respect to the centre atom which is closest to the molecular center of mass of each molecule. (b) The longitudinal distribution function, $g_{\parallel}(r)$. (c) The in-plane distribution function, $g_{\perp}(r)$. The distribution functions are shown for the nematic (brown), smectic A (red), smectic C (blue), and crystal (green) phases.

In order to characterize the smectic layer structures, the longitudinal distribution function, $g_{\parallel}(r)$, was calculated and shown for the pure 2PhP system in Fig. 41b. There are periodic peaks indicating order along the layer normal. In the SmA phase, the oscillatory peaks are significant, indicating ordered layer packing. The periodic peaks become both sharper and more intense in the SmC and Cr phases. The average separation between the peaks can be used to determine the layer spacing, and are calculated as 2.60 ± 0.01 nm, 2.52 ± 0.01 nm, and 2.50 ± 0.01 nm for the SmA, SmC and Cr phase respectively, which is comparable to the molecular length of optimized 2PhP of 2.55 nm. To explore the structure within each smectic layer, the in-plane distribution function, $g_{\perp}(r)$, was calculated and shown in Fig. 41c for the pure 2PhP system. In both the SmA and SmC phase the structure within the layer is clearly liquid like, and the in-plane distribution function shows no long range structure. In the Cr phase, there is hexagonal ordering and the in-plane order extends to large distances with a fine structure evident in the long range peaks. The first peak appears at a distance of 0.48 nm, and the separation distance between the peaks constituting this fine structure is approximately 0.42 nm, which is about $2^{-\frac{1}{6}}$ nm of the distance relative to the first peak, and can be attributed to the hexagonal order within the layer.

As shown in the phase diagram, the SmA phase dominates for the mixtures between $0.076 \leq x_{\mathrm{PhP14}} \leq 0.80$. In order to understand this stabilization of the SmA phase, the SmA layer structures for mixtures at different values of x_{PhP14} were investigated by calculating their the longitudinal distribution functions, as shown in Fig. 42a. The layer spacings for mixtures with $x_{\mathrm{PhP14}} = 0.076$, 0.167, 0.444 and 0.684 are 2.822, 2.916, 3.562 and 4.10 nm, respectively. Thus, increasing x_{PhP14} increases the layer spacing of the SmA phase. All the SmA layer spacings based on the longitudinal distribution functions were calculated and plotted in terms of x_{PhP14}, as shown in Fig. 42b. The layer spacing of the SmA phase for the mixtures was found to obey the Diele additivity rule[197],

$$d_{\mathrm{Mix}} = d_{\mathrm{A}} x_{\mathrm{A}} + d_{\mathrm{B}} x_{\mathrm{B}} \tag{8.1}$$

where d_{Mix}, d_{A} and d_{B} are the layer spacings of mixtures, component A and component B, respectively. And x_{A} and x_{B} are the mole fractions of A and B, respectively.

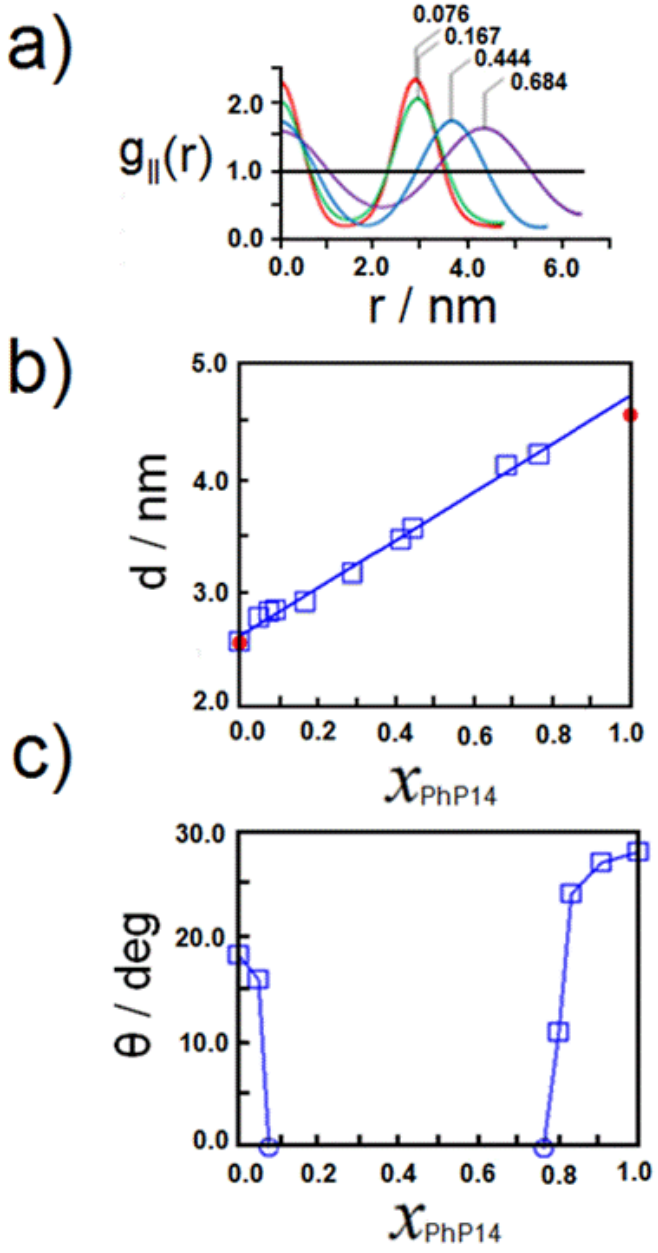

Figure 42: (a) The longitudinal distribution functions of mixtures at $x_{\mathrm{PhP14}} = 0.076$, 0.167, 0.444 and 0.684. (b) The SmA layer spacing (open square) increases with the mole fraction of x_{PhP14}. The molecular lengths of 2PhP and PhP14 are shown for comparison with the extrapolated values of the fitting line (blue) at $x_{\mathrm{PhP14}} = 0.0$ and 1.0, respectively. (c) The SmC tilt angles (open square) for mixtures at different values of x_{PhP14}, where all points are connected for viewing purpose. The SmC phase disappears at $x_{\mathrm{PhP14}} = 0.076$ and reappears at $x_{\mathrm{PhP14}} = 0.762$, and is shown with a zero tilt (open circle).

This has also been observed in experiments[2]. The extrapolated values from the simulations are 2.62 nm for the pure 2PhP system ($x_{\mathrm{PhP14}} = 0.0$) and 4.72 nm for pure PhP14 system ($x_{\mathrm{PhP14}} = 1.0$), which are very close to the respective molecular lengths of 2PhP (2.56 nm) and PhP14 (4.55 nm) found from the optimized geometries, indicating that the molecules in the mixtures have extended conformations[2]. The tilt angle of the smectic C phase was also calculated and shown in Fig. 42c. The tilt angle for the SmC in the pure 2PhP system was calculated to be 18.1°, which is close to the experimental value of 21.0°[198]. The tilt angle for the SmC in the pure PhP14 system was calculated to be 28.0°, which is very close to the experimental value of 27.0°[2]. At small values of x_{PhP14}, the tilt angle decreases with decreasing x_{PhP14} and goes to approximately zero at $x_{\mathrm{PhP14}} = 0.076$, corresponding to a SmA phase. At large values of x_{PhP14}, the SmC phase reappears, at $x_{\mathrm{PhP14}} = 0.8$, with a tilt angle of 10.8°. The tilt angle increases with x_{PhP14} reaching a maximum at $x_{\mathrm{PhP14}} = 1.0$. This tilt angle dependence on the value of x_{PhP14} can be utilized to make SmC phases with tunable tilt angles.

The SmA layer structure was further investigated by using visualization in order to determine if the SmA layer structure differs with x_{PhP14}. Figure. 43a shows the SmA structure of a mixture with $x_{\mathrm{PhP14}} = 0.167$, where the shorter 2PhP molecules form definite smectic layers, and the longer PhP14 molecules are arranged between the layers. The PhP14 molecules are observed to lie between the layers increases the layer spacing of the SmA phase, as compared to that of the pure 2PhP system, and following the Diele additivity rule[197]. Figure 43b shows the SmA layer structure for a mixture with $x_{\mathrm{PhP14}} = 0.684$, where the longer PhP14 molecules form definite smectic layers, with the shorter 2PhP molecules lying within and between different layers. The smectic A layers formed by PhP14 molecules are not well-defined, where the molecules from different layers pack more closely than in normal smectic layers, and make the layer spacing smaller, also following the Diele additivity rule[197]. Thus, the molecules in the SmA phases in the binary mixtures take an out-of-layer fluctuation arrangement, where the molecules of the lower mole fraction position themselves between the smectic A layers formed by the other molecules.

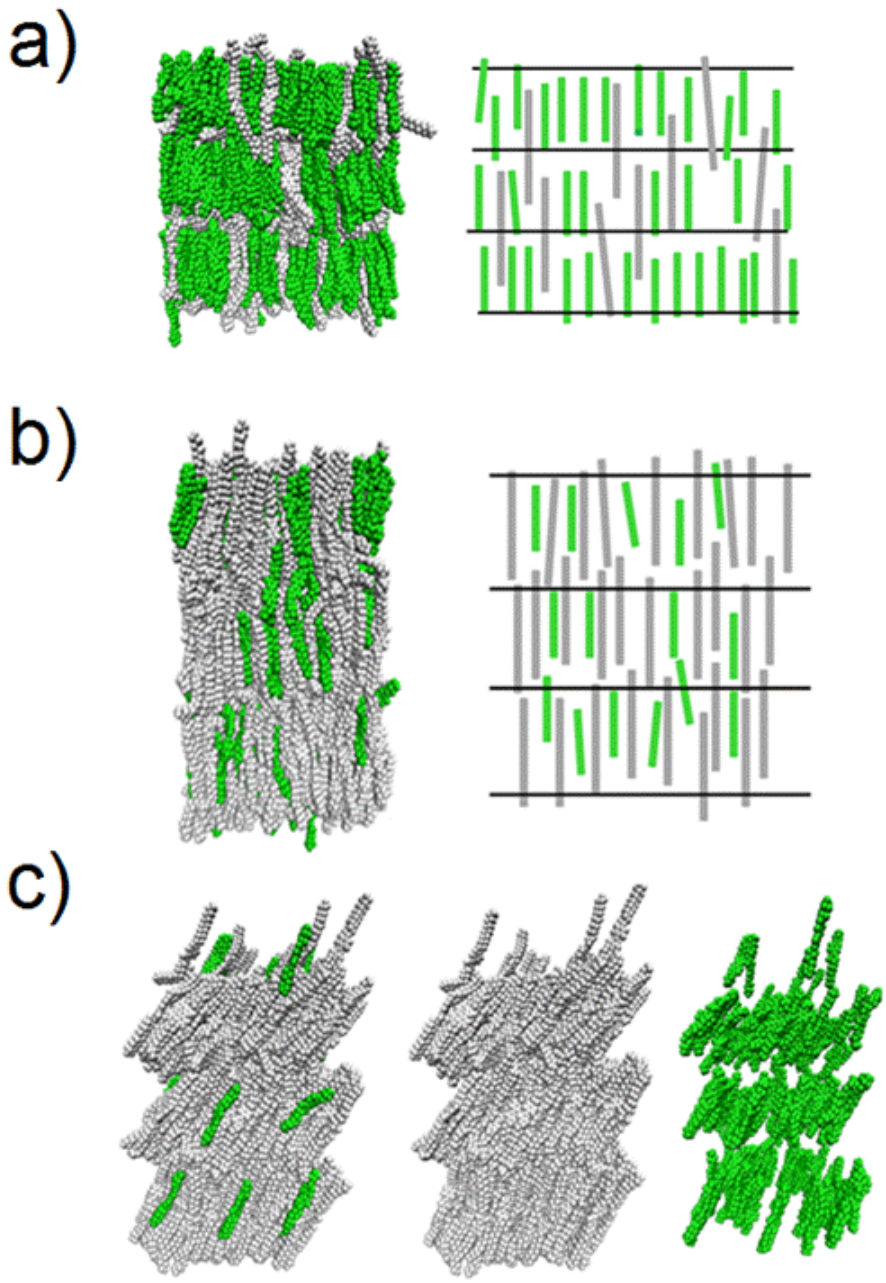

Figure 43: (a) (Left) Snapshot of a SmA phase for a mixture with $x_{\mathrm{PhP14}} = 0.167$ at 485 K. (Right) Schematic sketch. (b) (Left) Snapshot of a SmA phase for a mixture with $x_{\mathrm{PhP14}} = 0.684$ at 480 K. (Right) Schematic sketch version. (c) Snapshot of a SmC phase for a mixture with $x_{\mathrm{PhP14}} = 0.833$ at 460 K showing the whole mixture (left), only the 2PhP molecules (center), and only the PhP14 molecules (right). In order to guide the view, we represent PhP14 molecules in white and 2PhP molecules in green.

This out-of-layer fluctuation arrangement also explains the absence of a SmC phase for most binary mixtures, because the core-core interactions are important for SmC formation [199], and these are weakened in an out-of-layer fluctuation arrangement. The out-of-layer fluctuation arrangement for molecules in SmA mixtures was also found in the experiment of Kapernaum *et al.*[2, 199] and in simulations of binary mixtures of hard spherocylinders, where the molecular length of the long spherocylinders are twice that of the short spherocylinder[185, 182, 183]. These simulations showed that entropy alone can drive the out-of-layer fluctuation arrangement in a binary mixture and we posit that it is also the driving force in our simulations. Unsurprisingly, no SmC phases are found in hard spherocylinder models.

The SmA phase is destabilized when x_{PhP14} exceeds 0.80, and disappears at $x_{\mathrm{PhP14}} \geq 0.8333$. In contrast, the SmC phase reappears at $x_{\mathrm{PhP14}} = 0.80$ and becomes the only smectic phase at $x_{\mathrm{PhP14}} \geq 0.833$. This is to be expected because the pure PhP14 system only forms the SmC phase, and when the mole fraction of PhP14 increases above this threshold, the effect of the shorter 2PhP molecules becomes negligible and only a SmC forms. The SmC layer structure was further investigated by using visualization. Figure 43c shows the SmC structure for a mixture with $x_{\mathrm{PhP14}} = 0.833$. Most of the short 2PhP molecules are observed to lie within the smectic C layers, and not in an out-of-layer fluctuation arrangement required to form the SmA phase.

8.4 CONCLUSION

In this work the phase behaviour of liquid crystal mixtures of 2PhP and PhP14 has been studied by using molecular dynamics simulations in the isothermal-isobaric ensemble at the all atom level. The different molecular lengths of the two molecules results in interesting behavior in the mixed system, where the molecular length of PhP14 is 1.8 times that of 2PhP. A pure 2PhP system was shown to self-assemble into isotropic, nematic, smectic A, smectic C phases, and a pure PhP14 system was shwon to self-assemble into isotropic and smectic C phases. Mixtures of the two molecules show a stabilization of the smectic A

phase at the expense of the smectic C and nematic phases, where the smectic A phase is the dominant liquid crystal phase for large regions of the binary mixture phase diagram. This is a concentration induced phase transition from the smectic C to the smectic A phase in the mixture, and it has been demonstrated here that the main driving force for SmA formation in the binary mixture is an out-of-layer fluctuation arrangement, which also disfavors the formation of a SmC phase in the mixtures. The ability to computationally produce a phase diagram of a binary mixture using atomistic simulation that has a good agreement with experiment opens the possibility of designing new liquid crystal mixtures using theoretical methods.

9.0 SUMMARY

9.1 CONCLUSION

In chapters 4-6, the phase behaviors of rigid bent-core and rigid linear model systems have been systematically studied. Phase diagrams of these models have been mapped out by using molecular dynamics simulation in the isothermal-isobaric ensemble and/or the canonical ensemble, and very rich phase behaviors have been found for both model systems. In both models, chiral superstructures self-assemble at low volume ratios and/or low pressures, and liquid crystalline phases at high volume ratios and/or high pressures. The interesting chiral superstructures rules out any nucleation mechanism requiring transient chirality due to the rigid nature of our models, and was found to be the minima of the potential energy surface using energy minimization and parallel tempering simulations.

The shape effect on the phase behavior of bent-core molecules have been investigated by varying the bending angle γ, and the arm length ratios of attractive LJ particles N_A to soft-repulsive WCA particles N_B, by varying N_B while keeping N_A constant. It was found that chiral phases and liquid crystalline phases can be tuned by altering the bending angle γ and the arm length ratio N_A / N_B. The influence of the spacing between Lennard-Jones particles has also been investigated for the rigid linear model molecule, and it has been shown that correct spacing is required to form chiral phases. These findings may act as a design principle by which chiral superstructures and liquid crystalline phases can be realized with bent-core and linear molecules.

In chapters 7-8, fully atomistic molecular dynamics simulations have been used to study the phase behaviors of both a series of single component liquid crystals of di-, tri- and tetrafluoroterphenyls (chapter 7), and of binary liquid crystal mixtures of 2PhP and PhP14

(chapter 8). To our knowledge, these are the largest liquid crystal atomistic simulations to date. These atomistic simulations have been shown to be capable of capturing the phase behavior change due to very small variations in molecular structure of di-, tri-, and tetrafluoroterphenyl, which is not possible to do with coarse-grained models due to the its lack of molecular details. The atomistic simulations have also been shown to provide microscopic details regarding the mechanisms that govern phase stability in the liquid crystal mixtures of 2PhP and PhP14. These simulation results are in good agreement with the experiments[1, 2], and open the possibility of designing new liquid crystal materials with desired phase behaviors prior to experiment.

9.2 FUTURE DIRECTIONS

In future work of the coarse-grained models, the influence of chemical patterning on the bent-core and linear model molecules will be studied. The chemical patterning will be altered by replacing the attractive LJ particles with the soft-repulsive WCA particles, and vice-versa, and by introducing charged sites and dipoles.

Our preliminary parallel tempering simulations on both bent-core and linear model molecules have found that simple alternative chemical patterning can drive assembly towards spherical, achiral barrel-shaped, and chiral barrel-shaped micelles, as shown in Fig. 44. How this chemical patterning affects the formation and stability of denser phases will be further investigated in the future.

In the future work of the atomistic model, a multi-scale modeling study of chiral liquid crystalline phases will be conducted. Atomistic simulations of chiral liquid crystals are more challenging than that of normal liquid crystals. As shown in Fig. 2c, in order to confirm the chiral smectic C phase, several smectic layers are required to form, which make the system size prohibitively large. In order to tackle this problem, first, atomistic simulations will be performed on a few thousand liquid crystal molecules, then part of the molecule will be replaced with a simplified coarse-grained model[200, 70]. The multi-scale model will be tested and improved by comparing with the simulation results of atomistic model, until

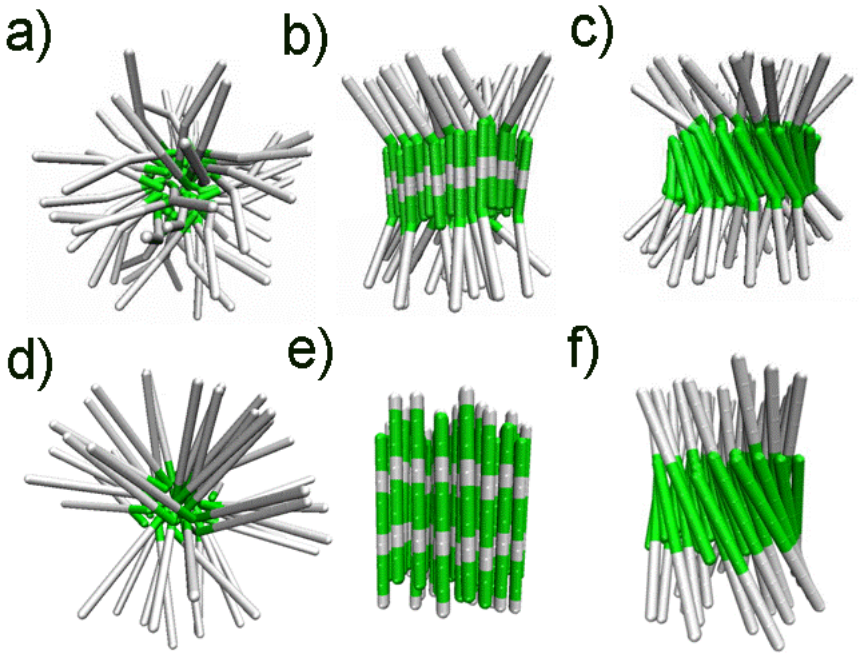

Figure 44: Preliminary parallel tempering simulations show that various patterning strategies can drive the self-assembly of bent-core molecules towards (a) spherical, (b) achiral barrel-shaped, and (c) chiral barrel-shaped micelles; and linear molecules also towards corresponding (d) spherical, (e) achiral barrel-shaped, and (f) chiral barrel-shaped micelles.

the model resolution is satisfied. Finally, this improved multi-scale model will be used for large-scale simulations, in hope to find chiral liquid crystals.

BIBLIOGRAPHY

[1] Gasowska, J., Cowling, S. J., Cockett, M. C. R., Hird, M., Lewis, R. A., Raynes, E. P., and Goodby, J. W. (2010) *J. Mater. Chem.* **20**, 299–307.

[2] Kapernaum, N., Hartley, C. S., Roberts, J. C., Lemieux, R. P., and Giesselmann, F. (2009) *Beilstein J. Org. Chem.* **5**, 65.

[3] Tepper, H. L. and Voth, G. A. (2005) *J. Chem. Phys.* **122**, 124906.

[4] Yan, F., Hixson, C. A., and Earl, D. J. Manuscript in preparation (2011).

[5] Coles, H. and Morris, S. (2010) *Nat. Photonics* **4**, 676–685.

[6] Haller, I. (1975) *Prog. Solid State Chem.* **10**, 103.

[7] Frisch, M. J., Trucks, G. W., Schlegel, H. B., Scuseria, G. E., Robb, M. A., Cheeseman, J. R., Montgomery, J. A., Vreven, T., Kudin, K. N., and Burant, J. C. (2003) et al. Gaussian 03, Revision C.02; Gaussian, Inc.:Pittsburgh PA, .

[8] Cheung, D. L., Clark, S. J., and Wilson, M. R. (2002) *Phys. Rev. E.* **65**, 051709.

[9] Glotzer, S. C. and Solomon, M. J. (2007) *Nat. Mater.* **6**, 557–562.

[10] Zannoni, C. (2001) *J. Mater. Chem.* **11**, 2637–2646.

[11] Zhang, Z., Horsch, M. A., Lamm, M. H., and Glotzer, S. C. (2003) *Nano Lett.* **3**, 1341–1346.

[12] Tschierske, C. (2002) *Nature* **419**, 681.

[13] Pelzl, G., Diele, S., and Weissflog, W. (1999) *Adv. Mater.* **11**, 707–724.

[14] Reddy, R. A. and Tschierske, C. (2006) *J. Mater. Chem.* **16**, 907–961.

[15] Chen, S., Wang, Z. L., Ballato, J., Foulger, S. H., and Carroll, D. L. (2003) *J. Am. Chem. Soc.* **125**, 16186–16187.

[16] Roh, K.-H., Martin, D. C., and Lahann, J. (2005) *Nat. Mater.* **4**, 759–763.

[17] Mohraz, A. and Solomon, M. J. (2005) *Langmuir* **21**, 5298–5306.

[18] Manna, L., Milliron, D. J., Meisel, A., Scher, E. C., and Alivisatos, A. P. (2003) *Nat. Mater.* **2**, 382–385.

[19] Sun, Y. and Xia, Y. (2002) *Science* **298**, 2176–2179.

[20] Petukhov, A., van derBeek, D., Dullens, R., Dolbnya, I., Vroege, G., and Lekkerkerker, H. (2005) *Phys. Rev. Lett.* **95**, 077801.

[21] Sekine, T., Niori, T., Watanabe, J., Furukawa, T., Choi, S. W., and Takezoe, H. (1997) *J. Mater. Chem.* **7**, 1307–1309.

[22] Bolhuis, P. and Frenkel, D. (1997) *J. Chem. Phys.* **106**, 666–687.

[23] Wilson, M. R. (2005) *Int. Rev. Phys. Chem.* **24**, 421.

[24] Care, C. M. and Cleaver, D. J. (2005) *Rep. Prog. Phys.* **68**, 2665–2700.

[25] Horsch, M. A., Zhang, Z., and Glotzer, S. C. (2005) *Phys. Rev. Lett.* **95**, 056105.

[26] Horsch, M. A., Zhang, Z., and Glotzer, S. C. (2006) *J. Chem. Phys.* **125**, 184903.

[27] Lintuvuori, J. S. and Wilson, M. R. (2009) *Phys. Chem. Chem. Phys.* **11**, 2116–2125.

[28] Horsch, M. A., Zhang, Z., and Glotzer, S. C. (2006) *Nano Lett.* **6**, 2406–2413.

[29] Nguyen, T. D., Zhang, Z., and Glotzer, S. C. (2008) *J. Chem. Phys.* **129**, 244903.

[30] Iacovella, C. R., Horsch, M. A., and Glotzer, S. C. (2008) *J. Chem. Phys.* **129**, 044902.

[31] De Gennes, P. G. (1993) Physics of Liquid Crystals, Oxford University Press, NY, .

[32] Schadt, M. (1997) *Annu. Rev. Mater. Sci.* **27**, 305–379.

[33] Strangi, G., Barna, V., De Luca, A., Versace, C., Scaramuzza, N., and Bartolino, R. (2006) *Opt. Express* **14**, 7737–7744.

[34] Kikuchi, H., Yokota, M., Y., H., Yang, H., and Kajiyama, T. (2002) *Nat. Mater.* **1**, 64–68.

[35] O'Brien, D. C., Faulkner, G. E., Wilkinson, T. D., Robertson, B., and Leyva, D. G. (2004) *Appl. Opt.* **43**, 3297–3305.

[36] Goodby, J. W., Saez, I. M., Cowling, S. J., Gortz, V., Draper, M., Hall, A. W., Sia, S., Cosquer, G., Lee, S.-E., and Raynes, E. P. (2008) *Angew. Chem. Int. Ed.* **47**, 2754–2787.

[37] Brake, J. M., Daschner, M. K., Luk, Y.-Y., and Abbott, N. L. (2003) *Science* **302**, 2094–2097.

[38] Collings, P. J. and Hird, M. (1997) Introduction to Liquid Crystals Chemistry and Physics, Taylor & Francis: London, .

[39] Nakata, M., Zanchetta, G., Chapman, B. D., Jones, C. D., Cross, J. O., Pindak, R., Bellini, T., and Clark, N. A. (2007) *Science* **318**, 1276.

[40] Takezoe, H. and Takanishi, Y. (2006) *Jpn. J. Appl. Phys.* **45**, 597–625.

[41] Link, D. R., Natale, G., Shao, R., Maclennan, J. E., Clark, N. A., Korblova, E., and Walba, D. M. (1997) *Science* **278**, 1924–1927.

[42] Niori, T., Sekine, T., Watanabe, J., Furukawa, T., and Takezoe, H. (1996) *J. Mater. Chem.* **6**, 1231–1233.

[43] Hough, L. E., Spannuth, M., Nakata, M., Coleman, D. A., Jones, C. D., Dantlgraber, G., Tschierske, C., Watanabe, J., Korblova, E., Walba, D. M., Maclennan, J. E., Glaser, M. A., and Clark, N. A. (2009) *Science* **325**, 452–456.

[44] Pelzl, G., Diele, S., Jakli, A., Lischka, C., With, I., and Weissflog, W. (2006) *Liq. Cryst.* **33**, 1519–1523.

[45] Pelzl, G., Eremin, A., Diele, S., Kresse, H., and Weissflog, W. (2002) *J. Mater. Chem.* **12**, 2591–2593.

[46] Weissflog, W., Dunemann, U., Schroder, M. W., Diele, S., Pelzl, G., Kresse, H., and Grande, S. (2005) *J. Mater. Chem.* **15**, 939–946.

[47] O'Callaghan, M. J., Wand, M. D., and Walker, C. M. (2004) *Appl. Phys. Lett.* **85**, 6344–6346.

[48] Kentischer, F., Macdonald, R., Warnick, P., and Heppke, G. (1998) *Liq. Cryst.* **25**, 341.

[49] Shen, D., Pegenau, A., Diele, S., Wirth, I., and Tschierske, C. (2000) *J. Am. Chem. Soc.* **122**, 1593–1601.

[50] Dantlgraber, G., Baumeister, U., Diele, S., Kresse, H., Luhmann, B., Lang, H., and Tschierske, C. (2002) *J. Am. Chem. Soc.* **124**, 14852–14853.

[51] Jakli, A., Kruerke, D., and Nair, G. G. (2003) *Phys. Rev. E* **67**, 051702.

[52] Yan, F., Hixson, C. A., and Earl, D. J. (2008) *Phys. Rev. Lett.* **101**, 157801.

[53] Chothia, C. (1973) *J. Mol. Biol.* **75**, 295–302.

[54] Muraoka, T., Cui, H., and Stupp, S. T. (2008) *J. Am. Chem. Soc.* **130**, 2946.

[55] Li, L., Jiang, H., Messmore, B. W., Bull, S. R., and Stupp, S. I. (2007) *Angew. Chem., Int. Ed.* **119**, 5977–5980.

[56] Tanaka, A., Inoue, K., Hisaki, I., Tohnai, N., Miyata, M., and Matsumoto, A. (2006) *Angew. Chem., Int. Ed.* **45**, 4142–4145.

[57] Lightfoot, M. P., Mair, F. S., Pritchard, R. G., and Warren, J. E. (1999) *Chem. Commun.* , 1945–1946.

[58] Sone, E. D., Zubarev, E. R., and Stupp, S. I. (2002) *Angew. Chem., Int. Ed.* **41**, 1705–1709.

[59] Ribo, J. M., Crusats, J., Sagues, F., Claret, J., and Rubires, R. (2001) *Science* **292**, 2063.

[60] Memmer, R., Kuball, H.-G., and Schonhofer, A. (1993) *Liq. Cryst.* **15**, 345.

[61] Gay, J. G. and Berne, B. J. (1981) *J. Chem. Phys.* **74**, 3316.

[62] Mishra, P., Ram, J., and Singh, Y. (2004) *J. Phys. Condens. Matter* **16**, 1695.

[63] Grason, G. M. and Bruinsma, R. F. (2007) *Phys. Rev. Lett.* **99**, 098101.

[64] Fejer, S. N. and Wales, D. J. (2007) *Phys. Rev. Lett.* **99**, 086106.

[65] Chakrabarti, D. and Wales, D. J. (2008) *Phys. Rev. Lett.* **100**, 127801.

[66] Bates, M. A. and Luckhurst, G. R. (1996) *J. Chem. Phys.* **104**, 6696.

[67] Yan, F., Hixson, C. A., and Earl, D. J. (2009) *Soft Matter* **5**, 4477–4483.

[68] Wales, D. J. and Scheraga, H. A. (1999) *Science* **285**, 1368.

[69] Earl, D. J. and Deem, M. W. (2005) *Phys. Chem. Chem. Phys.* **7**, 3910–3916.

[70] Wilson, M. R. (2007) *Chem. Soc. Rev.* **36**, 1881–1888.

[71] Wilson, M. R. and Allen, M. P. (1991) *Mol. Cryst. Liq. Cryst.* **198**, 465.

[72] Wilson, M. R. and Allen, M. P. (1992) *Liq. Cryst.* **12**, 157.

[73] Cook, M. J. and Wilson, M. R. (2001) *Molec. Cryst. Liq. Cryst.* **363**, 181–193.

[74] Pelaez, J. and R., W. M. (2006) *Phys. Rev. Lett.* **97**, 267801.

[75] Berardi, R., Muccioli, L., and Zannoni, C. (2004) *ChemPhysChem* **5**, 104–111.

[76] Cheung, D. L., Clark, S. J., and Wilson, M. R. (2004) *J. Chem. Phys.* **121**, 9131–9139.

[77] Lansac, Y., Glaser, M. A., Clark, N. A., and Lavrentovich, O. D. (1999) *Nature* **398**, 54–57.

[78] Cacelli, I., Gaetani, L. D., Prampolini, G., and Tani, A. (2007) *J. Phys. Chem. B* **111**, 2130–2137.

[79] Pecheanu, P. and Cann, N. M. (2010) *Phys. Rev. E.* **81**, 041704.

[80] Pizzirusso, A., Savini, M., Muccioli, L., and Zannoni, C. (2011) *J. Mater. Chem.* **21**, 125–133.

[81] Jorgensen, W. L., Maxwell, D. S., and Tirado-Rives, J. (1996) *J. Am. Chem. Soc.* **118**, 11225–11236.

[82] Pelaez, J. and R., W. (2007) *Phys. Chem. Chem. Phys.* **9**, 2968–2975.

[83] Berardi, R., Muccioli, L., Orlandi, S., Ricci, M., and Zannoni, C. (2004) *Chem. Phys. Lett.* **389**, 373–378.

[84] Bizzarri, M., Cacelli, I., Prampolini, G., and Tani, A. (2004) *J. Phys. Chem. A* **108**, 10336–10341.

[85] Amovilli, C., Cacelli, I., Campanile, S., and Prampolini, G. (2002) *J. Chem. Phys.* **117**, 3003–3012.

[86] Sluckin, T. J. (1989) *Liq. Cryst.* **6**, 111.

[87] Frenkel, D. and Smit, B. (2002) Understanding molecular simulation, 2nd ed., Academic Press: San Diego, CA, .

[88] Allen, M. P. and Tildesley, D. J. (1987) Computer Simulation of Liquids, Clarendon Press, Oxford, .

[89] Yan, F. and Earl, D. J. An all atom computer simulation study of the liquid crystalline phase behavior of alkenic fluoroterphenyls, Manuscript in preparation (2011).

[90] Yan, F. and Earl, D. J. Atomistic simulations of liquid crystal mixture of alkoxy substituted phenylpyrimidines 2php and phph14, Manuscript in preparation (2011).

[91] Humphrey, W., Dalke, A., and Schulten, K. (1996) *J. Mol. Graph.* **14**, 33–38.

[92] Moll, A., Hildebrandt, A., Lenhof, H.-P., and Kohlbacher, O. (2006) *Bioinformatics* **22**, 365–366.

[93] Moll, A., Hildebrandt, A., Lenhof, H.-P., and Kohlbacher, O. (2006) *J. Comput.-Aided Mol. Des.* **19**, 791–800.

[94] Pettersen, E. F., Goddard, T. D., Huang, C. C., Couch, G. S., Greenblatt, D. M., Meng, E. C., and Ferrin, T. E. (2004) *J. Comput. Chem.* **25**, 1605–1612.

[95] Sayle, R. A. and Milner-White, E. J. (1995) *J. Trends Biochem. Sci.* **20**, 374.

[96] Andersen, H. C. (1980) *J. Chem. Phys.* **72**, 2384.

[97] Nosé, S. (1984) *J. Chem. Phys.* **81**, 511.

[98] Hoover, W. G. (1985) *Phys. Rev. A* **31**, 1695–1697.

[99] Evans, D. J. (1983) *J. Chem. Phys.* **78**, 3297.

[100] Evans, D. J. (1983) *Physica, A* **118**, 51–68.

[101] Hoover, W. G., Ladd, A. J. C., and Moran, B. (1982) *Phys. Rev. Lett.* **48**, 1818.

[102] Berendsen, H. J. C., Postma, J. P. M., vanGunsteren, W. F., DiNola, A., and Haak, J. R. (1984) *J. Chem. Phys.* **81**, 3684.

[103] Tuckerman, M. E., Berne, B. J., and Martyna, G. J. (1992) *J. Chem. Phys.* **97**, 1990.

[104] Martyna, G. J., Klein, M. L., and Tuckerman, M. E. (1992) *J. Chem. Phys.* **97**, 2635.

[105] Martyna, G. J., Tobias, D. J., and Klein, M. L. (1994) *J. Chem. Phys.* **101**, 4177.

[106] Martyna, G. J., Tuckerman, M. E., Tobias, D. J., and Klein, M. L. (1996) *Mol. Phys.* **87**, 1117.

[107] Tuckerman, M. E., Mundy, C. J., and Klein, M. L. (1997) *Phys. Rev. Lett.* **78**, 2042–2045.

[108] Tuckerman, M. E., Mundy, C. J., and Martyna, G. J. (1999) *Europhys. Lett.* **45**, 149–155.

[109] Tuckerman, M. E. and Martyna, G. J. (2000) *J. Phys. Chem. B* **104**, 159–178.

[110] Tuckermanan, M. E., Liu, Y., Ciccotti, G., and Martyna, G. J. (2001) *J. Chem. Phys.* **115**, 1678.

[111] Miller III, T. F., Eleftheriou, M., Pattnaik, P., Ndirango, A., Newns, D., and Martyna, G. J. (2002) *J. Chem. Phys.* **116**, 8649.

[112] Kamberaj, H., Low, R. J., and Neal, M. P. (2005) *J. Chem. Phys.* **122**, 224114.

[113] Goldstein, H. (1980) Classical Mechanics, Addison-Wesley, Reading, MA, .

[114] McQuarrie, D. A. (2000) Statistical Mechanics, Harper Collins Publisher, NY, .

[115] Trotter, H. F. (1959) *Proc. Am. Math. Soc.* **10**, 545.

[116] Suzuki, M. (1985) *J. Math. Phys.* **26**, 601.

[117] Prigogine, I. (1962) Non-equilibrium Statistical Mechanics, Interscience publishers, NY, .

[118] Verlet, L. (1967) *Phys. Rev.* **159**, 98–103.

[119] Swope, W. C., Andersen, H. C., Berens, P. H., and Wilson, K. R. (1982) *J. Chern. Phys.* **76**, 637–649.

[120] Weiner, S. J., Kollman, P. A., Case, D. A., Singh, U. C., Ghio, C., Alagona, G., Jr, S. P., and Weinerl, P. (1984) *J. Am. Chem. Soc.* **106**, 765–784.

[121] Weiner, S. J., Kollman, P. A., Nguyen, D. T., and Case, D. A. (1986) *J. Comput. Chem.* **7**, 230.

[122] Brooks, B. R., Bruccoleri, R. E., Olafson, B. D., States, D. J., Swaminathan, S., and Karplus, M. (1986) *J. Comput. Chem.* **7**, 230.

[123] Allinger, N. L., Chen, K., and Lii, J.-H. (1996) *J. Comput. Chem.* **17**, 642.

[124] Dubrovin, B. A., Fomenko, A. T., and Novikov, S. P. (1992) Modern Geometry-Methods and Applications: Part I, Springer-Verlag, NY, .

[125] Jeffreys, H. and Jeffreys, B. S. (1988) Methods of Mathematical Physics, 3rd ed., Cambridge University Press, UK, .

[126] Nosé, S. (1984) *J. Chem. Phys.* **81**, 511–519.

[127] Hoover, W. G. (1986) *Phys. Rev. A* **34**, 2499–2500.

[128] Martin, M. G. and Siepmann, J. I. (1998) *J. Phys. Chem. B* **102**, 2569–2577.

[129] Chen, B., Martin, M. G., and Siepmann, J. I. (1998) *J. Phys. Chem. B* **102**, 2578–2586.

[130] Gray, J. J., Moughon, S., Wang, C., Schueler-Furman, O., Kuhlman, B., Rohl, C. A., and Baker, D. (2003) *J. Mol. Biol.* **331**, 281–299.

[131] Schueler-Furman, O., Wang, C., Bradley, P., Misura, K., and Baker, D. (2005) *Science* **310**, 638–642.

[132] Ryckaert, J. P., Ciccotti, G., and Berendsen, H. J. C. (1977) *J. Comput. Phys.* **23**, 327–341.

[133] Andersen, H. C. (1983) *J. Comput. Phys.* **52**, 24–34.

[134] Ciccotti, G., Ferrario, M., and Ryckaert, J.-P. (1982) *Mol. Phys.* **47**, 1253–1264.

[135] Evans, D. J. (1977) *Mol. Phys.* **34**, 327–331.

[136] Kol, A., Laird, B. B., and Leimkuhler, B. J. (1997) *J. Chem. Phys.* **107**, 2580–2588.

[137] Metropolis, N., Rosenbluth, A., Rosenbluth, M., Teller, A., and Teller, E. (1953) *J. Chem. Phys.* **21**, 1087–1092.

[138] Kone, A. and Kofke, D. A. (2005) *J. Chem. Phys.* **122**, 206101.

[139] Wales, D. J. and Doye, J. P. K. (1997) *J. Phys. Chem. A* **101**, 5111–5116.

[140] Carr, J. M. and Wales, D. J. (2005) *J. Chem. Phys.* **123**, 234901.

[141] Verma, A., Schug, A., Lee, K. H., and Wenzel, W. (2006) *J. Chem. Phys.* **124**, 044515.

[142] Bogdan, T. V., Walesa, D. J., and Calvo, F. (2006) *J. Chem. Phys.* **124**, 044102.

[143] Weeks, J. D., Chandler, D., and Andersen, H. C. (1971) *J. Chem. Phys.* **54**, 5237–5247.

[144] Maiti, P. K., Lansac, Y., Glaser, M. A., and Clark, N. A. (2004) *Phys. Rev. Lett.* **92**, 025501.

[145] Press, W. H., Teukolsky, S. A., Vetterling, W. T., and Flannery, B. P. (2007) Numerical Recipes, Cambridge University Press, Cambridge, England, .

[146] Earl, D. J. and Wilson, M. R. (2003) *J. Chem. Phys.* **119**, 10280–10288.

[147] Earl, D. J., Osipov, M. A., Takezoe, H., Takanishi, Y., and Wilson, M. R. (2005) *Phys. Rev. E* **71**, 021706.

[148] Coles, H. J. and Pivnenko, M. N. (2005) *Nature* **436**, 997–1000.

[149] Brizard, A., Oda, R., and Huc, I. (2005) Low molecular mass gelators, design, self-assembly, function In edited by F. Fages, Topics in Current Chemistry Vol. 256 Springer, Berlin.

[150] Earl, D. J., Ilnytskyi, J., and Wilson, M. R. (2001) *Mol. Phys.* **99**, 1719.

[151] Rudnick, J. and Gaspari, G. (1986) *J. Phys. A: Math. Gen.* **19**, L191.

[152] Crooker, P. P. (2001) Chirality in liquid crystals In ed. H.-S. Kitzerow and C. Bahr Springer-Verlag, New York.

[153] deMiguel, E., Rull, L. F., Chalam, M. K., and Gubbins, K. E. (1991) *Mol. Phys.* **74**, 405.

[154] Berardi, R., Emerson, A. P. J., and Zannoni, C. (1993) *J. Chem. Soc., Faraday Trans.* **89**, 4069.

[155] McGrother, S. C., Gil-Villegas, A., and Jackson, G. (1996) *J. Phys.: Condens. Matter* **8**, 9649.

[156] Polson, J. M. and Frenkel, D. (1997) *Phys. Rev. E: Stat., Nonlinear, Soft Matter Phys.* **56**, R6260.

[157] Pfleiderer, P. and Schilling, T. (2007) *Phys. Rev. E: Stat., Nonlinear, Soft Matter Phys.* **75**, 020402.

[158] Dewar, A. and Camp, P. J. (2004) *Phys. Rev. E* **70**, 011704.

[159] Xu, J., Selinger, R. L. B., Selinger, J. V., and Shashidhar, R. (2001) *J. Chem. Phys.* **115**, 4333–4338.

[160] Withers, I. M., Care, C. M., and Cleaver, D. J. (2000) *J. Chem. Phys.* **113**, 5078–5090.

[161] Neal, M. P. and Parker, A. J. (1999) *Mol. Cryst. Liq. Cryst.* **330**, 565.

[162] Nguyen, T. D., Zhang, Z., and Glotzer, S. C. (2008) *J. Chem. Phys.* **129**, 244903.

[163] Hess, B., Kutzner, C., van derSpoel, D., and Lindahl, E. (2008) *J. Chem. Theory Comput.* **4**, 435–447.

[164] van derSpoel, D., Lindahl, E., Hess, B., Groenhof, G., Mark, A. E., and Berendsen, H. J. C. (2005) *J. Chem. Theory Comput.* **26**, 1701–1719.

[165] Lindahl, E., Hess, B., and van derSpoel, D. (2001) *J. Mol. Mod.* **7**, 306–317.

[166] Berendsen, H. J. C., van derSpoel, D., and vanDrunen, R. (1995) *Comp. Phys. Comm.* **91**, 43–56.

[167] Rychaert, J. P. and Bellemans, A. (1975) *Chem. Phys. Lett.* **30**, 123–125.

[168] Hess, B. (2008) *J. Chem. Theory Comput.* **4**, 116–122.

[169] Essman, U., Perela, L., Berkowitz, M. L., Darden, T., Lee, H., and Pedersen, L. G. (1995) *J. Chem. Phys.* **103**, 8577–8592.

[170] Parrinello, M. and Rahman, A. (1981) *J. Appl. Phys.* **52**, 7182–7190.

[171] Fontana, M. P. and Rosi, B. (1986) *Phys. Rev. A* **33**, 4132–4142.

[172] Bondi, A. (1964) *J. Phys. Chem.* **68**, 441–451.

[173] McDonald, A. J. and Hanna, S. (2006) *J. Chem. Phys.* **124**, 164906.

[174] Kuprusevicius, E., Edge, R., Gopee, H., Cammidge, A. N., McInnes, E. J. L., Wilson, M. R., and Oganesyan, V. S. (2010) *Chem. Eur. J.* **16**, 11558–11562.

[175] Zhou, R. (2003) *Proc. Natl. Acad. Sci. USA* **100**, 13280–13285.

[176] Pitera, J. W. and Swope, W. (2003) *Proc. Natl. Acad. Sci. USA* **100**, 7587–7592.

[177] Wang, J. M., Cieplak, P., and Kollman, P. A. (2000) *J. Comput. Chem.* **21**, 1049–1074.

[178] Tsui, V. and Case, D. A. (2000) *Biopolymers* **56**, 275–291.

[179] Dutta, D., Fruitwala, H., Kohli, A., and Weiss, R. A. (1990) *Polym. Eng. Sci.* **30**, 1005–1026.

[180] Lemieux, R. P. (2001) *Acc. Chem. Res.* **34**, 845–853.

[181] Eelkema, R. and Feringa, B. L. (2006) *Org. Biomol. Chem.* **4**, 3729–3745.

[182] Cinacchi, G., Martinez-Raton, Y., Mederos, L., and Velasco, E. (2007) *Mol. Cryst. Liq. Cryst.* **465**, 121–132.

[183] Koda, T. and Kimura, H. (1987) *J. Phys. Soc. Jpn.* **36**, 2929.

[184] Stroobants, A. (1992) *Phys. Rev. Lett.* **69**, 2388.

[185] Cinacchi, G., Mederos, L., and Velasco, E. (2004) *J. Chem. Phys.* **121**, 3854–3863.

[186] Camp, P. J. and Allen, M. P. (1996) *Physica A.* **229**, 410–427.

[187] Galindo, A., Haslam, A. J., Varga, S., Jackson, G., Vanakaras, A. G., Photinos, D. J., and Dunmur, D. A. (2003) *J. Chem. Phys.* **119**, 5216–5225.

[188] Koda, T., Nishioka, A., and Ikeda, S. (2005) *J. Phys.: Condens. Matter* **17**, 2875–2878.

[189] Savenko, S. V. and Dijkstra, M. (2006) *J. Chem. Phys.* **124**, 234902.

[190] Vliegenthart, G. A. and Lekkerkerker, H. N. W. (1999) *J. Chem. Phys.* **111**, 4153–4157.

[191] Dogic, Z., Frenkel, D., and Fraden, S. (2000) *Phys. Rev. E.* **62**, 3925–3933.

[192] Camp, P. J., Allen, M. P., Bolhuis, P. G., and Frenkel, D. (1997) *J. Chem. Phys.* **106**, 9270–9275.

[193] Bemrose, R. A., Care, C. M., Cleaver, D. J., and Neal, M. P. (1997) *Mol. Phys.* **90**, 625.

[194] Bates, M. A. and Luckhurst, G. R. (1993) Computer Simulation of Liquid Crystal Phases Formed by Gay-Berne Mesogens, Springer, New York, .

[195] Wilson, M. R. (1997) *J. Chem. Phys.* **107**, 8654–8663.

[196] Cross, C. W. and Fung, B. M. (1994) *J. Chem. Phys.* **101**, 6839.

[197] Diele, S. (1993) *Ber. Bunsen-Ges. Phys. Chem.* **97**, 1326–1336.

[198] Roberts, J. C., Kapernaum, N., Giesselmann, F., and Lemieux, R. P. (2008) *J. Am. Chem. Soc.* **130**, 13842–13843.

[199] Kapernaum, N., Hartley, C. S., Roberts, J. C., Schoerg, F., Krueerke, D. Lemieux, R. P., and Giesselmann, F. (2010) *Chem. Phys. Chem.* **11**, 2099–2107.

[200] Stimson, L. M. and Wilson, M. R. (2005) *J. Chem. Phys.* **123**, 034908.